

DTIC FILE COPY

4

AD-A219 801

AFGL-TR-88-0300

Radar Sounder

F. E. Nathanson
T. Slocumb
L. Brooks
S. W. McCandless
R. Crane

Technology Service Corporation
962 Wayne Avenue
Suite 600
Silver Spring, MD 20910

September 1988

Final Report
August 1987 - September 1988

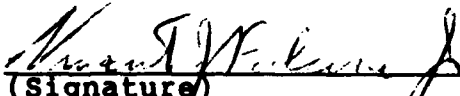
Approved for public release; distribution unlimited.

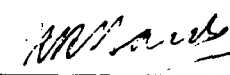
Air Force Geophysics Laboratory
Air Force Systems Command
United States Air Force
Hanscom Air Force Base, Massachusetts 01731-5000

DTIC
S ELECTE D
MAR 28 1990
G B


90 03 26 128

"This technical report has been reviewed and is approved for publication"


(Signature)
Vincent J. Falcone, Jr.
Contract Manager


(Signature)
Dr. Kenneth R. Hardy
Branch Chief

FOR THE COMMANDER


(Signature)
Dr. Robert A. McClatchey
Division Director

This report has been reviewed by the ESD Public Affairs Office (PA) and is releasable to the National Technical Information Service (NTIS).

Qualified requestors may obtain additional copies from the Defense Technical Information Center. All others should apply to the National Technical Information Service.

If your address has changed, or if you wish to be removed from the mailing list, or if the addressee is no longer employed by your organization, please notify AFGL/DAA, Hanscom AFB, MA 01731. This will assist us in maintaining a current mailing list.

Do not return copies of this report unless contractual obligations or notices on a specific document requires that it be returned.

REPORT DOCUMENTATION PAGE

Form Approved
OMB No 0704-0188

Public reporting burden for this collection of information is estimated to average 1 hour per response, including the time for reviewing instructions, searching existing data sources, gathering and maintaining the data needed, and completing and reviewing the collection of information. Send comments regarding this burden estimate or any other aspect of this collection of information, including suggestions for reducing this burden, to Washington Headquarters Services, Directorate for Information Operations and Reports, 1215 Jefferson Davis Highway, Suite 1204, Arlington, VA 22202-4302, and to the Office of Management and Budget, Paperwork Reduction Project (0704-0188), Washington, DC 20503.

1. AGENCY USE ONLY (Leave blank)		2. REPORT DATE 1988 September	3. REPORT TYPE AND DATES COVERED Final Report (August 1987-September 1988)	
4. TITLE AND SUBTITLE Radar Sounder			5. FUNDING NUMBERS PE 61101F PR ILIR TA 7C WU AA Contract F19628-87-C-0231	
6. AUTHOR(S) F.E. Nathanson T. Slocumb L. Brooks			S.W. McCandless R. Crane	
7. PERFORMING ORGANIZATION NAME(S) AND ADDRESS(ES) Technology Service Corporation 962 Wayne Avenue Suite 600 Silver Spring, MD 20910			8. PERFORMING ORGANIZATION REPORT NUMBER	
9. SPONSORING/MONITORING AGENCY NAME(S) AND ADDRESS(ES) Air Force Geophysics Laboratory Hanscom AFB Massachusetts 01731-5000 Contract Manager: Vincent Falcone/LYS			10. SPONSORING/MONITORING AGENCY REPORT NUMBER AFGL-TR-88-0300	
11. SUPPLEMENTARY NOTES				
12a. DISTRIBUTION / AVAILABILITY STATEMENT Approved for public release; distribution unlimited			12b. DISTRIBUTION CODE	
13. ABSTRACT (Maximum 200 words) This report describes a study of a Radar Sounder on an orbiting Satellite as a remote sensing tool with meteorologic and oceanographic applications. The study had as its primary objective the determination of cloud base altitudes for non-precipitating clouds. After selecting 3 potential candidates (a scanning dish, a long array, and a synthetic aperture radar) an exhaustive systems analysis was performed over all radar parameters at four carrier frequencies. The resulting system will meet the goals in the specification with the detectable water content level of stratus clouds dependent on swath size, orbit altitude and resolution. The "baseline" system consists of a relatively simple Ka band radar conically scanning about nadir. The calibration of the radar will take into account the attenuation of the electromagnetic waves by clouds and especially precipitation. It will be accomplished in at least two ways. The first will be by placing supplemental radiometer feeds on the dish. The second is to measure the reflected radar signals from the surface. The proposed system, will also detect sea ice, and will be able to derive approximate surface wind speed and direction over the oceans.				
14. SUBJECT TERMS Satellite Radar Sounder Cloud Heights Rain			15. NUMBER OF PAGES 140	
Satellite Microwave Radiometer Sea Surface Winds			16. PRICE CODE	
17. SECURITY CLASSIFICATION OF REPORT Unclassified	18. SECURITY CLASSIFICATION OF THIS PAGE Unclassified	19. SECURITY CLASSIFICATION OF ABSTRACT Unclassified	20. LIMITATION OF ABSTRACT SAR	

ACKNOWLEDGMENTS

The authors would like to acknowledge the support of numerous individuals who contributed to the study and especially: Dr. Linwood Jones of the Harris Corporation who provided analysis and descriptions of the antenna and helped size the instrument; Dr. Julius Goldhirsh of Applied Physics Laboratory, Johns Hopkins University for guidance on algorithm development; Burt Plitt and Arch Mitchell of The Westinghouse ESG who provided information on transmitter sizing and cooling requirements, and to Walter Gregorowich of Lockheed for information on a possible U-2 experiment.

We also would like to express thanks to Cori Beckmann for typing of this report.



Accession For	
NTIS GRA&I	<input checked="checked" type="checkbox"/>
DTIC TAB	<input type="checkbox"/>
Unannounced	<input type="checkbox"/>
Justification	
By	
Distribution/	
Availability Codes	
Dist	Avail and/or Special
A-1	

TABLE OF CONTENTS

1.0	Introduction and Summary	1
2.0	Meteorological Goals	7
2.1	Objective	7
2.2	Background	7
2.3	Radar Measurement Requirements	8
2.3.1	Spatial Resolution	9
2.3.2	Spatial Sampling	9
2.3.3	Cloud Properties	13
2.3.4	Rain Rate Measurements	15
2.4	Cloud and Precipitation Observing System	15
3.0	Trade-Off Studies of Radar Techniques and Frequency Selection	17
3.1	Boom Antenna (Metrad) Performance Assessment	17
3.1.1	Metrad Design Trade-Off	20
3.1.2	Metrad Summary	21
3.2	Scanning Altimeter Trade-Offs and Frequency Selection	29
3.3	Synthetic Aperture (METSAR) Mode Assessment Summary	44
3.3.1	Synthetic Aperture Radar Principles	44
3.3.2	System Operating Criteria - Strip Mapping Mode	45
3.3.3	SCANSAR Mode	50
3.3.4	Adaptation of the Meteorological Scanning Altimeter for a High Resolution, Limited Swath SAR Ground Mapping Mode	51
3.3.5	METSAR Mode Conclusions	53
3.4	Surface Reflectivity	54
4.0	Baseline System Evolution	55
4.1	Conical Scanning Strategy	55
4.2	Waveform Selection and Number of Samples	58
4.2.1	Detection Considerations	58
4.2.2	Estimation Considerations	67
4.3	Radar Parameter Selection and Detection Capabilities	70
4.4	Algorithms for Spatial Extent, Rain Rate and Liquid Water Content Retrieval and Particle Distribution	74

4.4.1	Spatial Extent	74
4.4.2	Rain Rate and Atmospheric Liquid Water Content (LWC) Retrieval	76
4.4.2.1	Backscatter Method	76
4.4.2.2	Attenuation Coefficient Method	87
4.4.2.3	Recommendations	89
4.5	Supplementary Use of Radiometers and Scatterometers	91
4.6	System Block Diagrams	96
5.0	System Implementation Based on Hardware State of the Art	99
5.1	Transmitter and Power Supply Selection	99
5.2	Thermal Control	104
5.3	Antenna Considerations	105
5.4	Antenna Feed Design	107
5.5	Receiver Noise Temperature	111
5.6	Data Rate Assumptions and Analysis	114
5.7	Baseline Radiometer	116
5.8	Power and Weight Estimates	117
6.0	System Trade-Offs and Plan of Action	118
6.1	Orbit Selection	118
6.2	Long Lead Items	125
7.0	Recommendations	126
8.0	References	130

1.0 INTRODUCTION AND SUMMARY

This report describes a study of a Radar Sounder on an orbiting Satellite as a remote sensing tool with meteorologic and oceanographic applications.

The "Radar Sounder" focused on the design of an active radar on a spacecraft to study atmospheric parameters and especially clouds and precipitation. The study had as its primary objective the determination of cloud base altitudes for non-precipitating clouds. Related objectives included determining cloud top height, horizontal and vertical extent of rain, melting layer altitude, rain intensity, particle size distribution parameters, and cloud phase.

The most difficult objective of the Radar Sounder design was to obtain sufficient backscatter from the bottom of the cloud after the electromagnetic signals have been attenuated by passing through the upper portions of the cloud. In addition, these weak signals must be separated from the much stronger surface echoes. The difficulty is illustrated on Table 1.1 where the cloud parameters (in radar terms) are related to the potential radar carrier frequencies. The goal is to determine cloud bottoms with a stratus cloud model. Note that the reflectivity (η) for Stratus is 38dB lower than for light rain at Ku (13.6 GHz) and 26dB lower at W (94 GHz).

Since earlier studies by TSC and others had light rain as a goal, the radar sounder must be over 3 orders of magnitude more sensitive. To achieve this requires a combination of more transmitted energy, better sensitivity, and larger aperture size.

After selecting 3 potential candidates (a scanning dish, a long array, and a synthetic aperture radar) an exhaustive systems analysis was performed over all radar parameters at the four carrier frequencies indicated. Initial bounds were placed on available transmit power, and receiver sensitivity based on the expected early 1990's state of the art. Antenna diameter was initially limited to 300 wavelengths.

While it will be shown that the differences between the candidate systems was small, the scanning dish or "scanning altimeter" was judged superior and easier to implement. A representative summary of results is shown on Table 1.2 in terms of signal excess or the number of dB above minimum detectable signal. These values are for a selected horizontal resolution. The most interesting result is the clear superiority of Ka band (35.6 GHz) in detecting clouds. The difference is about 6 dB relative to Ku or W band. The somewhat surprising result of the superiority of Ka relative to W results from the higher attenuation and rf losses at W band, the somewhat better available power and receiver sensitivity at Ka band, the larger aperture diameter, and the increased sidelobe clutter problem at W band.

During the study it was realized that larger apertures were possible and that Harris Corp. of Melbourne, FL, was prepared to design and build very lightweight 500-700 wavelength apertures that would lead to better performance.

TABLE 1.1 ATTENUATION AND SCATTERING PROPERTIES

Freq:	13.6 GHz		35 GHz		94 GHz		140 GHz	
	γ^*	η	γ	η	γ	η	γ	η
	(dB/km)	(dBm ⁻¹)	(dB/km)	(dBm ⁻¹)	(dB/km)	(dBm ⁻¹)	(dB/km)	(dBm ⁻¹)
1 mm/h	0.05	-63	0.5	-48	1.9	-43	2.5	-39
Melting	1.8	-47	12.5	-34	22.5	-37	28.5	-39
16 mm/h	1.2	-45	8.7	-32	14.0	-35	17.8	-37
Stratus	0.1	-101	0.9	-85	2.9	-69	4.3	-62
Cirrus	0	-82	0	-65	0	-48	0	-41

* Two way propagation

TABLE 1.2 NOMINAL SIGNAL EXCESS IN dB RELATIVE TO Ka BAND (CALCULATIONS PERTAINING TO RAIN ARE AT 4 km DEPTH AND INCLUDE ATTENUATION)

Frequency (GHz)/Band	13.6/Ku	35.6/Ka	94/W
Heavy Rain (20 mm/hr; 45 dBZ)	46	16	-20
Light Rain (1 mm/hr; 26 dBZ)	31	32	15
Cirrus (- 6 dBZ)	14	21	14
Stratus (0.3 g/m ³ ; -12 dBZ)	-6	0	-6

While earlier studies (Goldhirsh [2], TRMM Studies [11]) indicated that a second system at a different carrier frequency (probably at Ku band) was desired to remove the unknown attenuation and "calibrate" the radar system, its utility in the primary goal of cloud measurement was not evident since its sensitivity at other bands is not adequate. Thus other methods were explored that need only yield data in moderate to heavy rains.

The resulting system proposed in this report will meet the goals in the specification with the detectable water content level of stratus clouds dependant on swath size, orbit altitude and resolution. Horizontal resolution will be 1-2 km, and vertical resolution will be better than 1 km. Accuracy of determining cloud tops and bottoms should be a few hundred meters

The "baseline" system consists of a relatively simple Ka band radar with a 4.1 meter dish, conically scanning about nadir as illustrated on Fig. 1.1. The dish will stow, without folding, in a Shuttle or Titan IV shroud, although both of these launch systems far exceed the weight and volume of the proposed system. The proposed system can be easily launched with lower cost Atlas or Delta Expendable launch vehicles, and the design appears to be well within the state-of-the-art. The orbit altitude will be 300-824 km depending upon the mission.

The calibration of the radar will take into account the attenuation of the electromagnetic waves by clouds and especially precipitation. It will be accomplished in at least two ways: The first will be by placing a supplementary 19 GHz radiometer feed on the dish, and by using the receive system as an additional 37 GHz radiometer. Since the measured brightness temperature over the oceans is dependant on rainfall rate (Wilheit et al., 1977, 1982) the algorithms that estimate this quantity can be easily extended to determine the total attenuation of the radar signals. At Ka band (33-37 GHz) attenuation is independant of drop size distribution for both rain and clouds.

The second technique is to measure the reflected radar signals from the surface (oceans or land) in a "scatterometer" mode, and effectively subtract these values from the predicted echoes to measure attenuation. At the planned Nadir angles, these reflected signals do not vary significantly, and can be deduced from "cloud free" measurements on the same or previous orbits. The Scatterometer is an integral part of the radar.

The proposed system which is currently called ALLRAD will also detect sea ice, and will be able to derive approximate surface wind speed and direction over the oceans.

If desired, a doppler channel can be inserted into the radar to approximately measure wind velocity in the presence of rain or clouds. This is recommended for further study as there is a complicated trade-off between hardware implementation and accuracy.

The proposed sensor system includes the radar and radiometer channels at 19 and 37 GHz. As such, it also performs several of the functions of SSM/I. Table 1.3 shows that it should meet many of the goals of various users with comparable or better performance than other sensors.

TABLE 1.3 RELATIVE PERFORMANCE OF INSTRUMENTS

PRIORITIZED USER REQUIREMENTS	ALLRAD	SSM/I	SCATTER-OMETER	OTHERS
1. Clouds └───Tops, Bottoms Cover	Best	-	-	-
2. Vertical Temperature Profile	V. Good	Good+	-	OLS
3. Absolute Humidity (Moisture Profile)	-	-	-	SSM/T1
└───In Rain, Clouds	-	-	-	SSM/T2
4. Wind └─── Surface	Best Potential	-	-	-
5. Electron Density Profile	Good	Good+	Good	ALT
	-	-	-	SEM
6. Precipitation	Best	Good	-	-
7. Sea Ice	V. Good	Good	?	-
8. Sea Surface Temperature	- *	-	-	OLS
9. Visibility (Aerosol Concentration & Size)	-	-	-	OLS
10. Soil Moisture	Good	Good	TBD**	-
11. Pressure Profile	-	-	-	
12. Neutral Density	-	-	-	
13. Liquid/Solid Water Content & Cloud Droplet Size	Best	Fair- Good+	-	
14. Snow Cover	Good	Fair	-	
15. Land Locked Ice Cover	V. Good	Fair	-	
16. Solar Spectral Imagery/Flux	-	-	-	
17. Land Surface Temperature	?	?	-	
18. Auroral Emissions and Air Glow	-	-	-	
19. Solar Wind	-	-	-	
20. Geo-Magnetic Field	-	-	-	ALT
21. Sea Surface Topography	-	-	-	SAR, ALT
22. Ocean Waves (sea, swell, surf)	V. Good	Some	V. Good	SAR, ALT

- * with additional lower freq. radiometer (4-6 GHz?)
- ** good at low microwave frequencies
- + over the oceans

OLS - Operational Line-scan System
ALT - Altimeter
SAR - Synthetic Aperture
Radar

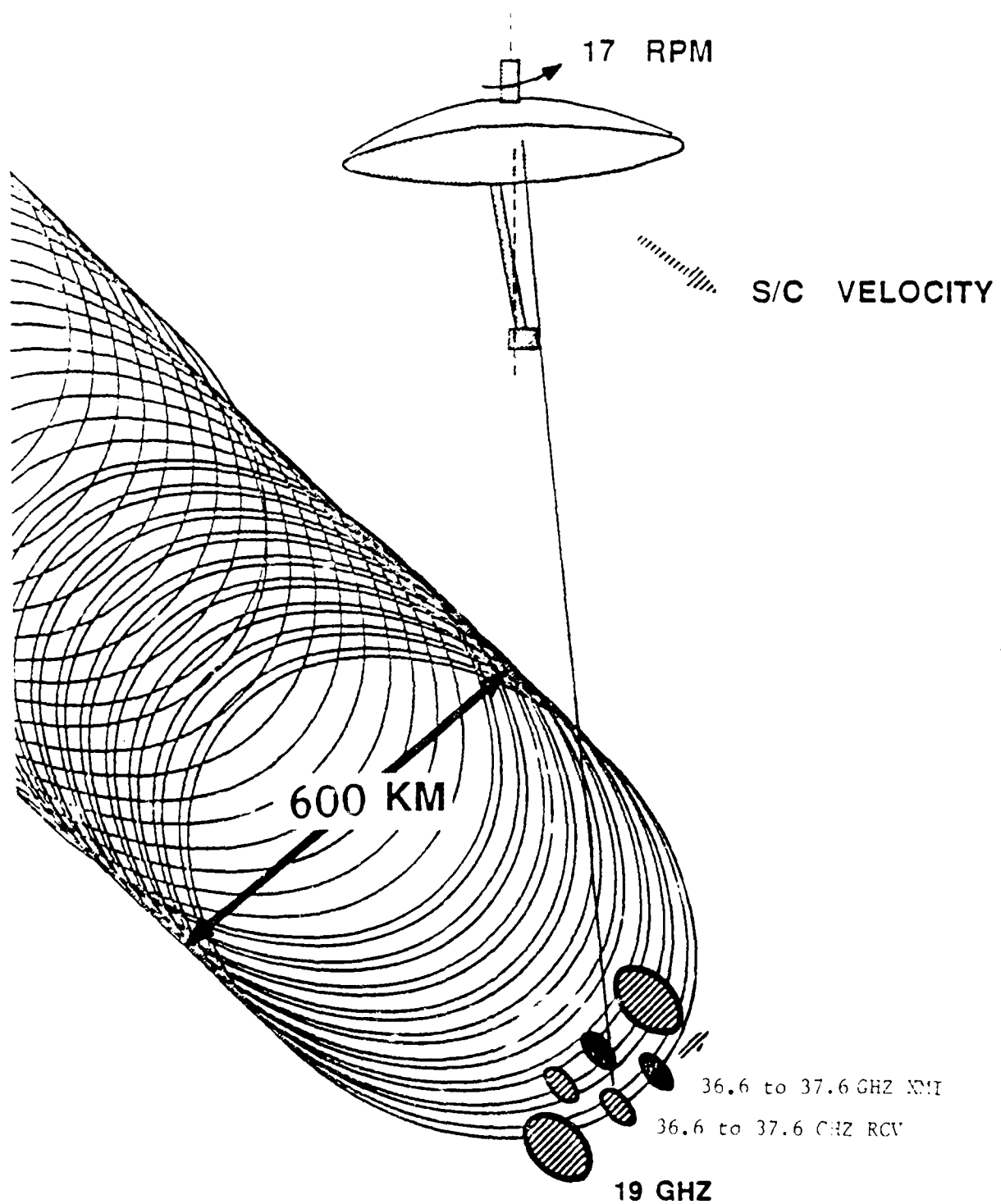


Figure 1.1 ALLRAD Instrument Scenario

The remainder of this report is divided into several sections. Section 2 relates meteorological goals to radar requirements. Section 3 summarizes the approaches studied. A baseline system is described in the following section. Section 5 shows that the hardware is within the state-of-the-art and provides an initial weight estimate. Section 6 illustrates system trade-offs for particular missions or scientific goals. The final section gives a plan for some additional analysis and for developing the instrument starting with a scaled down version on a high altitude aircraft or mountaintop.

The size and weight of the proposed system is comparable to similar scientific satellites. Prime power required for retaining sensitivity for high altitude orbits is moderate and less than several remote sensing satellites.

2.0 Meteorological Goals

2.1 Objective

The primary objective of this study is the design of a radar system for a satellite that is capable of detecting layer clouds and determining cloud base and top heights for clouds higher than 1 km above mean ground level (AGL) with a 300 m accuracy. Additional goals include the measurement of cloud liquid water content; estimation of cloud crystal habit (liquid water droplets, snow, columnar ice, plates, etc.); estimation of rain rate and the observation of the horizontal and vertical structure of rain.

The data from the radar sounder will be useful for providing quantitative moisture analyses for use in the initialization and update of numerical weather prediction models and regional cloud and precipitation forecast models; for providing information on the vertical distribution of latent heat release for use in numerical modeling; and for the verification of numerical model predictions. The instrument will become a primary source of quantitative data for the U.S. Air Force cloud analysis program (RTNEPH).

2.2 Background

Clouds are routinely observed by infrared and visible (visual) wavelength radiometers on geostationary satellites and on polar orbiters such as the Defense Meteorological Satellite Program (DMSP) satellites. The infrared observations provide information on cloud top heights if the clouds are thick enough and completely fill the field of view (FOV) of the sensor. The visible wavelength observations provide higher spatial resolution data on the locations of the clouds during times with sunlight. Neither type of observation can provide direct measurements of the thickness of a cloud layer or the number of cloud layers or the microphysical properties of the clouds such as equivalent liquid water content or crystal habit. The microphysical properties and vertical structure of the clouds are needed for applications of interest to the Air Force such as estimating visibility or the propagation conditions for laser transmission.

At the present time the cloud data used by the Air Force is acquired from a number of different sources. In addition to the infrared and visual observations from satellites, the Air Force Global Weather Center (AFGWC) obtains data from surface observers and from pilots (PIREPS) and employs conventional analyses of radiosonde soundings to predict cloudiness in the absence of direct observations and to convert the infrared radiance values to cloud top height estimates. AFGWC combines these data using their cloud analysis model (Real Time NEPHanalysis model - RTNEPH [Bunting et al., 1983]) to provide their user community with estimates (predictions) of current cloud conditions and to provide input data for the AFGWC cloud forecast models and precipitation analysis models.

A problem with the current cloud analysis system is that the measurements do not provide all the desired information. Cloud tops are estimated from the infrared data and atmospheric temperature soundings. The equivalent cloud liquid water or crystal habit cannot be measured. Statistical models can be incorporated to provide estimates of the

parameters that are not directly measured but different measurements are needed to determine unambiguously the parameter values. Some parameters cannot be measured at all. Cloud layering can often be inferred from cloud top measurements in the pixels within a 25 nm x 25 nm grid element (eighth mesh) of RTNEPH when the lower layers are visible through breaks in the upper layers. When widespread cirrus completely blankets a region, the layering information is not available.

The observing systems can also be confused. Snow or ice on the surface produce the same infrared signature as clouds at mid levels. Thin upper level clouds can be interpreted as low clouds if radiation from the warmer earth is not strongly attenuated by the thin cloud. In the future, microwave radiometer data from the Special Sensor Microwave Imager (SSM/I) on new DMSP satellites will be combined with the infrared and visual data to provide information on snow and ice covered areas to identify regions where the infrared data should not be used in estimating cloud tops.

The SSM/I will also provide information on precipitation that can now only be inferred indirectly from the infrared measurements. The SSM/I measurements are not uniquely related to precipitation intensity but depend on the thickness of the region with precipitation in liquid form, rain, and liquid water clouds; the structure of the melting layer overlying widespread rain or the regions of melting snow and graupel in convective rain; the spatial variation of precipitation within the FOV of the microwave sensors; and the scattering by snow and ice in the upper levels of the storm. The data may be interpreted statistically but additional measurements are needed to determine unambiguously the rain rate or equivalent liquid water content of precipitation.

2.3 Radar Measurement Requirements

Additional information is needed about the vertical extent of regions with rain or clouds and the spatial variations or precipitation and clouds within a layer or layers. Radar provides the tool needed to make the measurements. It must provide profiles of the vertical variations of the backscatter cross section per unit volume (reflectivity) of the clouds, rain, snow, melting snow, etc. at a number of sample points within a grid element of RTNEPH (and on smaller scales for improved editions of RTNEPH). It must sample the variations in reflectivity within the FOVs of the other sensors to be used by RTNEPH. As with the other sensors, the radar reflectivity values are not uniquely related to the parameters to be estimated but the data, when combined with the other inputs to RTNEPH, provide sufficient information to reduce significantly the errors in estimating the desired cloud (and precipitation) parameters.

Cloud layering information will be provided directly by a radar without a requirement for additional measurements provided the radar has sufficient sensitivity to detect the clouds. A radar can determine cloud tops and bases. It is the interpretation of the reflectivity data in terms of liquid water content or rain rate that requires additional information, information already input to RTNEPH.

For use with RTNEPH, a radar could be installed on the DMSP satellites or on special radar satellites. The cloud analysis routines

provide for the combination of data from different sensors on different platforms obtained at different times. If the data are to be used in conjunction with microwave radiometer observations, the sensors should be on the same platform and view the same regions on the surface of the earth.

2.3.1 Spatial Resolution

The radar should have sufficient spatial resolution to observe the significant horizontal variations in precipitation and cloud intensity. Because radar reflectivity is not linearly related to rain rate or liquid water content, significant variations in reflectivity within the FOV and range resolution element of the radar will compromise the measurement capability of the device. Rain occurs within small cells imbedded in regions of less intense precipitation that also contain small cells. For parameter estimation, a variation in reflectivity by a factor of two is considered significant. The cells enclosed by a contour a factor of two below the peak reflectivity value are small and numerous [Crane, [39] 1979]. Typically, about 20 such cells will occur within a RTNEPH grid square. Cell diameters for cells larger than 1 km are exponentially distributed with an average diameter less than two km. Cell lifetimes are exponentially distributed for cells that last longer than 5 minutes. Their average lifetime is less than 20 minutes. These cells produce the rapid variations within the FOV of microwave radiometer systems such as the SSM/I. To map such cells, a radar must have a field of view with a maximum horizontal dimension of less than 0.2 km. To observe the precipitation and to provide data for the correction of the SSM/I observations, a maximum dimension of 2 km is adequate.

Both clouds and rain exhibit spatial variations on a wide range of horizontal and vertical scales. A small fair weather cumulus cloud will have a horizontal dimension approximately the same size as its vertical dimension. Such clouds can be as small as 300 m to as large as several kilometers. Larger cumulus clouds exist but are not identified as fair weather cumulus. The liquid water content of a fair weather cumulus can vary significantly depending on cloud size and cloud base height (temperature). Clouds with a horizontal scale the order of 2 km and a base temperature of the order of 10°C have liquid water contents of 0.5 g/m³ or more and produce reflectivity factors in excess of -10 dBZ.

Stratus clouds also show significant spatial variations. They occur in layers that can be as thin as a few hundred meters to as thick as several km and have liquid water contents ranging from tenths of a g/m³ to several g/m³. To resolve the more important cloud layers, the radar should have a vertical resolution of a kilometer. Cloud base temperature is an important indicator of the microphysical properties of a cloud. Temperature estimates should be within 2°C, requiring that the radar should be able to estimate layer tops and base heights with an accuracy of 300 m.

2.3.2 Spatial Sampling

RTNEPH currently employs an eighth mesh (46 km x 46 km) grid square as its basic analysis element and may, in the future, reduce the

element size by a factor of 2 (4 in area). Significant horizontal variations in precipitation and cloud intensity occur on a wide range of scales, scales both larger and smaller than the dimension of a grid element. Figures 2.1 and 2.2 display the spatial power spectral density for rain rate variations within a 256 km x 256 km area (~30 grid elements) observed in the tropics. Figure 2.1 is a two-dimensional spectrum while Figure 2.2 presents the azimuthal average (one dimensional spectrum) of the two-dimensional spectrum as well as the one-dimensional east-west and north-south spectra. The spectra are plotted vs wavenumber expressed in inverse km ($1/\text{distance}$ not $2\pi/\text{distance}$). The two-dimensional spectrum displays a north-south wave with a 35 km wavelength while the one dimensional spectra reveal the shapes characteristic of two-dimensional turbulence.

Weather radar data analyses reported by Crane [49] show that during steady state conditions, the spatial spectra are similar to those presented in Figures 2.1 and 2.2. The rain rate fields producing these spectra can be interpreted as tracing realizations of the distribution of a passive additive in a two-dimensional turbulent flow field. The outer scale where the spectrum rolls off and flattens at low wavenumbers is not evident in Figure 2.2. The domain of interest for widespread rain or extended regions with strong convection therefore is greater than 250 km and not observable by a single surface based radar. The azimuthally averaged spatial spectrum of rain rate variations has the shape expected for two-dimensional turbulence with the characteristic energy input and rain production scales (marked by vertical arrows in Figure 2.2 where the spectra depart from a k^{-3} power law curve) for the turbulent process varying little with location or climate or the intensity of the precipitation.

The energy input scale for the two-dimensional turbulent flow producing the rain rate variations analyzed for Figure 2.2 is approximately 13 km, a scale nearly identical to the average nearest neighbor distances found by Crane and Hardy [40] [1981] to characterize the organization of the convective clusters of small cells in Kansas storms. The rain input scale is the order of 4 km, a scale nearly identical to the average nearest neighbor distance between the little cells reported by Crane and Hardy.

Recent studies indicate that the energy input scale is important in the organization of light, widespread, winter coastal storms in New England and in summertime convection in Colorado, Tennessee and Massachusetts. A universal spatial spectrum for rain and, by implication, overcast stratus conditions as a precursor of rain provides a model for selecting an optimum sampling strategy for the determination of the statistics of cloud layer and rain within a RTNeph grid square. The power spectral density monotonically decreases with increasing wavenumber (decreasing scale size) for scales smaller than the outer scale (all scales shown in Figure 2.2). It has a segmented power law structure with almost two orders of magnitude reduction in the variance of the precipitation fields between the energy input and rain production scales.

A preliminary analysis of time series of vertically integrated cloud liquid water estimates obtained from vertical pointing multi-frequency microwave radiometer data provided by the NOAA Wave Propagation Laboratory (WPL) [Westwater, 1987] show that the cloud liquid water variation spectra

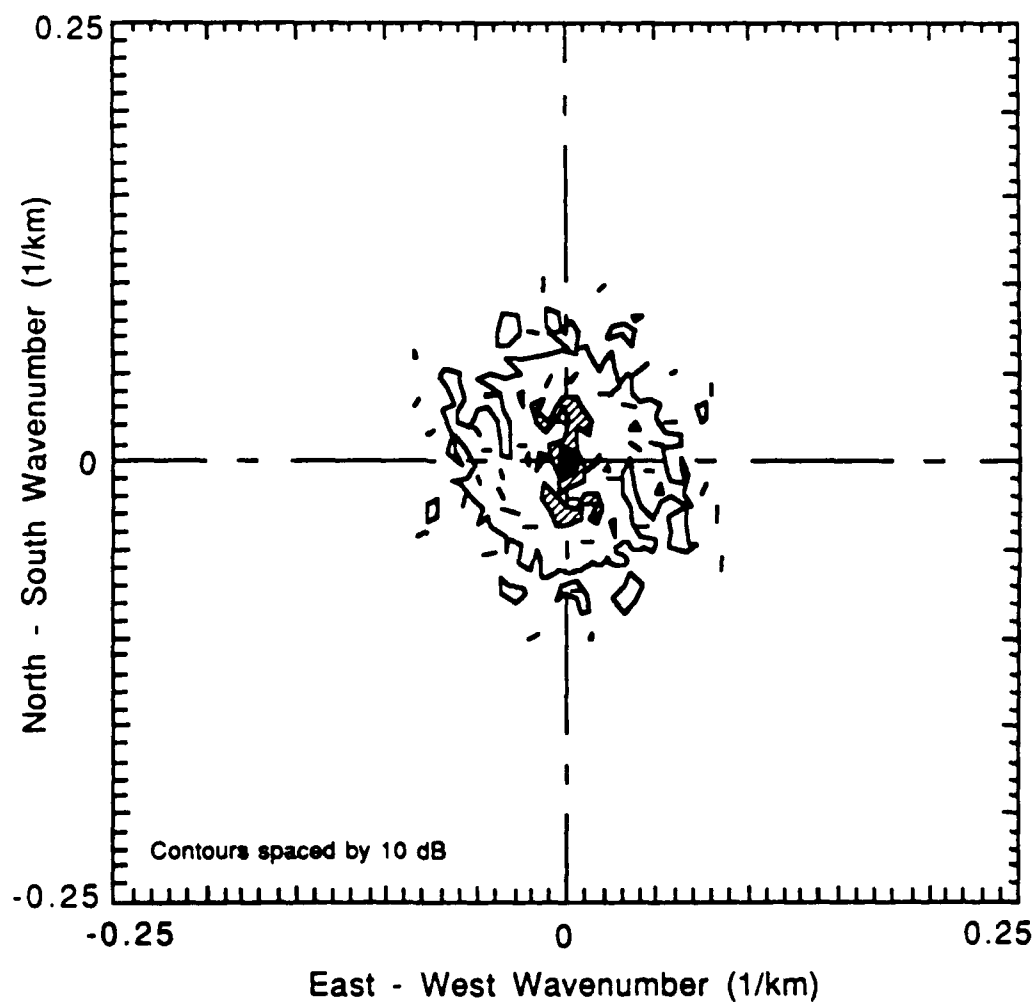


Figure 2.1 Two-dimensional spatial spectrum for MONEX observations, Bintulu, Malaysia, December 1978

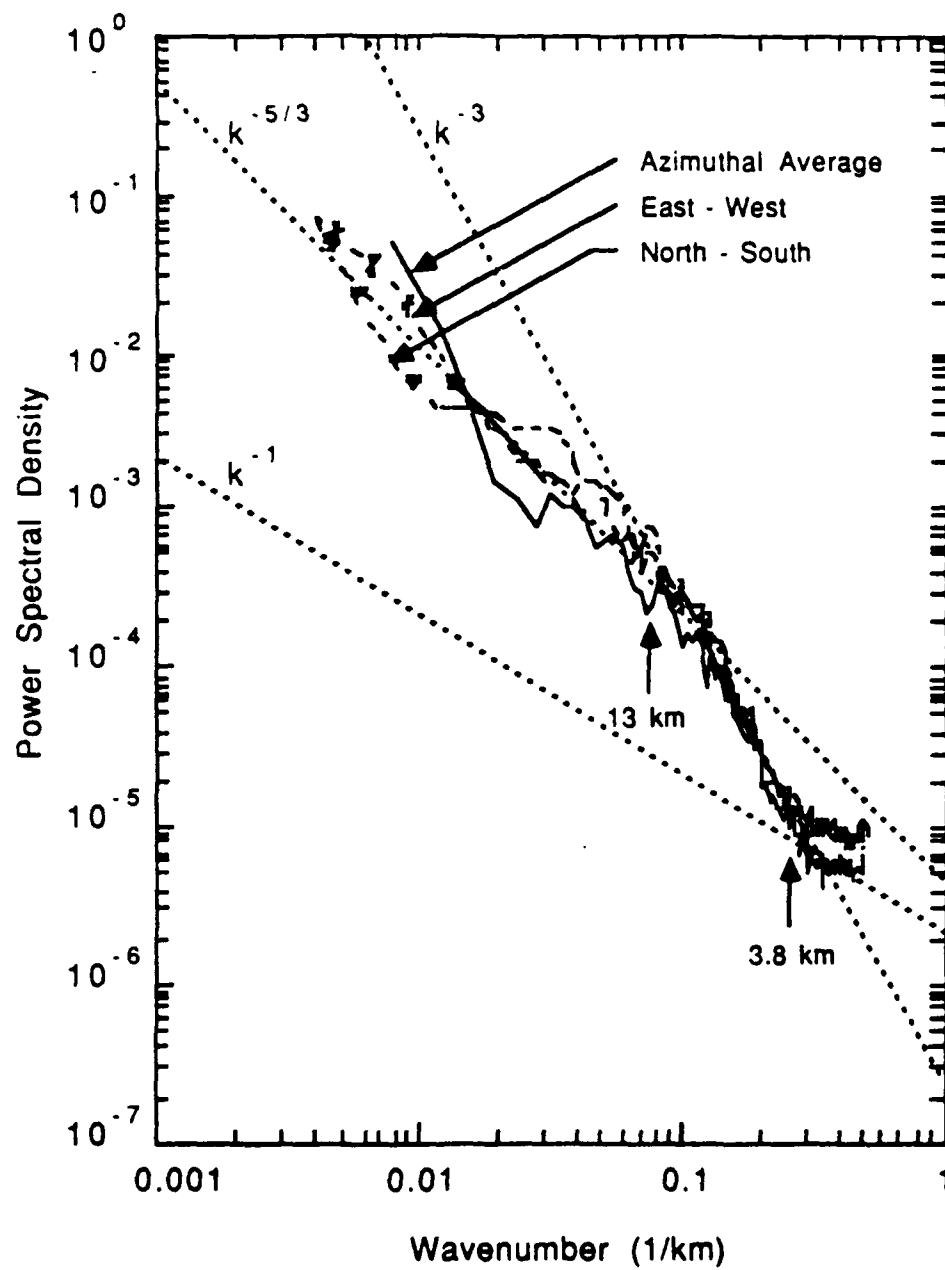


Figure 2.2 One-dimensional spatial spectra for MONEX data in Figure 2.1.

have the same shape as the one-dimensional spectra in Figure 2.2. Crane [49] reported similar results for simultaneous time series and space series from a line of rain gauges. The data show that a single translation velocity connects the spatial and temporal spectra (Taylor's Hypothesis). The WPL cloud observations show that the spatial spectra observed for rain also applies to clouds.

Due to the natural low pass spatial filtering of the precipitation and cloud generation processes, high resolution observations taken at sampling points separated by 6 km contain all the information needed to characterize the rain or cloud fields. Closer spacings between samples will not provide more meteorological information but will improve measurement accuracy increasing the number of radar observations used to prepare a reflectivity estimate.

2.3.3 Cloud Properties

A number of authors have described the microphysical parameters of "typical" clouds for use in estimating atmospheric attenuation and scattering at millimeter wavelengths [Carrier et al., 1967; Sherr et al., 1968; Greaves, 1973; Falcone and Abreu, 1979; Slobin, 1982]. In some instances a probability of occurrence was associated with the selected cloud parameters; in others only a cloud type is associated with the cloud description. For the purpose of estimating the comparative performance of different radar designs, another set of cloud and rain models is proposed. This set is not dependent on occurrence probabilities in any climate region but describes the relative properties of clouds and rain under conditions where questions of visibility near the surface may be important.

The cloud and rain models are to be used to consider cloud type detectability. The cirrus cloud can be used by itself or to represent an overlaying cloud field that would deny infrared or visible wavelength sensors a view of lower level clouds. The stratus cloud can be used by itself. Although low level growth of rain drops is possible in stratus clouds beneath a melting layer, the combination of attenuation by the melting layer and scattering by rain falling through the cloud should mask the signature of the cloud. The light rain, 1 mm/h, model should be used with an overlaying melting layer. Heavy rain, 16 mm/h, should be used by itself for modeling. The thicknesses for rain are heights above mean sea level. Clouds are positioned so the stratus clouds lie below the -10°C (approx. 6.5 km mean sea level, summer at 30°N Lat.) isotherm and cirrus clouds lie above the -20°C (approx. 8 km mean sea level, summer at 30°N Lat.) isotherm.

The melting layer introduces a total, two way attenuation of 0.5 dB at 13.6 GHz, 3.8 dB at 35 GHz, 6.8 dB at 94 GHz and 8.6 dB at 140 GHz. The melting layer calculations were based on the vertical propagation measurements at 35 GHz made by Joss et al. [1974]. It is noted that the model suggests a lack of discrimination between the melting layer and light rain below at 140 GHz. The properties of snow could also be modeled but their effect is to produce a scattered signal but little attenuation. As a rule of thumb, the scattering in the snow just above the melting layer is comparable in cross section to the rain just below the melting layer. Because it is the combination of attenuation and weak scattering from

TABLE 2.1 RAIN AND CLOUD MODELS

Type	Liquid Water Content (g/m ³)	Mean Diameter (μ m)	Reflectivity (dBZ)	Thickness (km)	Doppler Spread (m/s)
Rain 1 mm/h	0.06	310	26	4.0	1.0
Melting Layer (Use with 1 mm/h)	0.3	570	41	0.3	1.0
Rain 16 mm/h	0.7	500	43	4.0	2.0
Stratus	0.3	9.7	-12	1.0	0.2
Cirrus	0.17	170	14	1.0	0.2

regions below attenuating layers that sets the most stringent design constraints, a consideration of snow effects will not change the conclusions about radar system design.

2.3.4 Rain Rate Measurements

Radar sounders capable of observing clouds with reflectivities 40 dB below those of light rain suffer from severe attenuation in the rain as indicated in Table 1.1. Accurate measurements of rain rate at the surface are difficult to impossible when significant attenuation occurs along the path between the radar and the observing volume. Additional information are needed, either from other sensors or from the underlying statistics of the rain process. Radiometer observations provide constraints on the possible variations of rain rate along the path. The apparent statistical regularity of the rain process provides additional constraint.

For regions with rain larger than several hundred kilometers on a side, the observed cumulative distributions of rain rate closely approximate a log-normal distribution (for averages over a 1 km x 2 km x 2 km resolution cell). Figure 2.3 depicts a sample distribution for one volume scan of a weather radar (the same data used for the preparation of Figures 2.1 and 2.2). The observations have a log-normal distribution as indicated by the straight line on the figure. The tail of the distribution will provide a better estimate of the occurrences of the rain rate extremes in a large observation area, say the size of a RTNEPH grid square, than any of the multi-sensor inversion algorithms for the estimation of rain rate.

2.4 Cloud and Precipitation Observing System

A radar by itself cannot provide the data needed by the Air Force to generate the cloud and precipitation fields (analysis) needed to initialize cloud forecast models and, eventually, provide the moisture fields to update numerical weather prediction models. Used in conjunction with other observations the radar will provide information not currently available to the Air Force and will provide the data needed to correct and interpret measurements by other sensors already in use by the Air Force. RTNEPH or a similar analysis program will be required to combine the data from the radar and other sensors.

A complete system should use the multi-sensor analysis program output for input to cloud and precipitation forecast programs and the global numerical weather prediction program. The forecasts should then be input to the analysis program to provide refined estimates of the cloud microphysical parameters which in turn will provide latent heat release input data to the numerical weather prediction programs. The entire process should be viewed as a large feedback system with the input the current data on the states of the atmosphere: clouds, precipitation, winds, atmospheric temperature profiles, temperature and moisture soundings from satellites, etc. and the output the current and forecast states of the atmosphere.

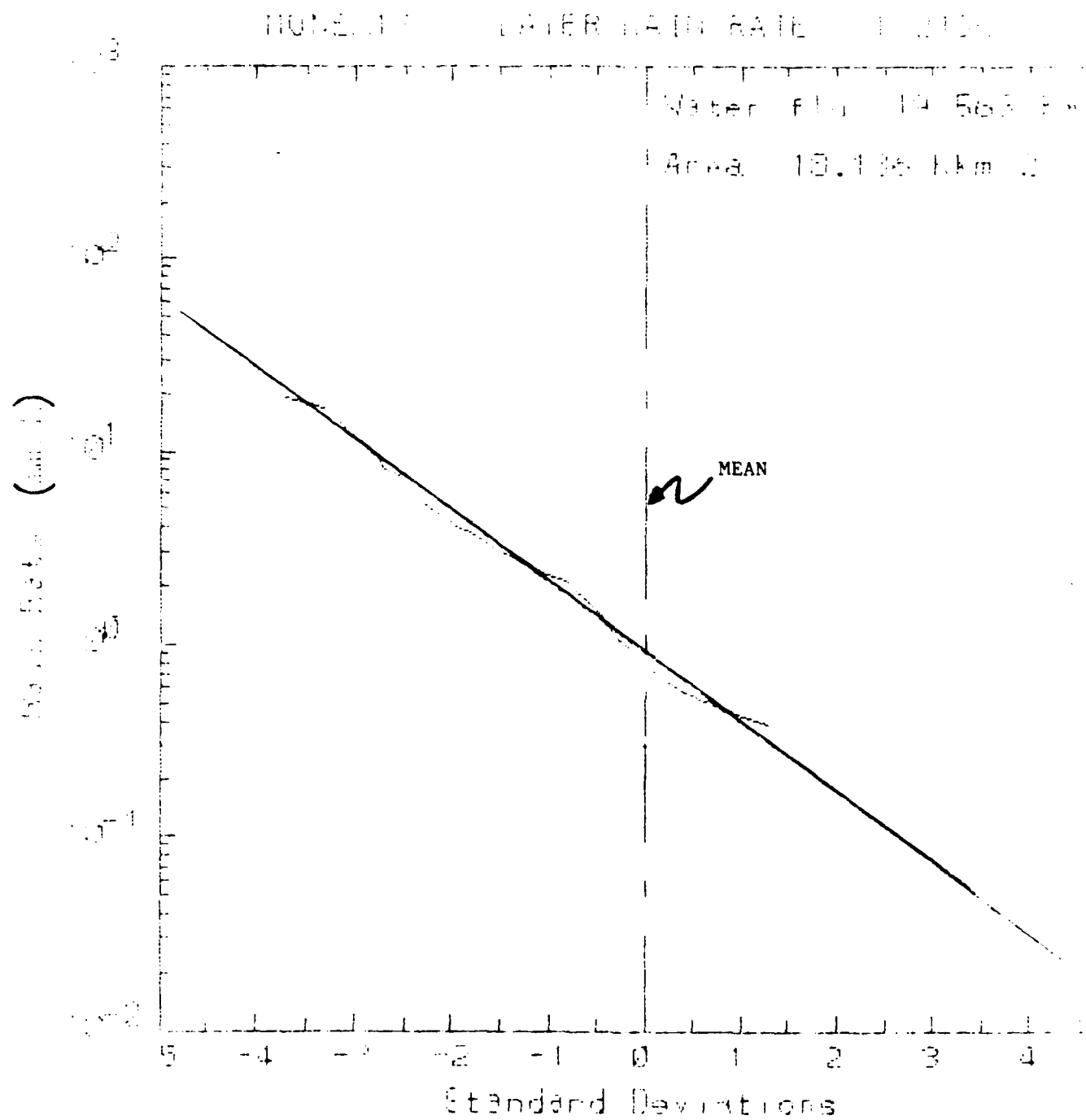


FIGURE 2.3 SAMPLE DISTRIBUTION FOR LARGER RAIN

3.0 TRADE-OFF STUDIES OF RADAR TECHNIQUES AND FREQUENCY SELECTION

This section reviews the trade-offs between various radar implementations and parameter trade-offs including the selection of radar carrier frequency. With the three configurations studied, the carrier frequency selection was basically the same (Ka band).

The first technique is a relook at an approach evaluated for a shuttle application in 1975. The goal at that time was to detect light rain with a high data rate. It achieved that with a long, (700-1000) wavelength but narrow linear array that was believed to be feasible in the early 1980's.

The second approach utilizes a relatively large scanning dish which it will be shown to have the desired swath and sensitivity with the simplest implementation. It was not believed to be practical in 1975.

The final trade-off considers synthetic aperture techniques. It is shown that high spatial resolution can be achieved, but only over a narrow swath. It may be a good mode for small scale observations, but not applicable to broad coverage.

3.1 BOOM ANTENNA (METRAD) PERFORMANCE ASSESSMENT

One technical approach evaluated for the Sounder study is based on the Metrad boom system which was investigated at TSC for NASA for possible shuttle applications. The Metrad boom system is a "pushbroom" type of sensor with multiple receive azimuth beams and corresponding receiver channels. A boom type of antenna is used to transmit a beam which is wide in the azimuth plane (30-70 degrees) and only a few milli-radians in the elevation plane. Figure 3.1.1 illustrates the Metrad atmospheric coverage. The proposed receive antenna is an array of strip-line which forms multiple azimuth beams and one elevation beam which is the same width as the transmit elevation beam. Doppler beam sharpening is used to enhance azimuth resolution and minimize the number of receive beams/channels necessary to achieve the desired swath. Figure 3.1.2 gives a block diagram of the Metrad receiver configuration.

Referring to Figure 3.1.1, the Metrad swathwidth is determined by the width of the transmit azimuth beam, the angle that the beam center subtends to the satellite velocity vector, and the nadir angle. Metrad resolution is a function of elevation beamwidth (θ_{bw}), azimuth synthetic (doppler) beam width (ϕ), pulsewidth (τ), slant range (R), and grazing angle (ψ). The following equations give the vertical (nadir pointing) and horizontal resolution of Metrad,

$$VRES = R \cdot \theta_{bw} \cdot \sin(\psi) + (c\tau/2) \cdot \cos(\psi)$$

$$HRES1 = R \cdot \theta_{bw} \cdot \cos(\psi) + (c\tau/2) \cdot \sin(\psi)$$

$$HRES2 = R \cdot \phi$$

The length of the vertical boom is related to the radar resolution via the elevation beamwidth. Vertical boom length is determined by the radar

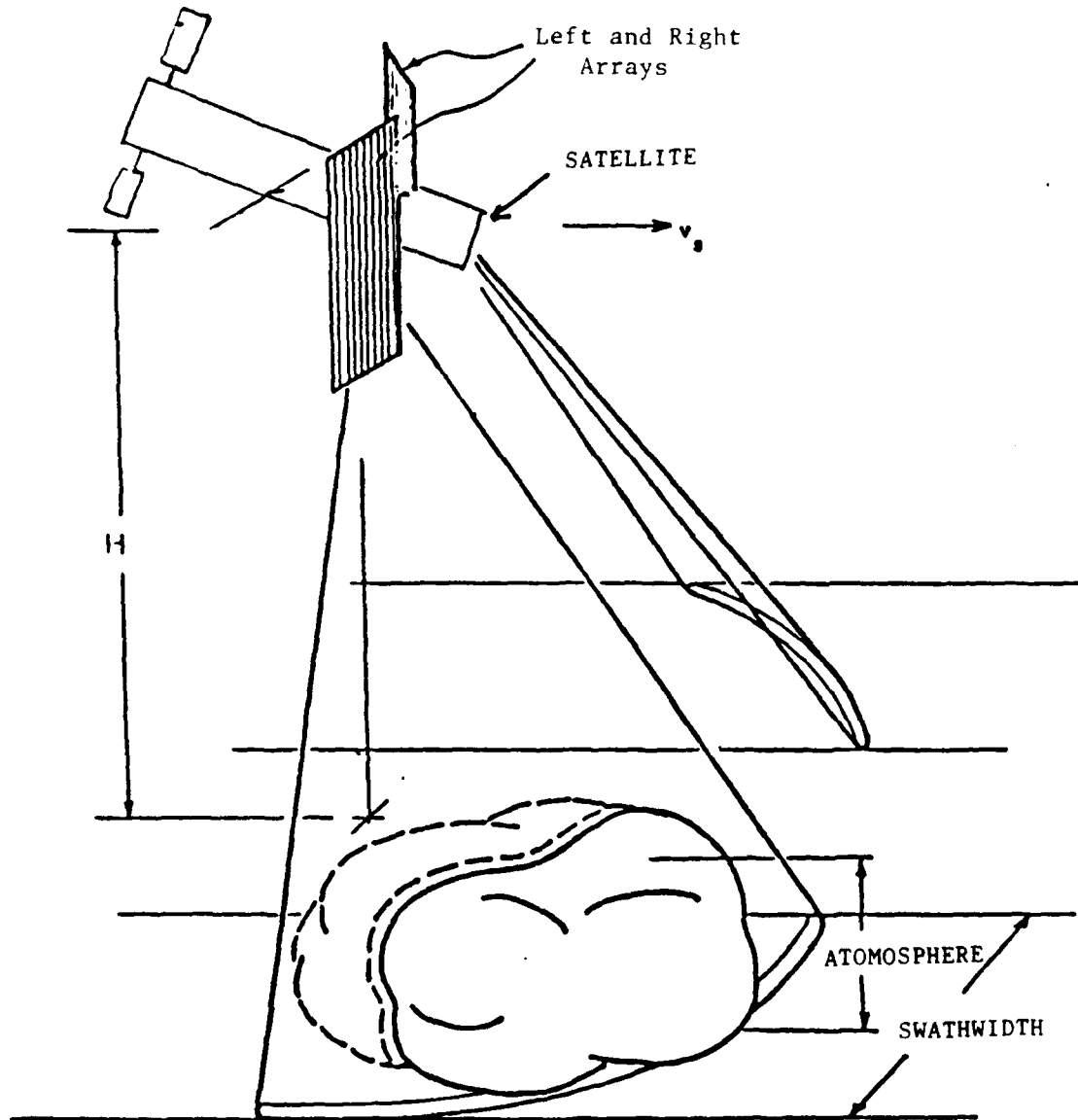


Figure 3.1.1 Metrad Coverage

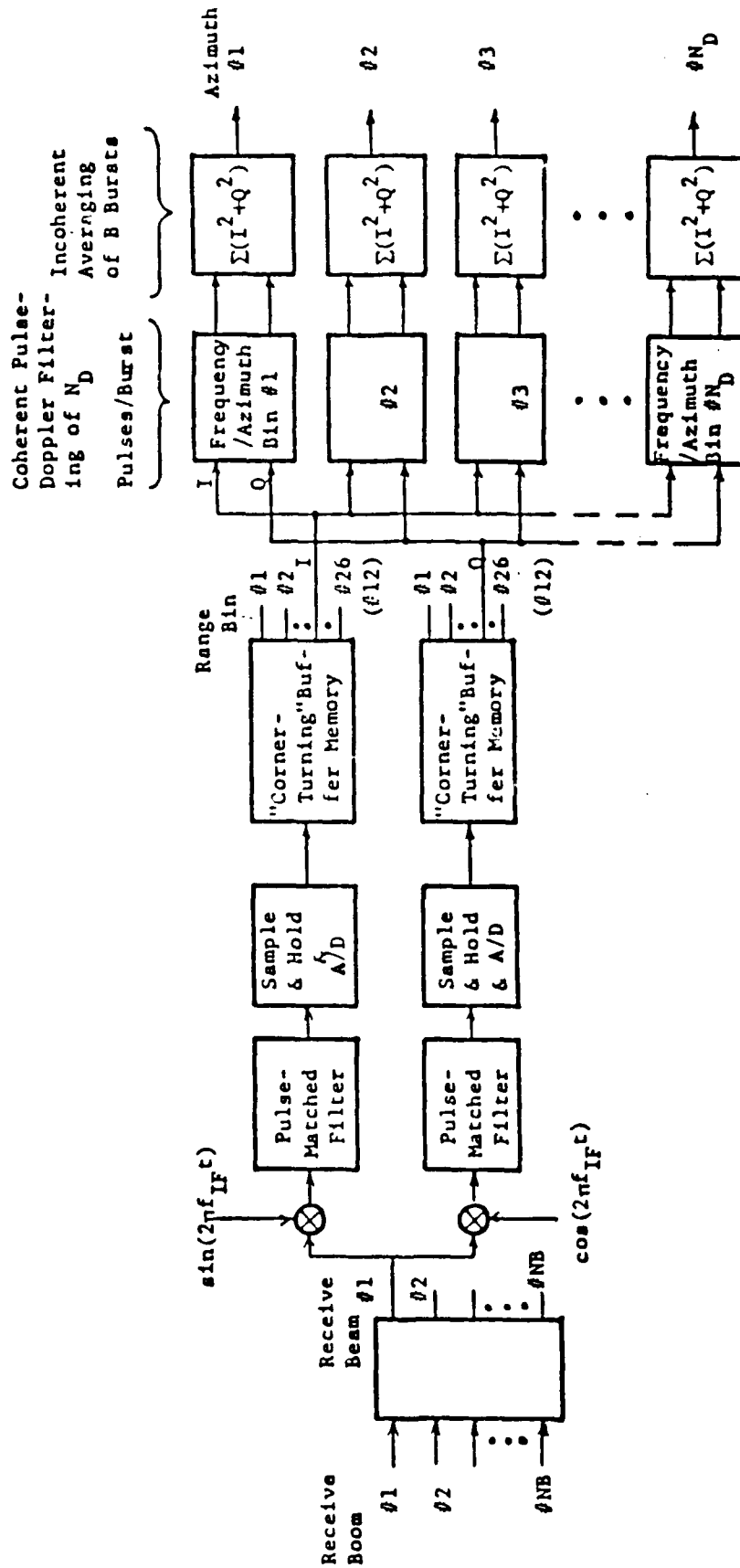


Figure 3.1.2 Metrad Receiver Block Diagram

wavelength (λ), the elevation beamwidth, (θ_{bw}), and the nadir angle (α) in the following equation,

$$VBL = \lambda \cdot 1.4 / (\theta_{bw} \cdot \sin(\alpha) \cdot \sqrt{2})$$

One Metrad system parameter which has significant impact on system complexity is the number of real receive beams. There are several receive beams which span the transmit azimuth beam. The number of receive beams necessary to span the transmit beam depends on the maximum allowable receive beamwidth which is not constrained by horizontal resolution requirements because doppler beam sharpening is being used. However, the maximum time-bandwidth product across any receive beam must be less than unity to give unambiguous doppler filters across the entire receive beam. The result is that the bandwidth across the receive beam must be less than the radar pulse repetition frequency. The PRF is constrained by the necessity to be range unambiguous in the atmosphere. The atmospheric thickness is assumed to be 18 km. The highest bandwidth receive beam is that which is pointed closest to the satellite direction of motion. If the PRF is constrained to 7 kHz, then the width of the highest bandwidth receive beam is computed such that the bandwidth is less than 7 kHz. The width of the highest bandwidth receive beam is used to compute the width of the receive strip line. The number of real receive beams necessary to span the transmit beam can be computed using the width of the receive stripline. It will be shown that for a 200 km swath and a PRF constrained by the atmospheric range ambiguity, a large number of receive beams/channels is necessary for 300 to 800 km orbits.

The original Metrad waveform was a burst waveform which did not allow transmission during the receive period. A group of pulses (the number necessary for the desired doppler resolution) was transmitted at a constant PRF, and transmission was suspended until atmospheric return from the last pulse was gated. The concern was transmitter-receiver interference. During the current study it was decided that a continuous mode is possible. Therefore, the constant PRF, continuous mode waveform was used for this study.

3.1.1 Metrad Design Tradeoff

Using a precedence matrix approach, the Metrad design equations were prioritized and 17 inputs were identified. Using these inputs, the basic Metrad design can be computed. Six of the 17 inputs were chosen to perform a design tradeoff. The 17 inputs are listed in Table 3.1.1 as either fixed or variable inputs. The design tradeoff was performed at Ku-band (13.5 GHz) and Ka-band (35 GHz). Design experimentation yielded 20 combinations of the 6 variable inputs which might produce an optimal system. Tables 3.1.2 and 3.1.3 list the variable input values for each of the 20 experimental systems for Ku-band and Ka-band respectively. Note that the atmospheric thickness is reduced for some cases which allows the PRF to increase accordingly. This reduction assumes that a waveform can be designed which can eliminate the atmospheric range ambiguities associated with a higher PRF.

A FORTRAN program was used to evaluate the Metrad system at each of the 20 variations at the 2 RF's (13.5 and 35 GHz). The evaluation was performed using a 1 mm/hr rain atmospheric model with no brightband over a land background. Four computed system parameters were used to compare and choose the optimal system. They are; (1) the number of real receive beams (channels), (2) the signal-to-noise ratio (dB), (3) the vertical boom length (meters), and (4) the signal excess (dB). Figure 3.1.3 is a chart of the four evaluation parameters over the 20 candidate systems at Ku-band. Note the high number of receive beams which corresponds to systems with range unambiguous PRF's. System #14 was chosen as the system which did the best job of minimizing the number of beams and the boom length while maximizing the signal-to-noise ratio and signal excess. Figure 3.1.4 shows the four evaluation parameters over the 30 candidate systems at Ka-band. System #16 was chosen as optimal at Ka-band.

Table 3.1.4 gives the optimal Ku-band system parameters. The system has a transmit azimuth beamwidth of 37 degrees resulting in a vertical boom width of .048 meters. The elevation beamwidth is 2.35 milliradians which requires a vertical boom length equal to 13.14 meters. The swathwidth is computed to be 207 km. The pulse-duration is .83 micro seconds, the PRF is 17.6 KHz, and the peak power is 8 kw which gives an average power equal to 117 watts. There are 16 real receive beams and channels.

Table 3.1.5 gives the optimal Ka-band system parameters. The vertical boom dimensions are 7.33 by .022 meters. The swathwidth is computed to be 206 km. The pulse-length is 1.2 micro seconds, the PRF is 19.15 KHz, and the peak power is 4 kw which yields an average power equal to 94 watts. There are 30 real receive beams and channels.

The signal excess of the optimal Ku-band and Ka-band systems evaluated across the environmental matrix is given in Table 3.1.6. The Ka-band system out-performs the Ku-band system for all of the atmospheric models except heavy rain. The Ka-band system is capable of detecting every cloud type except stratus which it misses by approximately 3 dB over land and sea.

3.1.2 Metrad Summary

The sensitivity of the Ka-band Metrad system is good, but the design is awkward. The design is not recommended for the sounder mission for the following reasons:

- (1) there are too many receiver channels (30)
- (2) the swathwidth cannot be increased without increasing the receiver complexity proportionately
- (3) the vertical boom is too long (7 meters)
- (4) the range ambiguous PRF necessitates a complicated, pulse compressed waveform.

The Metrad design is best for a higher resolution, limited swath, imaging type of sensor.

Table 3.1.1 Metrad Input Values

<u>Fixed Inputs</u>	<u>13.6 GHz</u>	<u>35.0 GHz</u>
Vertical Resolution (Km)	1.0	1.0
Horizontal Resolution (Km)	3.0	3.0
Transmitter Peak Power (Kw)	8.0	4.0
Average Power (w)	200.0	200.0
System Losses (dB)	5.7	5.7
Receiver Noise Figure (dB)	2.1	2.1
Receiver Noise Temp (*K)	500.0	800.0
Peak 2-way Elevation Sidelobe (dB)	-35.0	-35.0
Average Doppler Filter Sidelobe (dB)	-30.0	-30.0
Average Receive Azimuth Sidelobe (dB)	-35.0	-35.0
Swathwidth (Kw)	200.0	200.0

Variable Inputs

Transmit Azimuth Beamwidth (Deg)	20 - 70
Transmit Beam Center Angle (Deg)	0 - 90
Nadir Angle (Deg)	0 - 45
Satellite Altitude (Km)	300 - 800
Elevation/Beamwidth (Millirad)	= 1 - 3
Atmospheric Thickness (Km)	6 - 18

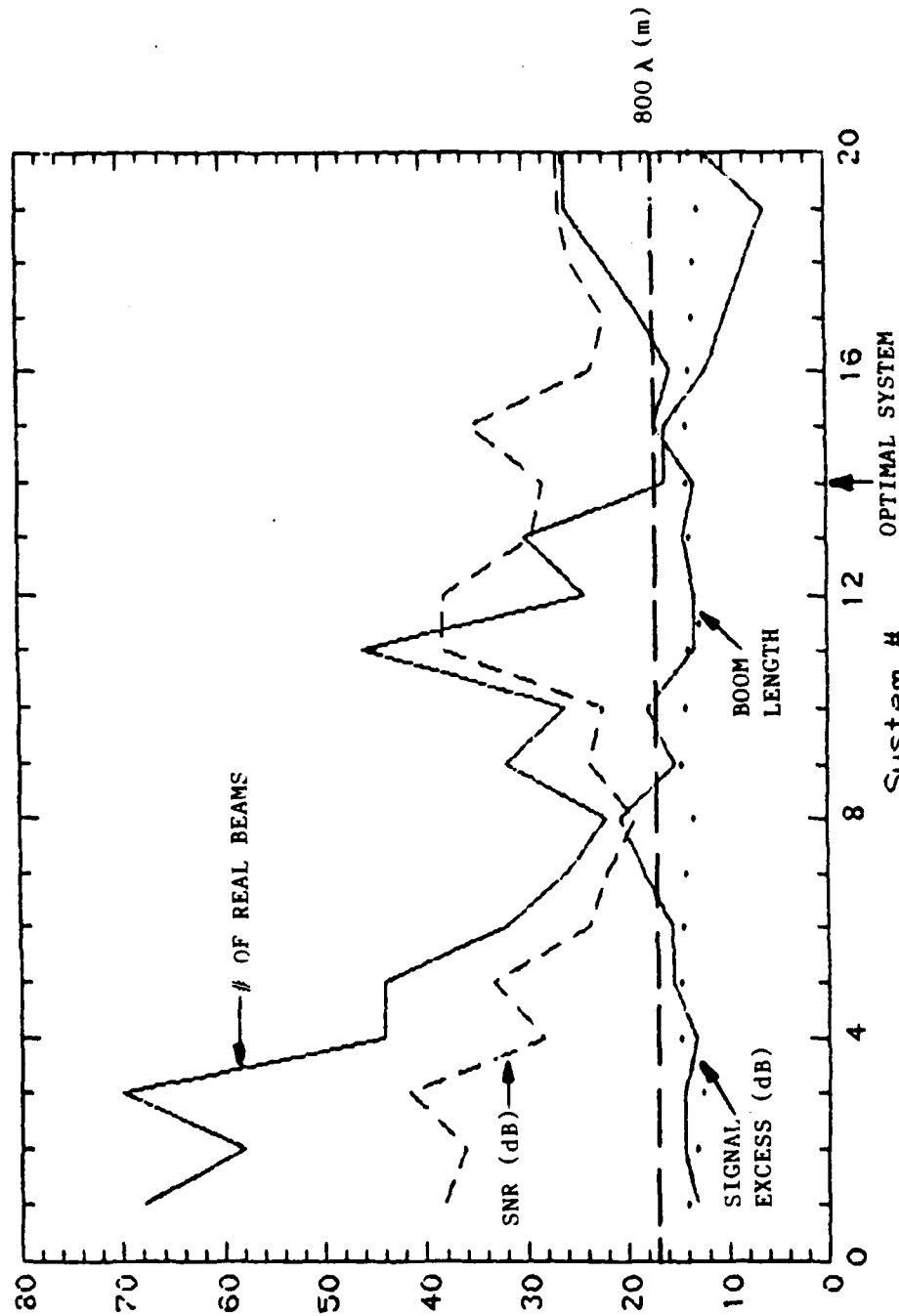
Table 3.1.2 Ku Variations (Baseline = #1)

System =	1	2	3	4	5	6	7	8	9	10	11	12	13	14	15	16	17	18	19	20
Variable																				
Transmit																				
Azimuth																				
Beamwidth (Deg)	50.0	50.0	57.0	36.0	36.0	28.0	23.0	20.0	27.0	22.5	50.0	50.0	40.0	37.0	37.0	29.0	26.0	20.50	18.0	18.0
Transmit																				
Beamcenter (Deg)	35.0	35.0	35.0	35.0	35.0	35.0	35.0	35.0	35.0	35.0	35.0	35.0	35.0	35.0	35.0	35.0	35.0	35.0	35.0	35.0
Beam																				
Angle (Deg)	45.0	40.0	40.0	45.0	45.0	45.0	45.0	45.0	46.0	46.0	45.0	45.0	41.0	45.0	45.0	45.0	45.0	45.0	45.0	45.0
Satellite																				
Altitude (Km)	300.0	350.0	300.0	400.0	400.0	500.0	400.0	700.0	500.0	600.0	300.0	300.0	400.0	400.0	400.0	500.0	600.0	300.0	600.0	400.0
Elevation																				
Beamwidth (Millirad)	2.35	2.35	2.35	2.35	2.00	2.00	1.70	1.50	2.00	1.69	2.35	2.35	2.35	2.35	1.80	2.00	1.70	1.40	1.20	1.20
Atmospheric																				
Thickness (Km)	18.0	18.0	18.0	18.0	18.0	18.0	18.0	18.0	18.00	18.00	12.0	6.0	12.0	6.0	6.0	6.0	6.0	6.0	6.0	12.0

Table 3.1.3 Ka Variations (Baseline = #1)

System =	1	2	3	4	5	6	7	8	9	10	11	12	13	14	15	16	17	18	19	20
Variable																				
Transmit																				
Azimuth																				
Beamwidth (Deg)	50.0	50.0	57.0	36.0	36.0	28.0	23.0	20.0	24.0	22.0	50.0	50.0	40.0	40.0	40.0	35.0	29.0	24.0	21.0	21.0
Transmit																				
Beamcenter (Deg)	35.0	35.0	35.0	35.0	35.0	35.0	35.0	35.0	35.0	35.0	35.0	35.0	35.0	35.0	35.0	35.0	35.0	35.0	35.0	35.0
Beam																				
Angle (Deg)	45.0	40.0	40.0	45.0	45.0	45.0	45.0	45.0	40.0	40.0	45.0	45.0	41.0	41.0	41.0	40.0	40.0	40.0	40.0	40.0
Satellite																				
Altitude (Km)	300.0	350.0	300.0	400.0	400.0	500.0	400.0	700.0	500.0	600.0	300.0	300.0	400.0	400.0	400.0	500.0	600.0	700.0	800.0	800.0
Elevation																				
Beamwidth (Millirad)	2.35	2.35	2.35	2.35	2.00	2.00	1.50	1.30	1.30	1.30	2.35	2.35	2.35	2.35	1.80	1.60	1.40	1.40	1.20	1.20
Atmospheric																				
Thickness (Km)	18.0	18.0	18.0	18.0	18.0	18.0	18.0	18.0	18.00	18.00	12.0	6.0	12.0	6.0	6.0	6.0	6.0	6.0	6.0	6.0

Figure 3.1.3 Metrad, 20 Ku-Band Systems



System Optimization Run
 aeta=-63dB/M, Land Clutter
 1 mm/hr rain, no brightband
 Attenuation=.05dB/KM

Figure 3.1.1.4 Metrad, 20 Ka-Band Systems

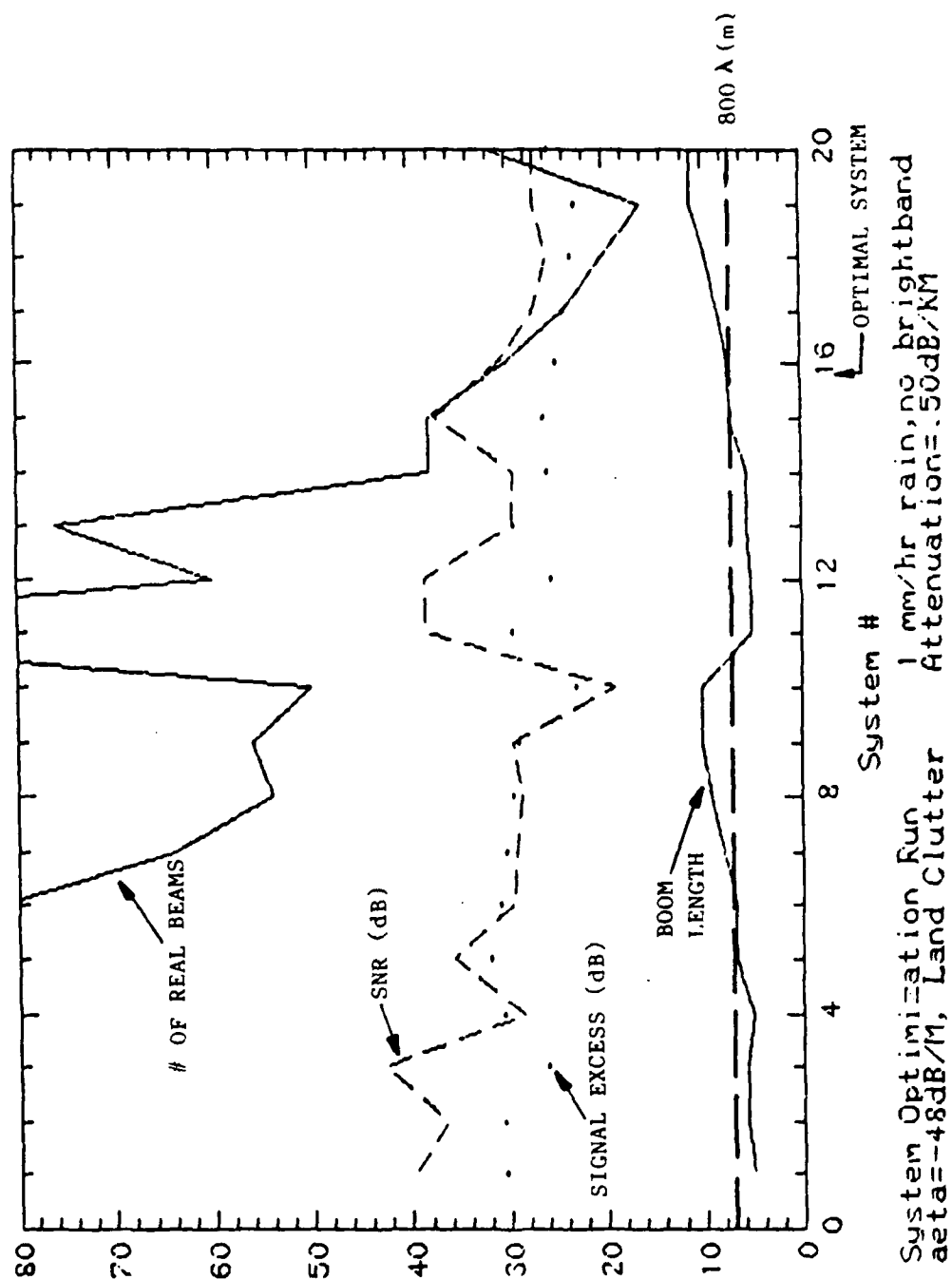


TABLE 3.1.4 OPTIMAL KU-BAND SYSTEM

METRAD INPUT VALUES

XMIT FREQUENCY (MHZ)	13600.00
AZIMUTH BEAMWIDTH (DEG)	37.00
BEAM CLUTTER ANGLE (DEG)	35.00
RADAR ANGLE (DEG)	45.00
SATELLITE ALTITUDE (KM)	400.00
VERTICAL RESOLUTION (KM)	1.00
HORIZONTAL RESOLUTION (KM)	3.00
ELEVATION BEAMWIDTH (MILLIRAD)	2.35
ATMOSPHERIC THICKNESS (KM)	6.00
SURFACE CLUTTER COEFF (DB)	-10.00
TRANSMITTER PEAK POWER (KW)	8.00
AVERAGE POWER CONSTRAINT (W)	200.00
ATMOS VOLUME REF COEFF (DB)	-.63E+02
2-WAY ATTENUATION COEFF (DB/KM)	.05
SYSTEM LOSSES (DB)	5.70
RECEIVER NOISE FIGURE (DB)	2.10
CLOUD THICKNESS (KM)	4.00
RECEIVER NOISE TEMPERATURE (K)	500.00

METRAD OUTPUT VALUES

TRANSMIT ANTENNA WIDTH (M)	.04B
SATELLITE VELOCITY (1 M/S)	7.664
SWATHWIDTH (KM)	207.937
ENVIRONMENT BANDWIDTH (KHZ)	178.850
VERTICAL BOOM LENGTH (M)	13.142
PULSE LENGTH (SEC)	83E-06
ROUND TRIP PROPACATION TIME (SEC)	.19E-02
TRANSMIT ANTENNA GAIN (DB)	58.267
ENVIRONMENT TIME-BANDWIDTH PRODUCT	10.117
NUMBER OF REAL RECEIVE BEAMS	16.000
RELEIVE ANTENNA APERTURE (M)	1.029
MINIMUM RECEIVE BEAMWIDTH (DEG)	2.432
MAXIMUM RECEIVE BEAMWIDTH (DEG)	2.546
MINIMUM RECEIVE BANDWIDTH (KHZ)	6.664
MAXIMUM RECEIVE BANDWIDTH (KHZ)	17.551
MINIMUM RECEIVE TIME-BANDWIDTH PRODUCT	.351
MAXIMUM RECEIVE TIME-BANDWIDTH PRODUCT	.976
PRF (KHZ)	17.678
# OF SYNTHETIC BEAMS PER REAL BEAM(WRST CSE)	8.66
TIME NECESSARY FOR DOPPLER PROCESSING (SEC)	13E-02
NUMBER OF PULSES COHERENTLY INTEGRATED	22.97
BURST REPETITION FREQUENCY (HZ)	769.50
SIGNAL ENERGY (JOULES)	.15
AVERAGE POWER (WATTS)	117.36
RECEIVE ANTENNA GAIN (DB)	52.31
SIGNAL-TO-NOISE RATIO (DB)	28.09
SIGNAL-TO-SURFACE-CLUTTER RATIO (DB)	12.33
SIGNAL-TO-PULSE-DOPPLER-SIDELobe RATIO (DB)	17.22
SIGNAL-TO-AMBIGUITY-LOBE-CLUTTER RATIO (DB)	24.95
SIGNAL-TO-CLUTTER-PLUS-NOISE RATIO (DB)	10.85

TABLE 3.1.5 OPTIMAL Ka-BAND SYSTEM

XMIT FREQUENCY (MHZ)	35000.00
AZIMUTH BEAMWIDTH (DEG)	35.00
BEAM CENTER ANGLE (DEG)	35.00
RADAR ANGLE (DEG)	40.00
SATELITE ALTITUDE (KM)	500.00
VERTICAL RESOLUTION (KM)	1.00
HORIZONTAL RESOLUTION (KM)	3.00
ELEVATION BEAMWIDTH (MILLIRAD)	1.00
ATMOSPHERIC THICKNESS (KM)	6.00
SURFACE CLUTTER COEFF (DB)	-13.00
TRANSMITTER PEAK POWER (KW)	4.00
AVERAGE POWER CONSTRAINT (W)	200.00
ATMOS VOLUME REF COEFF (DB)	-.48E+02
2-WAY ATTENUATION COEFF (DB/KM)	.50
SYSTEM LOSSES (DB)	5.70
RECEIVER NOISE FIGURE (DB)	2.10
CLOUD THICKNESS (KM)	4.00
RECEIVER NOISE TEMPERATURE (K)	800.00

METRAD OUTPUT VALUES

TRANSMIT ANTENNA WIDTH (M)	.022
SATELLITE VELOCITY (KM/S)	7.608
SWATHWIDTH (KM)	206.690
ENVIRONMENT BANDWIDTH (KHZ)	393.624
VERTICAL BOOM LENGTH (M)	7.334
PULSE LENGTH (SEC)	.12E-05
ROUND TRIP PROPAGATION TIME (SEC)	.22E-02
TRANSMIT ANTENNA GAIN (DB)	60.080
ENVIRONMENT TIME-BANDWIDTH PRODUCT	20.554
NUMBER OF REAL RECEIVE BEAMS	30.000
RECEIVE ANTENNA APERTURE (M)	.925
MINIMUM RECEIVE BEAMWIDTH (DEG)	1.156
MAXIMUM RECEIVE BEAMWIDTH (DEG)	1.205
MINIMUM RECEIVE BANDWIDTH (KHZ)	7.456
MAXIMUM RECEIVE BANDWIDTH (KHZ)	18.905
MINIMUM RECEIVE TIME-BANDWIDTH PRODUCT	377
MAXIMUM RECEIVE TIME-BANDWIDTH PRODUCT	979
FRF (KHZ)	19.151
# OF SYNTHETIC BEAMS PER REAL BEAM (WRST CSE)	4.71
TIME NECESSARY FOR DOPPLER PROCESSING (SEC)	.63E-03
NUMBER OF PULSES COHERENTLY INTEGRATED	12.10
BURST REPETITION FREQUENCY (HZ)	1583.19
SIGNAL ENERGY (JOULES)	.06
AVERAGE POWER (WATTS)	94.63
RECEIVE ANTENNA GAIN (DB)	57.13
SIGNAL-TO-NOISE RATIO (DB)	30.78
SIGNAL-TO-SURFACE-CLUTTER RATIO (DB)	30.16
SIGNAL-TO-PULSE-DOPPLER-SIDELobe RATIO (DB)	20.92
SIGNAL-TO-AMBIGUITY LOBE-CLUTTER RATIO (DB)	24.17
SIGNAL-TO-CLUTTER-PLUS-NOISE RATIO (DB)	18.63

TABLE 3.1.6 METRAD PERFORMANCE (SIGNAL EXCESS)
Ka/Ku

	LAND	SEA	SNOW
LIGHT RAIN	24.83/13.85	24.83/15.75	22.7/11.52
MELTING LAYER W/LIGHT RAIN	24.50/13.84	24.50/15.74	22.49/11.52
HEAVY RAIN	19.04/19.36	19.04/19.44	19.02/19.19
STRATUS	-2.84/-22.61	-2.84/-19.71	-10.93/-25.55
CIRRUS	16.82/-3.62	16.82/- .75	9.03/-6.56

Scanning Altimeter Tradeoffs and Frequency Selection

This section summarizes the preliminary design calculations for the so called scanning altimeter type of radar sounder. In fact the scanning design will have little in common with the typical satellite altimeter other than a pencil beam antenna. Since the resolution requirements are dramatically different (e.g., 1 km vs a fraction of a meter) the system will be unlikely to use pulse compression which is considered to be undesirable. Further, rather than looking in a fixed nadir direction, the sounder must scan a significant swath (200 - 600 km). Finally, the low level of signals which must be detected requires a significantly larger antenna. For these reasons, the study did not start with an existing altimeter, but began with basic requirements and attempted to evolve a design to meet those requirements.

Table 3.2.1 outlines the steps in the design procedure. The first step is to define the nominal limits of what can be achieved with the 1988 radar state-of-the-art (SOTA), and what are the typical weather environments for which the radar must provide reasonable performance. Initial estimates of these quantities were refined during a three day workshop at TSC. Table 3.2.2 summarizes the nominal radar parameters used for these calculations.

As can be seen, four frequency bands have been considered. This range of frequencies span the range of potential weather measurement systems. Below Ku band (13.6 GHz) the cloud backscatter coefficients would be expected to be too small for successful operation. Further, antenna sizes required to achieve the required resolution become excessive. Above 140 GHz, the atmospheric and water attenuation would be too great even in light rain.

The clear air loss listed in the table is the two way loss through the troposphere at normal incidence. Additional attenuation through the rain or clouds is added to that loss. The distribution loss applies only to surface clutter limited situations. This is an additional factor to account for the fact that even with a fairly large foot print and reasonably large incidence angles, the surface clutter return deviates slightly from a Rayleigh distribution. Typically, the detection threshold has to be adjusted upwards to maintain acceptable false alarm rates in such environments.

Table 3.2.3 shows the environments considered in the preliminary design. These are intended to span a reasonable range of environment types. The important radar parameters are the cloud or rain thickness, the reflectivity, and the attenuation. The top of the heavy rain cloud is easily detectable at all frequencies; however, due to high attenuation, the bottom is not easily detectable at the higher frequencies. At the other extreme, the low stratus cloud is a difficult target at all frequencies due to its low reflectivity. With its high water content (and corresponding attenuation) the normal payoff achieved by going to higher frequency is largely nullified. The light rain and high cirrus environments are between the two extremes. Section 3.4 gives the surface clutter model used in the study.

TABLE 3.2.1 RADAR SOUNDER: SCANNING "ALTIMETER" PRELIMINARY DESIGN

- SPECIFY NOMINAL RADAR PARAMETER LIMITS AND CHARACTERIZE ENVIRONMENT
- DEVELOP DESIGN EQUATIONS AND ORDER USING PRECEDENCE MATRIX
- OPTIMIZE ANTENNA AND WAVEFORM
- COMPUTE NOMINAL PERFORMANCE AND SELECT CANDIDATE SYSTEM
- INVESTIGATE VARIATIONS WHICH ALLOW DETECTION OF STRATUS CLOUDS

TABLE 3.2.2 NOMINAL RADAR/SATELLITE PARAMETER LIMITS

RESOLUTION:

Altitude	1 km
Horizontal	6 km goal in clouds

ORBIT:

High Orbit	833 km
Low Orbit	300 km

SWATH:

Max.	600 km
Min.	200 km

RADAR:

Freq. (GHz)	13.6	35.0	94.0	140.0
Peak Power (kw)	8.0	4.0	1.0	0.2
Avg. Power (w)	200.0	200.0	100.0	20.0
System Temp (*K)	500.0	700.0	1200.0	1500.0
Antenna Dia. (m)	6.6	2.6	0.9	0.6
System Losses*	5.7	5.7	6.7	6.7
Distribution Loss**	1.0	1.0	1.0	1.0
Clear Air Loss	0	0.5	1.0	3.5

*Ohmic receive loss included in system temperature.

**Nominal detectability loss when surface clutter greatly exceeds system noise.

TABLE 3.2.3

RAIN AND CLOUD MODELS

-- α is for one way propagation-- in light rain α includes melting layer
attenuation

Observable	Frequency			
	Ku 13.6GHz	Ka 35.6GHz	W 94GHz	-- 140GHz
Heavy Rain				
η (dBm ⁻¹)	-45	-32	-35	-37
α (dB/km)	0.6	4.4	7.0	8.9
Δh (km)	4.0	4.0	4.0	4.0
Light Rain				
η (dBm ⁻¹)	-63	-48	-43	-39
α (dB/km)	.09	.70	1.8	2.3
Δh (km)	4.0	4.0	4.0	4.0
Cirrus				
η (dBm ⁻¹)	-82	-65	-48	-41
α (dB/km)	0	0	0	0
Δh (km)	1.0	1.0	1.0	1.0
Stratus 1				
η (dBm ⁻¹)	-101	-85	-69	-62
α (dB/km)	.05	.40	1.4	2.1
Δh (km)	1.0	1.0	1.0	1.0
Stratus 2				
η (dBm ⁻¹)	-106	-90	-74	-67
α (dB/km)	0	.04	.10	.20
Δh (km)	.30	.30	.30	.30

The second step in the design process is to develop the system design equations. Here it is assumed that the principal problem to be solved is that of detection. Thus the performance criteria chosen is signal excess (E^*). This is defined as the ratio (in dB) of the signal to total interference (noise plus surface clutter) divided by the minimum required signal-to-noise ratio. The ratio is computed in somewhat unusual way shown below so that a separate accounting of SNR and SCR can be maintained.

$$E^* = \frac{\left[\left(\frac{P_v}{N} \right)^{-1} + \left(\frac{P_v}{C} \right)^{-1} \right]^{-1}}{D_{np}}$$

E^* - Excess Signal
 P_v - Volume (rain or cloud) Return
 N - Noise Power
 C - Clutter Power
 D_{np} - Minimum Required SNR

Computation of the SNR is a straight forward application of the meteorological radar equation as shown on Table 3.2.4. For these computations Z_e is the equivalent radar Z , not the meteorological Z . It is simply a surrogate for the reflectivity as defined on the bottom of the table.

Computation of the SCR requires including surface scattering from three portions of the surface as shown on Fig. 3.2.1. As shown in the chart, the primary interference is below the rain cell of interest on the constant range arc.

Here the surface clutter is attenuated only by the principal axis sidelobes of the antenna. The second area of interest is the complete ring of return centered around the nadir point of the satellite. This ring is defined by the intersection of the constant range sphere through the rain cell and the surface. Although this energy is attenuated by the (generally lower) off principal axis sidelobes of the antenna, the large area included in the ring can produce significant total backscatter. Finally, in pulse compression systems, the range sidelobes of the pulse will reach on down to the surface and pick up significant interference. Since the range sidelobes are only "one-way" attenuation this contribution generally overwhelms the interference through the antenna sidelobes. Table 3.2.5 gives the equations used for computing SCR.

The approximate equations used to calculate SCR only apply at off nadir scan angles. Thus the evaluations given here are limited to a minimum horizontal distance from the nadir point of about 10-25 km. At nadir the antenna sidelobe response is of little interest as surface scatter into these sidelobes always occurs at ranges greater than that of the rain or cloud cell of interest. The only important nadir interference is from the

TABLE 3.2.4

DESIGN EQUATIONS: SNR

$$\frac{P_v}{N} = \frac{\pi^3 c |K|^2}{512k} \frac{P_t C_r}{L_v T_s} \left(\frac{G \theta \tau}{\lambda} \right)^2 \frac{z_e}{R^2}$$

P_t = peak transmit power

C_r = pulse compression ratio

G = antenna gain

θ = antenna beamwidth

τ = compressed pulse length

L_v = total losses excluding L_{Dist} (i.e. system
+ atmos. + cloud)

T_s = system temperature

λ = RF wavelength

R = range to rain or cloud

c = speed of light

$|K|^2 \equiv 0.93$

k = Boltzman's constant

z_e = equivalent radar Z

$$\eta \equiv \frac{\pi^5 |K|^2 z_e}{\lambda^4}$$

FIGURE 3.2.1

ILLUSTRATION OF SOURCES OF SURFACE INTERFERENCE

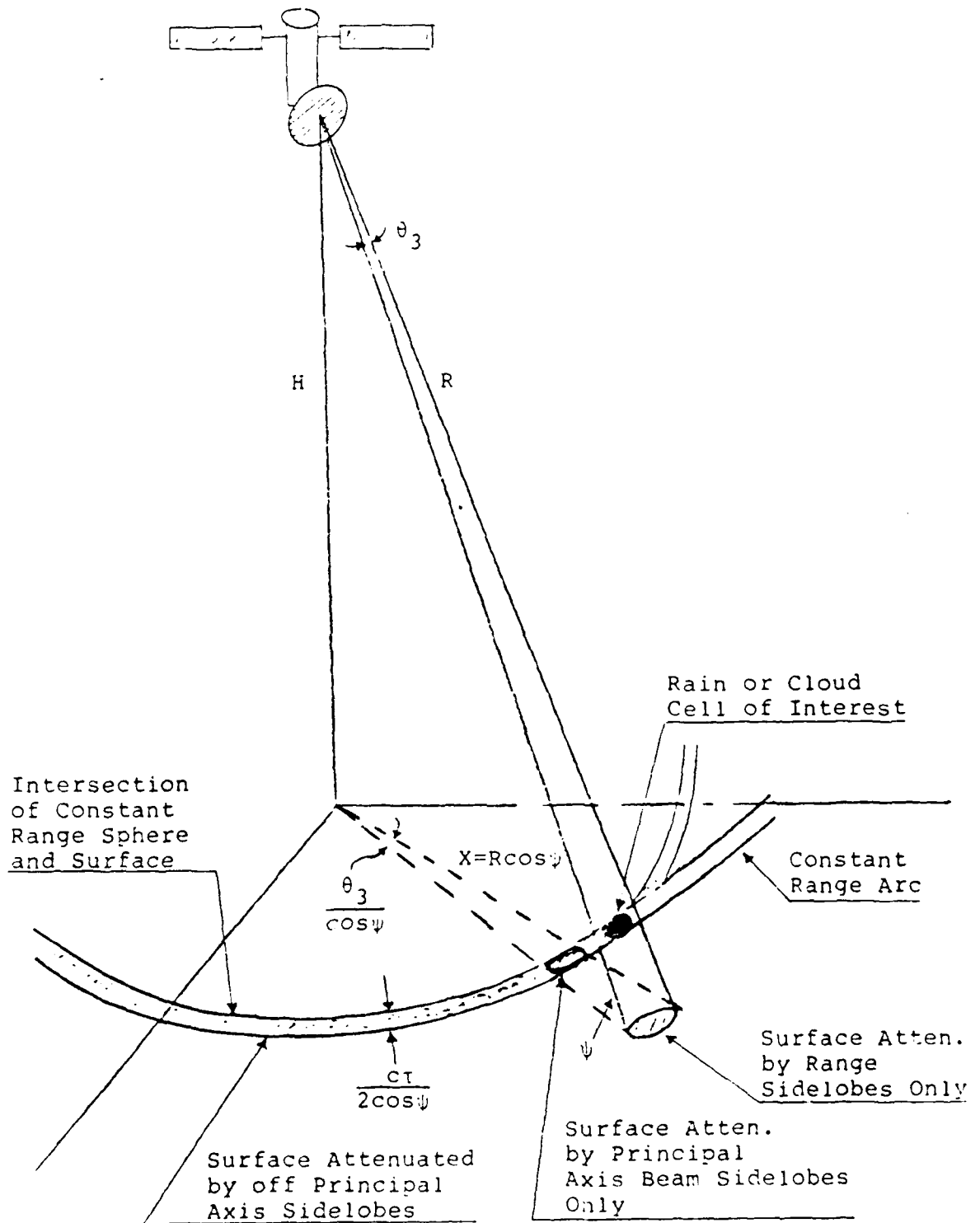


TABLE 3.2.5

DESIGN EQUATIONS: SCR

$$SCR = \frac{-6|K|^2}{4} \frac{\theta}{\lambda^4} \frac{RZ \cos \psi}{\sigma_o L_{Dist}} \left[\frac{1}{S_{bo}^2} + \frac{2\pi x_c}{\theta R S_{bl}^2} + \frac{A_3}{S_p A_1} \right]^{-1}$$

$$\frac{A_3}{A_1} = \frac{\pi}{2c} \frac{R\theta}{\tan \psi} \quad \text{Beam Limited}$$

$$= C_r \quad \text{Pulse Limited}$$

- ψ = grazing angle
 σ_o = surface scattering at angle ψ
 L_{Dist} = distribution loss
 S_{bo} = antenna (one-way) principal axis
sidelobes
 S_{bl} = antenna (one-way) off principal
axis sidelobes
 S_p = pulse compression sidelobes
 x_c = horizontal distance to rain or
cloud cell

pulse compression sidelobes. For a system without range sidelobes, surface scattering at nadir look angles can be neglected.

In the following design analysis a linear scan back and forth across the sub-satellite point is assumed. Thus, for example, a 200 km swath is obtained by scanning ± 100 km about nadir. For systems with pulse compression, there could be a narrow region about nadir where the calculations given here may be optimistic. For systems without pulse compression (as will ultimately be recommended) the surface return at nadir is not a problem and the performance estimates given represent worst case.

Evaluation of the signal excess requires the evaluation of a large number of auxiliary parameters each of which may have various constraints applied to them. The first pass through the design identified 46 equations, constraints, and variables in the system design. Precedence matrices were used to organize them into input variables, output variables, and system equations, and to order the computations into a logical efficient order of evaluation.

Early in the design, it was discovered that a key constraint was on the waveform PRF and the antenna scan rate. For a straight forward linear scanning system, the antenna must scan across the swath width in the time it takes the satellite to move forward one resolution cell. This implies a high scan rate on the order of 100 deg/sec. At the same time, in a single frequency system, the maximum useful PRF is limited by the decorrelation time it takes the satellite to move one-half an antenna diameter. At Ku band this implies a PRF limit of about 2300 Hz. The combination of high scan rate and limited PRF results in relatively few pulses per beam and a correspondingly limited performance.

At the other extreme, if the system employs either frequency or beam agility to decorrelate the return, then the maximum PRF is limited only by the duty cycle of the transmitter tube. For the same Ku band case, the maximum PRF is 12.5 KHz, and the total number of pulses which can be placed in a resolution cell before the satellite moves on is 73 for 3 km resolution.

The required principal sidelobe requirement at Ka is nearly 35 dB below peak gain. This is a direct result of the somewhat greater reflectivity of the refrozen snow background as compared to the original land background used. The off principal (rms) sidelobes were dramatically reduced in all cases. A simple argument shows that the rms sidelobes must be on the order of the antenna gain. That is, for a pencil beam we may write the antenna gain as:

$$G = \frac{4\pi}{B(\theta, \phi) d\Omega} \approx \frac{4\pi}{\theta^2 + \frac{4\pi - \theta^2}{SL}} \quad (1)$$

where $B(\theta, \phi)$ is the beam pattern,
 $d\Omega$ is the differential of solid angle,
 θ is the effective beamwidth,

and SL is the rms sidelobe level.

Solving this equation for sidelobe level yields:

$$SL = \frac{(1-\theta^2/4\pi)G}{1-\eta} \approx \frac{G}{1-\eta} \geq G \quad (2)$$

where $\eta = G/(4\pi/\theta^2)$ is the antenna efficiency.

Thus the rms sidelobes must be at least equal to the antenna gain. Using the conservative assumption that in the cone of interest, sidelobes could rise as much as 3 dB, the rms sidelobes were set at 55 dB for the calculations. At this level, the rms sidelobes produce no contribution to the clutter background.

The optimization was performed for Stratus 2 clouds against a refrozen snow background. Based on the inputs from Table 3.2.6 the results are given in Table 3.2.7. As can be seen, at Ku band, the system is roughly balanced between being noise and clutter limited, at Ka band the system is noise limited. In the higher bands, (94 and 140 GHz), the systems are clutter limited. This is due to surface clutter leaking through the pulse compression range sidelobes.

Table 3.2.8 compares the performance of all four systems (with a land background) against the five rain and cloud models. That table shows the clear superiority of the Ka system. It has the greatest signal excess against the weak stratus clouds, while still having good margin in both the rain environments.

Table 3.2.9 shows the effect of the background. For the (principal) antenna sidelobe levels chosen, the Ka system is not limited by clutter background. No significant difference appears between various background types.

Figure 3.2.2 shows the effect of peak sidelobe levels on signal excess for the two stratus cloud targets with both land and snow backgrounds. As can be seen, the point of diminishing returns is reached for sidelobe levels of 35 dB and lower. If (as was done last quarter) only land background is considered, 30 dB peak sidelobes would be sufficient. The stronger snow background, however, forces the lower sidelobe levels. Note that the 55 dB rms sidelobes contribute nothing to the interference in any of the environments. Apparently, only the peak sidelobe levels are important.

The frequency selection result from this optimization applies to other configurations as well. The attenuation at 94 GHz and higher rule out measurements in heavy rain and thus would not lead to a practical system. If a 5 kw transmitter were available at 94 GHz, pulse compression would not be necessary, and that frequency would be more competitive. Perhaps a practical gyration may be available in the 1990's. The cloud sensitivity is not adequate at Ku band.

The above calculations were made earlier in the study and it will be shown in later sections that it is practical to have larger apertures and better sensitivity.

TABLE 3.2.6
INPUT PARAMETERS FOR OPTIMIZED SYSTEMS

Symbol	Name	14GHz	36GHz	94GHz	140GHz
RADAR:					
λ cm	RF Wavelength	2.20	.86	.31	.21
P_t kw	Transmit Pwr.	8.0	4.0	1.0	.2
C_r	Compression Ratio	1.0	1.0	32.0	32.0
τ μ sec	Compressed Pulse	3.6	3.8	3.8	3.7
δ %	Duty Factor	2.5	5.0	10.0	10.0
S_p dB	PC Sidelobe Level	none	none	35.0	35.0
S_{bo} dB	Sidelobe Level (1way)	35.0	35.0	25.0	25.0
S_{bl} dB	Off Prin. Axis SL	55.0	55.0	55.0	55.0
D_{max} m	Antenna Dia.	6.6	2.6	.9	.6
L_{dist} dB	Dist. Loss in Clt.	1.0	1.0	1.0	1.0
T_s °K	System Temperature	500.0	700.0	1200.0	1500.0
L_o dB	System Losses	5.7	5.7	6.7 ⁺	6.7 ⁺
L_{CFAR} dB	CFAR Loss	1.0	1.0	1.0	1.0
P_d	Detection Prob.	.9	.9	.9	.9
L_{pfa}	Log P_{fa}	-6.0	-6.0	-6.0	-6.0
REQUIREMENTS:					
Δx km	Hor. Res.	6.0	6.0	6.0	6.0
Δy km	Ver. Res.	1.0	1.0	1.0	1.0
x_c km	Crosstrack Rng.	100.0	100.0	100.0	100.0
S_w km	Swath	200.0	200.0	200.0	200.0
H km	Satellite Alt.	300.0	300.0	300.0	300.0
ENVIRONMENT :					
η dBm ⁻¹	Volume Reflectivity	-101.0	-85.0	-69.0	-62.0
α dB/km	Attenuation (1way)	.05	.4	1.4	2.1
Δh km	Rain Thickness	1.0	1.0	1.0	1.0
h_{max} km	Max. Cloud Ht.	18.0	18.0	18.0	18.0
S_{type}	Surface Type	Snow	Snow	Snow	Snow

* Stratus 1

+ With pulse compression

TABLE 3.2.7

OUTPUT PARAMETERS FOR RE-OPTIMIZED SYSTEMS

Symbol	Name	14GHz	36GHz	94GHz	140GHz
η_a	Antenna Efficiency	.77	.77	.91	.91
$\theta_s \lambda/D$	Beam Broadening	1.23	1.23	1.12	1.12
G dB	Antenna Gain	58.4	58.4	58.8	58.6
θ_3 deg	Antenna Beamwidth	.234	.222	.221	.225
ψ deg	Grazing Angle	67.2	67.2	67.2	67.2
ρ_x	Frac. Hor. Res.	.23	.23	.23	.23
ρ_y	Frac. Ver. Res.	1.00	1.02	1.00	.99
v_s km/s	Satellite Velocity	7.7	7.7	7.7	7.7
R km	Slant Range	317.0	317.0	317.0	317.0
f_{prf} kHz	PRF	6.9	13.2	.8	.8
n_p	No. of Pulses/res	161.5	306.0	19.1	19.6
D_{np} dB	Min. Req. SNR	-2.7	-4.2	3.3	3.2
σ_o dB	Surf. Reflec.	-6.1	-0.1	-0.1	-0.1
L_v dB	Vol. Loss Fac.	6.8	7.6	10.7	12.3
SCR dB	Sig.-to-clutt.	-0.1	9.7	-7.9	-1.0
SNR dB	Sig.-to-noise	-2.5	0.5	11.5	5.3
E^* dB	Excess	-1.9	4.2	-11.3	-5.2

TABLE 3.2.8

SIGNAL EXCESS IN DB VS FREQUENCY

- 300λ Antenna
- Altitude 300km
- Reoptimized Waveforms (Table II)
- Horizontal Range = 100km (\pm 1/2 swath)
- Land Background

Observable	Frequency			
	Ku 13.6GHz	Ka 35.6GHz	W 94GHz	-- 140GHz
Heavy Rain	50.3	20.5	-15.5	-43.6
Light Rain*	35.7	36.4	19.6	9.6
Cirrus	17.2	25.5	18.6	23.6
Stratus 1	-1.8	4.6	-2.5	0.2
Stratus 2	-12.0	-4.8	-12.6	-7.6

* Includes attenuation due to melting layer.

TABLE 3.2.9

SIGNAL EXCESS IN DB VS BACKGROUND

-- 300 λ Antenna *
-- Ka Band
-- 300km Altitude
-- $x_c = 100\text{km}$

	Land	Snow	Sea
Heavy Rain	20.5	20.5	20.5
Light Rain	36.6	36.5	36.6
Cirrus	25.5	25.0	25.5
Stratus 1	4.6	4.2	4.6
Stratus 2	-4.8	-5.3	-4.8

* Increased to 500 λ in later sections.

SIGNAL
EXCESS
IN
dB

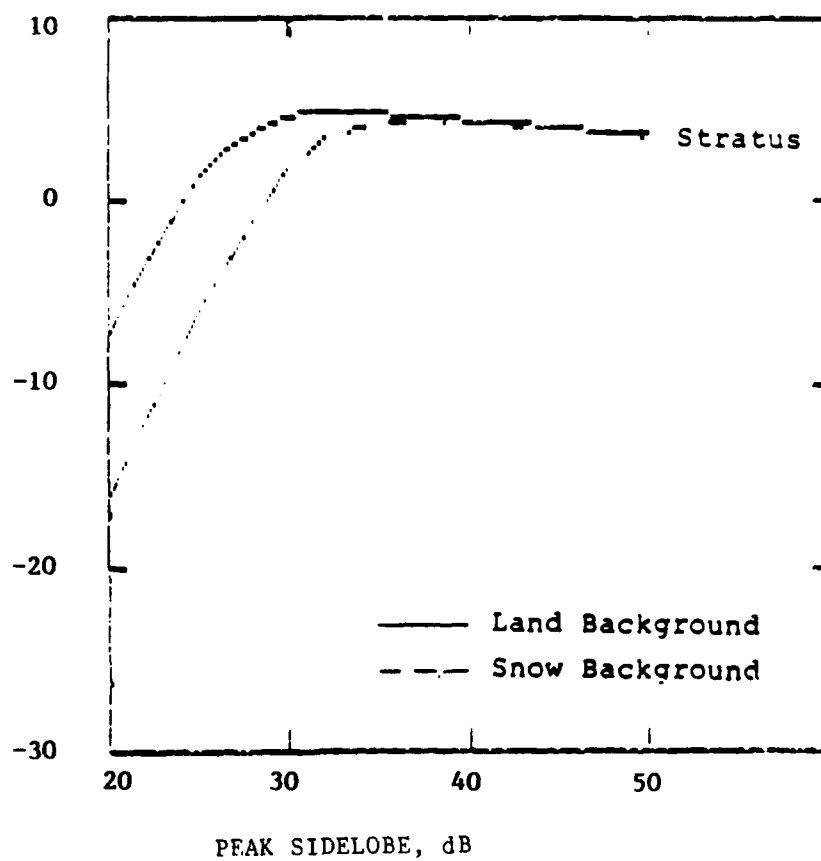


FIGURE 3.2.2 Effect of peak sidelobe level on performance,
Ka band (35.6GHz), $x_c = 100\text{km}$.

3.3 SYNTHETIC APERTURE (METSAR) MODE ASSESSMENT SUMMARY

This section explores the use of a synthetic aperture radar, designated METSAR, to determine cloud base altitudes for non-precipitating clouds. Aligned with this objective are other requirements associated with the collection of synoptically useful data sets. It is important to obtain a large enough field of view or swath width such that meteorological events are encompassed (100's of kilometers) and to sample a global data set often enough to make the data operationally useful.

3.3.1 SYNTHETIC APERTURE RADAR PRINCIPLES

A synthetic aperture radar collects a coherent data set and subsequently processes this data to form a high resolution image. Unlike diffraction limited remote sensors, such as the real aperture radar described in Section 3.2, whose cross-range spatial resolution is dependent on the radar wavelength, antenna dimension and range from the radar to the target, a SAR can achieve a fine spatial resolution independent of radar wavelength and target range.

$$\text{SPATIAL RESOLUTION (RAR)} = \frac{\text{WAVELENGTH X RANGE}}{\text{ANTENNA DIMENSION}}$$

$$\text{SPATIAL RESOLUTION (SAR)} = \frac{\text{ALONG TRACK ANTENNA DIMENSION (D}_{AT})}{2}$$

However, to achieve this fine spatial resolution, the SAR must integrate the collected data set over a dwell period that is equal to the time required for the radar to fly through the diffraction limited projection of the real beam at the target area.

$$\text{DWELL TIME} = \frac{\text{WAVELENGTH X RANGE}}{\text{ANTENNA DIMENSION X SATELLITE GROUND VELOCITY}}$$

This time is usually several orders of magnitude larger than the decorrelation time associated with meteorological events such as the cloud detection that is the focus of this study. After looking at METSAR performance at several frequencies, the study selected Ka band (35 GHz) as the preferred frequency. Typical SAR dwell times associated with 35 GHz and the synthetic apertures created by the 4 meter antennas studied in this report are a few tenths of a second. Although these times will vary as a function of target range, satellite velocity (orbital altitude) and specific antenna sizing, they are much larger than the meteorological target decorrelation times which are typically two orders of magnitude smaller. Section 3.2 calculated a range of decorrelation times. For the parameters used to study the METSAR approach, a decorrelation time of approximately .0017 seconds was used. To combat this large time difference, the SAR will only coherently integrate over the shorter time period (resulting in a multilook SAR) with the result that spatial resolution, the usual reason for using SAR techniques, degrades by the ratio of the target decorrelation time to the fully focused SAR dwell time. This ratio is equal to the number of looks described in Section 3.3.2. In addition to the loss of spatial

resolution, the signal-to-noise performance is correspondingly affected due to the sharp reduction in coherent processing or integration gain.

SAR systems have other limitations that influence their use for applications that require broad area or large swath coverage. A SAR must avoid both range ambiguities, the same as a RAR, and Doppler ambiguities. This condition imposes a lower bound restriction on antenna area. Thus, the SAR antenna must exceed some minimum area. This condition limits the swath width for SAR in many applications such that in its generic form, which is a fixed antenna that is pushbroom scanned by satellite motion, the SAR is not a wide swath width system. Examples of previous and planned space-based SAR sensors confirm this.

1. SEASAT, 1978, 100 km SWATH WIDTH
2. SIR-B, 1984, 40 km SWATH WIDTH
3. ERS-1, 1990, 80km SWATH WIDTH

The following sections provide more detailed descriptions of these limitations in the context of study objectives. Two specific SAR designs are studied for the determination of cloud base altitudes. The first design, described in Section 3.3.2 uses a fixed beam or strip mapping approach as shown in Figure 3.3.1. In this design, the antenna beam is oriented 90° to the direction of flight and remains at some fixed incidence angle using the moving satellite to accomplish the along-track scan. The second design, shown in Figure 3.3.2 and described in Section 3.3.3, also uses a beam at 90° to the line of flight but varies the incidence angle, within the constraints of target decorrelation timing, to increase swath coverage. A third operating mode is evaluated in Section 3.3.4. This mode would use the SAR as a higher resolution cloud imager capable of 100 meter performance or less. The small swath width attendant with this application makes this mode useful only as an adjunct or submode to the scanning altimeter described in Section 3.2, but might provide important data about fine scale cloud structures.

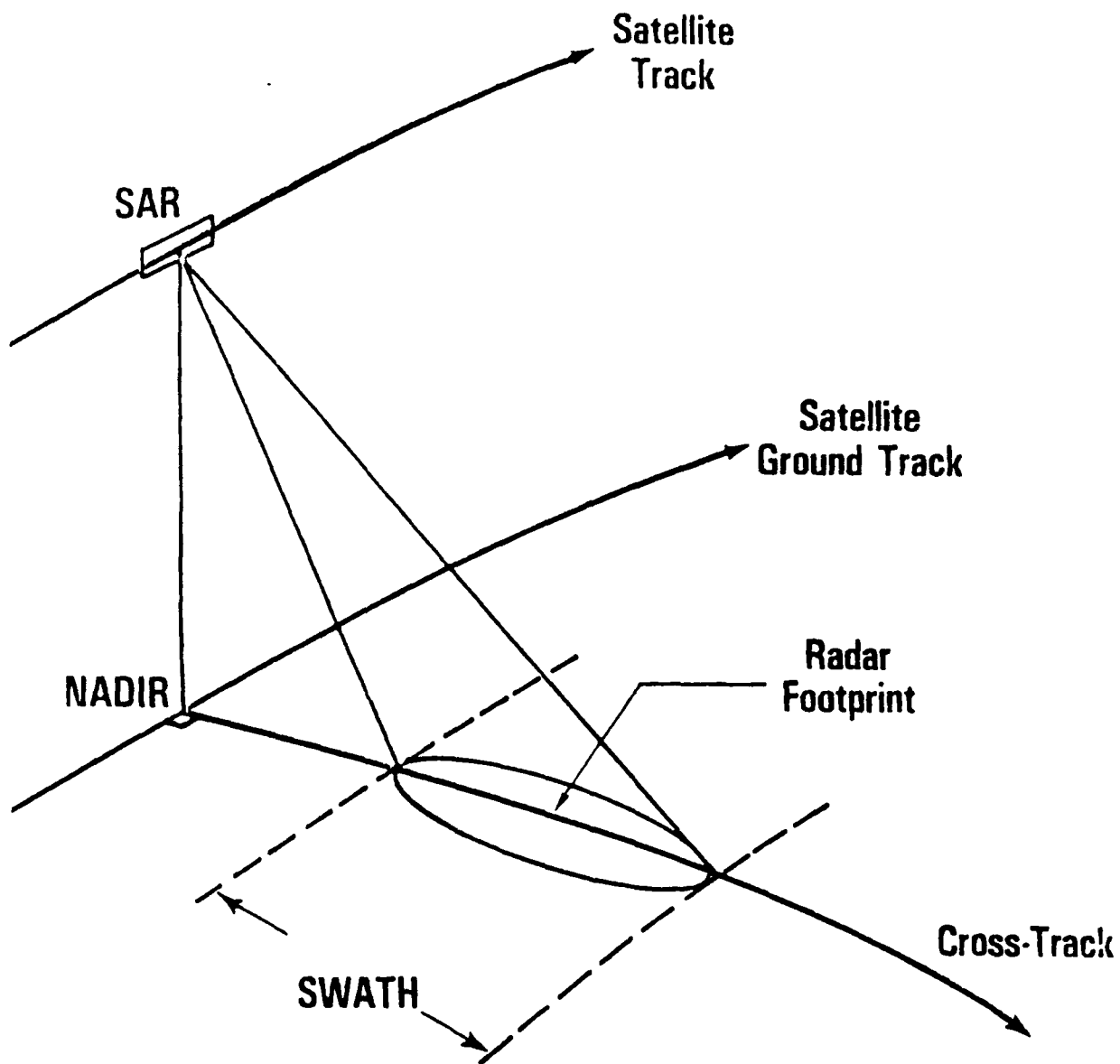
3.3.2 SYSTEM OPERATING CRITERIA - STRIP MAPPING MODE

It was decided to focus on 35 GHz and use a fixed SAR beam pointed broadside (90°) to the direction of flight as shown in Figure 3.3.1. The maximum antenna length along track (D_{AT}) = 4.4m (see Section 4.1) with a Corporate phased array (rectangular). The fixed beam maximizes swath width using a cross-track antenna dimension very nearly equal to that produced by the minimum antenna area to avoid ambiguities which is:

$$A_{MIN} = 4v\lambda RTAN\phi_i/c$$

- v = satellite velocity
- λ = wavelength = .00857m
- R = range to target area
- ϕ_i = incidence angle the complement of grazing angle
- c = the speed of light

$$D_R \geq A_{MIN}/4.4M$$



SAR IMAGING GEOMETRY

Figure 3.3.1 - STRIP MAPPING MODE

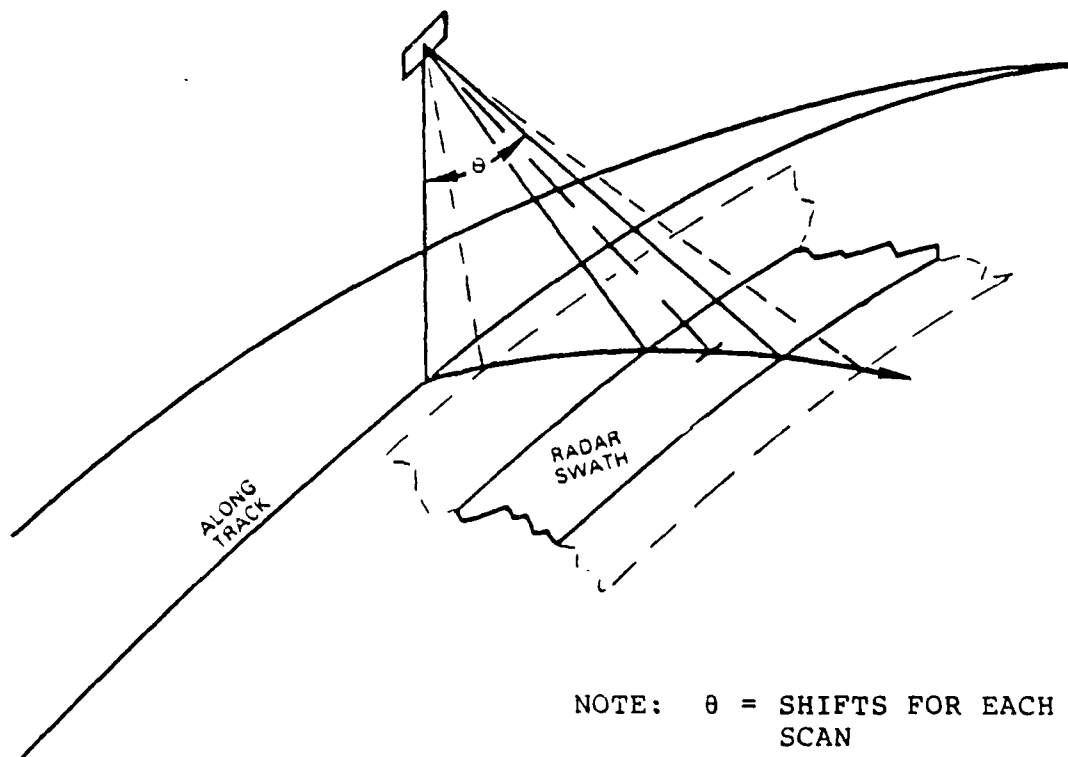


Figure 3.3.2 - SCANSAR MODE

The viewing geometry was adjusted to minimize the antenna dimension required in the range direction. The other radar design values used were:

1. Use of a steep look down geometry, $\phi_i = 10^\circ$. This reduces A_{MIN} and consequently the antenna dimension in range which increases swath width.
2. The dwell time used to avoid meteorological decorrelation at 35 GHz was .0017 seconds. This is an approximate value over the application range.
3. Clear air loss was assumed to be 2dB (.5dB/km over a 4 km distance).
4. Peak power limits = 4 kilowatts maximum, average power = 220 watts (Table 3.2.2).
5. $T_s = 700^\circ$ (includes receiver noise figure - see Table 3.2.2).
6. RF losses 5.2dB
7. Spatial resolution vertical ≤ 1 km
8. Spatial resolution horizontal ≤ 6 km (maximum permissible)
9. The reflectivity as a function of cloud type that was used is shown in Table 3.3.1.

The TSC space-based radar analyzer SAR mode was used to produce calculations at orbital altitudes for a 300 km circular orbit and a 833 km circular orbit (DMSP orbit).

CALCULATION RESULTS:

For a low orbit:

Length of the synthetic aperture L_{SA}
 L_{SA} (300 km altitude, 10° incidence angle)
 $L_{SA} = 594m$, $v_{gd} = 7382m/sec$
 $T_{DWELL} = T_D = .08$ sec (fully focused)

For a higher orbit such as DMSP:

L_{SA} (833 km altitude, 10° incidence)
 $L_{SA} = 1651m$, $v_{gd} = 6578m/sec$
 $T_D = .25$ sec (fully focused)

Table 3.3.2 provides a range of values for the orbits and incidence geometries under consideration.

The maximum PRF to avoid ambiguities over the 18 km meteorological altitude range is $c/(2 \times 18 \text{ km})$ or 8333 pulses per second where c is the speed of light.

The along-track resolution (δ_{AT}) can be expressed as:

**TABLE 3.3.1 REFLECTIVITY AS A FUNCTION
OF CLOUD TYPE**

<u>CONDITION</u>	<u>REFLECTIVITY</u>
LIGHT RAIN (1mm/hr)	-48dB m ⁻¹ = 1.58 x 10 ⁻⁵ m ⁻¹
CIRRUS CLOUDS	-65dB m ⁻¹ = 3.16 x 10 ⁻⁷ m ⁻¹
STRATUS CLOUDS	-85dB m ⁻¹ = 3 x 10 ⁻⁹ m ⁻¹

**TABLE 3.3.2
NUMBER OF SAR LOOKS TO COMPLY
WITH THE METEOROLOGICAL DECORRELATION TIME LIMIT
AT 35 GHz**

ORBITAL ALTITUDE	300 km		833 km	
RADAR INCIDENCE	$\phi_i = 10^\circ$	$= 45^\circ$	$\phi_i = 10^\circ$	$= 10^\circ$
<hr style="border-top: 1px dashed black;"/>				
T_D^* IN SECONDS	.08	.11	.25	.33
T_C^{**} IN SECONDS	.0017	<hr style="border-top: 1px dashed black;"/>		
# OF LOOKS	47	65	147	194

* T_D IS THE SAR FULLY FOCUSED DWELL TIME

** T_C IS THE METEOROLOGICAL DECORRELATION TIME LIMIT

$$\begin{aligned}\delta_{AT} &= (D_{AT}/2)m \times \# \text{ of looks} \\ &= 2.2m \times \# \text{ of looks}\end{aligned}$$

D_{AT} is the along-track antenna dimension of 4.4m.

$$\text{The number of looks} = \frac{\text{SAR fully focused } T_D}{\text{meteorological decorrelation dwell time limit } T_c}$$

SPATIAL RESOLUTION RESULTS:

$$\begin{aligned}\# \text{ of looks (300 km altitude)} &= .08/.0017 = 48 \\ \# \text{ cf looks (833 km altitude)} &= 25/.0017 = 148 \\ \delta_{AT} \text{ (300 km altitude)} &= 106m \\ \delta_{AT} \text{ (833 km altitude)} &= 326m \\ \delta_{VERT} &= \delta_{SR}/\cos\phi_i \\ \delta_{HOR} &= \delta_{SR}/\sin\phi_i \\ \delta_{SR} &= \text{slant range resolution}\end{aligned}$$

Let $\delta_{SR} = 900m$, $\phi_i = 10$ degrees

Then $\delta_v = 914m$ and $\delta_H = 5183m$

The performance of the strip mapping METSAR designed with these radar and mission parameters is summarized in Table 3.3.3. Note the severely limited swath widths associated with stratus cloud detection.

3.3.3 SCANSAR MODE

To improve the swath width a SCANSAR mode was evaluated. This approach is being considered for several applications (JPL - NASA EOS design, Canada - Radarsat design) and is shown in Figure 3.3.2. SCANSAR results in an increased swath width since only a few pulses are coherently integrated in the strip mapping mode to comply with the .0017 sec decorrelation time estimate. The resulting along-track resolution for SAR is more than adequate, and the articulating beam SCANSAR provides a larger swath.

SCANSAR can use a much wider antenna in the range or cross-track direction (still less than the 4.4m limit) to produce a narrow footprint at $\phi_i = 45^\circ$ such that:

$$(\lambda/D_R) R/\cos\phi_i = 6 \text{ km}$$

For an orbital altitude of 300 km

$$D_R = \frac{.008571 \times 515132 \times 1.41}{6000} = .836 \text{ m}$$

For an orbital altitude of 833 km

$$D_R = \frac{.008571 \times 1116694 \times 1.41}{6000} = 2.25 \text{ m}$$

This will assure that $\delta_H = 6 \text{ km}$

$$\delta_v = \delta_{SR} \times 1.41$$

$\delta_{SR} = 700\text{m}$ will assure adequate vertical resolution

The idea is to integrate in one position for T_C and then move the beam (scan) to the next 6 km segment continuing this process over as wide a swath area as possible on either side of the satellite. Using the same parameters employed in Section 3.3.2 (i.e., loss budgets, 4.4m along-track antenna length, 700° antenna noise temperature) the SCANSAR has the added advantage of significantly more antenna gain, compliance with all of the spatial resolution requirements, and wider swath coverage.

The 300 km design will scan over a range from 47 km (10° incidence) to 335 km (50° incidence) from the nadir and will detect Stratus clouds. The 833 km design will scan over a range of 127 km (10° incidence) to 821 km (50° incidence) from the nadir and will handle Stratus clouds. However, this design is similar to the scanning pencil beam altimeter described in Section 3.2. A performance summary for SCANSAR is provided in Table 3.3.4.

3.3.4 ADAPTATION OF THE METEOROLOGICAL SCANNING ALTIMETER FOR A HIGH RESOLUTION, LIMITED SWATH SAR GROUND MAPPING MODE

Since the antenna is a dish, the range antenna dimension used in the model will be $4.4 \times .33 \times .79 = 1.14\text{m}$. A 300 km altitude circular orbit and a 833 km altitude circular orbit will be investigated. A SCANSAR mode is particularly applicable for this adaptation and this possibility is shown in Table 3.3.5.

The 300 km altitude version can SCANSAR 6 scan positions or a swath of approximately 30 km. The 833 km altitude version can SCANSAR 3 positions or a swath of approximately 21 km.

ASSUMPTIONS FOR THIS MODE ARE:

1. 35 GHz RADAR
2. 4.4m PARABOLIC DISH ANTENNA
3. 3 TO 1 BEAM SPOILING IN RANGE
4. 90° TO ALONG-TRACK STRIP MAPPING SAR
5. 50° INCIDENCE GEOMETRY
6. 4 kw PEAK AND 220W AVERAGE POWER LIMIT

TABLE 3.3.3 STRIP MAPPING SAR MODE

	ALT	SWATH (km)	POWER (KW)		S/N (dB)	PCR	ANTENNA WIDTH (m)
			PK	AVG			
LIGHT RAIN	300	153	3.4	.087	10	1	.02
	833	100	3.9	.099	10	1	.07
CIRRUS	300	23	3.8	.098	10	1	.12
CLOUDS	833	14	3.8	.097	10	1	.52
STRATUS	300	6	3.1	.205	5	3	.44
CLOUDS	833	3	2.0	.155	5	3	2.45

PCR - PULSE COMPRESSION RATIO

**TABLE 3.3.4 SCANSAR MODE
STRATUS CLOUD MAPPING
PCR =1, S/N = 10dB**

	SWATH (km)	POWER (KW)		ANTENNA WIDTH (m)	SCAN POSITIONS
		P _K	AVG		
300 km ORBIT	288	1.74	.035	.84	48
833 km ORBIT	694	2.70	.052	2.26	115

TABLE 3.3.5 HIGH RESOLUTION ALTIMETER - SCANSAR

	RESOLUTION (m)			POWER (KW)		PCR
	ALONG TRACK	RANGE	SWATH (km)	PK	AVG	
300 km ALTITUDE	2.2	13	30	3.8	.042	40
833 km ALTITUDE	2.2	13	21	3.9	.213	200

3.3.5 METSAR MODE CONCLUSIONS

The primary objective of this study and the special virtues of synthetic aperture radar (SAR) are in conflict. The meteorological application requires:

1. A short integration time to avoid target decorrelation at 35 GHz, which was the frequency deemed most promising in study analyses (see Section 3.2); this time was assumed to be .0017 seconds. In contrast, SAR systems rely on significant coherent processing gain by using relatively long integration periods.
2. Large area coverage rates to produce operationally useful information. SAR systems notably produce low coverage rates due to ambiguity limited beam dimensions coupled with the desire to integrate over longer periods at each beam position.

Some of the SAR shortcomings can be overcome by limiting the integration period and scanning the SAR beam (SCANSAR) but carrying this approach to an operationally useful conclusion results in a SCANNING PENCIL BEAM SOUNDER.

The SAR technique might be valuable as an adjunct to the Scanning Pencil Beam Sounder. The SAR can provide higher resolution cloud images, 100 meters or less, and will sense STRATUS clouds. However, the swath width is small (i.e., 6 km at 300 km orbital altitude). The SAR can also provide high resolution land and ocean surface maps, 10 meters or less, with a swath of 30 km if it is allowed to integrate over the full synthetic aperture. This application is not a study objective, but could be considered as part of an experimental program utilizing scatterometer, radiometer and high resolution imaging radar capabilities associated with the scanning altimeter design.

Coupling this feature with the Scanning Pencil Beam Sounder is the first step toward providing a multifunction radar (ALLRAD) able to:

1. Detect and map cloud bottom profiles with wide area coverage.
2. Provide high resolution land, sea and ice maps with useful swaths of 50 kms or more.
3. Measure ocean surface roughness (scatterometry) to determine wind speed (5-50 KT, $\pm 10\%$) and direction (20°).
4. Measure surface wave height or sea state ($\pm .5m$ from 1-20m).

3.4 Surface Reflectivity

When observing the radar cells above the surface, the relatively weak meteorological echoes can be corrupted by surface echoes entering the radar receiver through the antenna sidelobes. The clutter that presents the greatest problems are, in order:

- 1) The first sidelobe in the vertical plane below the main beam,
- 2) Close in sidelobes in the vertical plane with pulse compression,
- 3) The high reflectivity Nadir echo, and
- 4) The integrated sidelobes from other areas.

With the high antenna gain, the far out sidelobe rejection is about 120 dB for the altimeter type antennas and somewhat less for other configurations. Thus 3) and 4) are not significant contributors. Table 3.4.1 summarizes the limited available experimental data. The most variation in areas of high incidence angle depends on the nature of the snow (or ice).

Table 3.4.1 Reflectivity, σ_0 , Vs Incidence Angle From Nadir

Frequency Band		45°	30°	20°	15°	
Ku	Land	-10 dB	-7	-6	-5	+4
	Snow	-7	-6	-5	-4	+8
	Sea	-13	-8	-5	0	+10
Ka	Land	-13	-10	-9	-8	+2
	Refrozen Snow	-3	0	0	0	+2
	Wet or Dry Snow	-10	-8	-7	-6	-
	Sea	-13	-8	-5	0	+6
W or 140 GHz	Land	-13	-10	-9	-8	0
	Refrozen Snow	-4	-3	0	0	+2
	Wet or Dry Snow	-6	-5	-3	-	-
	Sea	-13	-8	-5	0	+6

There are a few indications that σ_0 does not change in any pattern between 35 and 94 GHz for terrain or water. It is guessed that this will hold for 140 GHz. Relatively smooth seas were used for 0°, relatively rough seas were modeled for 30° and 45°.

4.0 BASELINE SYSTEM EVOLUTION

The systems described in Section 3 are considered to be current state-of-the-art. With the possible exception of the peak sidelobe requirement, all of the system parameters are available in off the shelf components, or demonstrated systems. Subsequent discussions with suppliers (Sec. 5.1, 5.7) indicate that at Ka-band, the system noise temperature can be reduced to 500° K, and The Harris Corp. indicated that a 500λ - 700λ antenna can be built.

The proposed system in a low orbit does well against all models, including the Stratus clouds. The same system in a high orbit is likely to detect the weak Stratus cloud with slightly larger horizontal resolution cells. Two transmitters will be suggested for the baseline to obtain more energy and better reliability.

4.1 CONICAL SCANNING STRATEGY

A conical scan has been determined to be preferable to a nodding scan. The nodding scan mechanism is suspect of being more vulnerable to mechanical failure at the scan rates needed to support the ALLRAD swath and sample spacing requirements. Furthermore, the scan through nadir approach imposes variability on the observables since the radar IFOV size changes with nadir angle as does the surface reflection coefficient. These variabilities would complicate surface reference calibration and geophysical parameter retrieval algorithms considerably.

The conical scan pattern in the atmosphere is illustrated in Figure 4.1.1. Note that the back edge of the scan fills in across most of the pattern. There are, however, a few critical diamond shaped areas, symmetric to the pattern center, where the distance between the coverage arcs is equal to the distance the satellite travels in one antenna revolution. In an approximate sense, the distance between scan arcs in the pattern center equals half the distance between scan arcs in a diamond shaped area. For a 6 km along track sample spacing in the pattern center (which corresponds to a 12 km spacing in the diamond areas), the antenna must rotate at 38.7 rpm for a 300 km orbit and at 37.5 rpm at the 800 km orbit. It was determined that these scan rates are too fast to allow the dwell time necessary to meet the detection and estimation goals of the ALLRAD radar. The high spin rates also call for a larger despun mechanism.

The solution chosen for reducing the antenna scan rate is to add a second elevation beam. The second elevation beam is oriented to create a 6 km distance between the centers of the IFOV's of the two elevation beams (in keeping with the preferred 6 km sampling density). The two-beam scan pattern is illustrated in Figure 4.1.2 for the 800 km orbit and a 17 rpm spin rate. The worst case distance between samples at the center of the first diamond area is 18 km. However, this sampling density is only present over approximately 5% of the entire scan pattern. The distance between samples is 6 km over the satellite subtrack and decreases significantly towards the outer edges of the swath. Note that both elevation beams are pulsed continuously giving continuous coverage in the direction of rotation of the antenna.

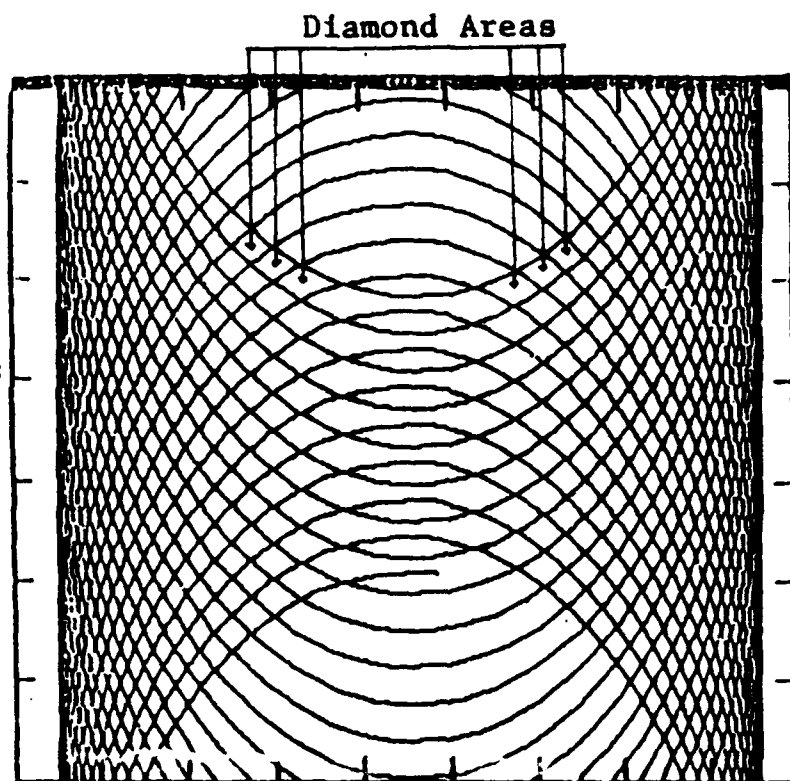


Figure 4.1.1 Conical Scan Pattern

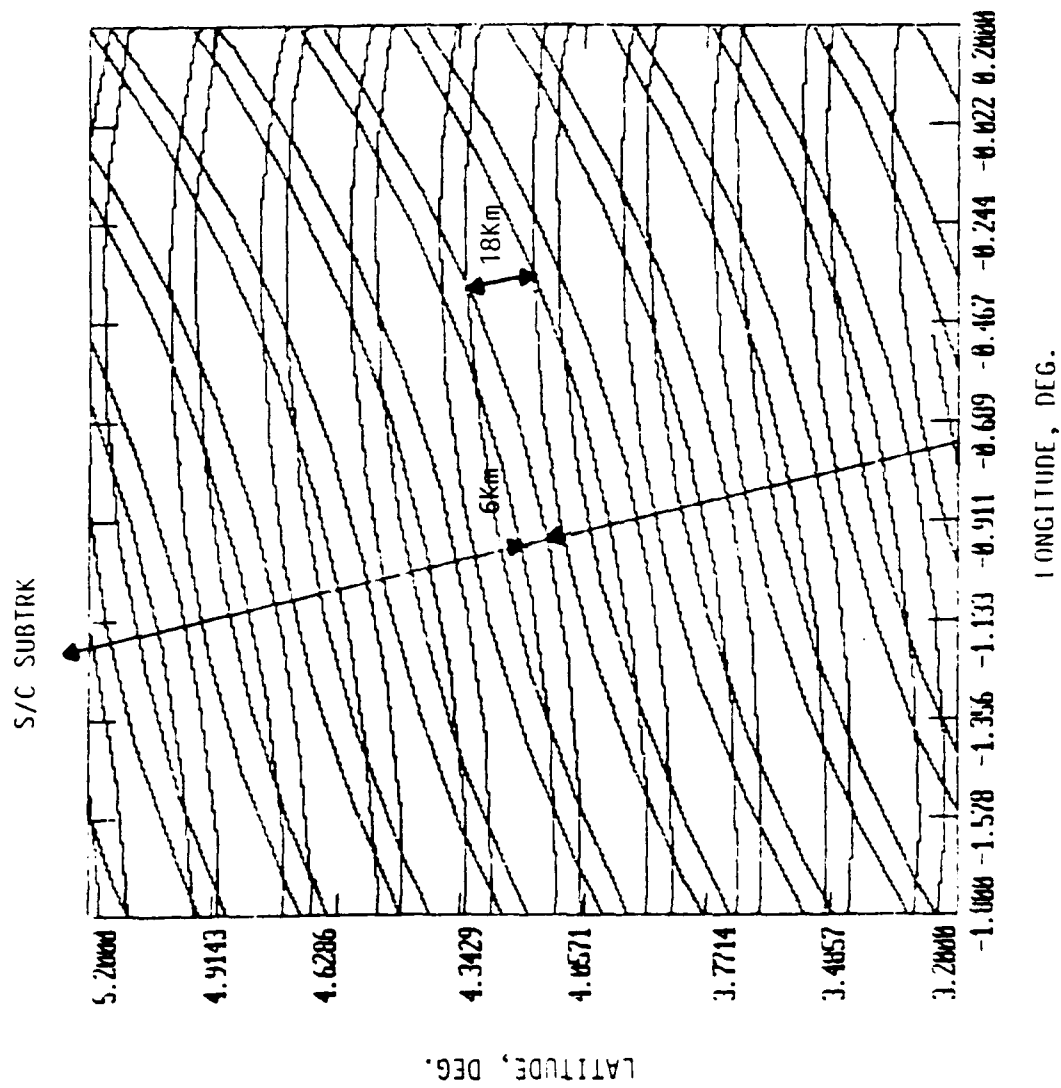


Figure 4.1.1.2 ALLRAD Scan Pattern, 2 Beams, 17 RPM

4.2 WAVEFORM SELECTION AND NUMBER OF SAMPLES

This section discusses the selection of the best waveform for the radar. It shows that a simple fixed pulse rate waveform is adequate, but that not all echoes are independent.

The ALLRAD waveform is designed to maximize the detection capabilities of the radar and to optimize the geophysical parameter estimation capabilities of the instrument. The first objective motivates a duty-limited waveform for maximal transmitted energy. The second objective requires a sufficient number of independent samples of the phenomena being estimated. The constraints are resolution, atmospheric range ambiguities, and system complexity.

4.2.1 Detection Considerations

In light of the above, the recommended ALLRAD waveform is a single PRF, continuous pulse train, without pulse compression. The ALLRAD radar is designed to detect very light stratus clouds. Under these conditions, the matched filter range sidelobes must be less than -60 dB to avoid earth surface interference. Pulse compressed, linear and non-linear FM waveforms and processors do not give this kind of performance, especially with low pulse compression ratios.

The two parameters to be determined are the pulselength and PRF. The maximum pulselength is limited by the vertical radar resolution goal of 1 km. For a 300 km orbit and 400 km swath, the maximum pulselength is 4 μ sec. For the 800 km orbit and 600 km swath, the pulselength is 3.2 μ sec which degrades the vertical resolution slightly.

The choice of PRF is more difficult and involves a few design tradeoffs. The first consideration is power. The transmitter tubes currently under investigation for the ALLRAD radar have peak powers which range between 2 and 8 KW. A realistic constraint on average power is 200 watts. The duty limited PRF for a 2 KW system is approximately 25 KHz for the 300 Km orbit and 30 KHz for the 800 Km orbit. For an 8 KW system, the duty limited PRF is approximately 5.5 KHz at 300 Km and 8 KHz at 800 Km. Figure 4.2.1 gives the duty-limited PRF as a function of peak power at both orbital altitudes. A second consideration when choosing the PRF is the atmospheric range ambiguity. The phenomena of interest to the ALLRAD radar are within 18 Km of the earth surface. At the 300 Km altitude and the 800 Km altitude, the ambiguity-limited PRF's are 7.1 KHz and 7.8 KHz. According to Figure 4.3.1, the full duty, unambiguous waveform necessitates 7 KW of peak power for the 300 Km orbit and 8 KW of peak power for the 800 Km orbit. Table 4.3.1 summarizes the waveform parameter limits for the ALLRAD radar.

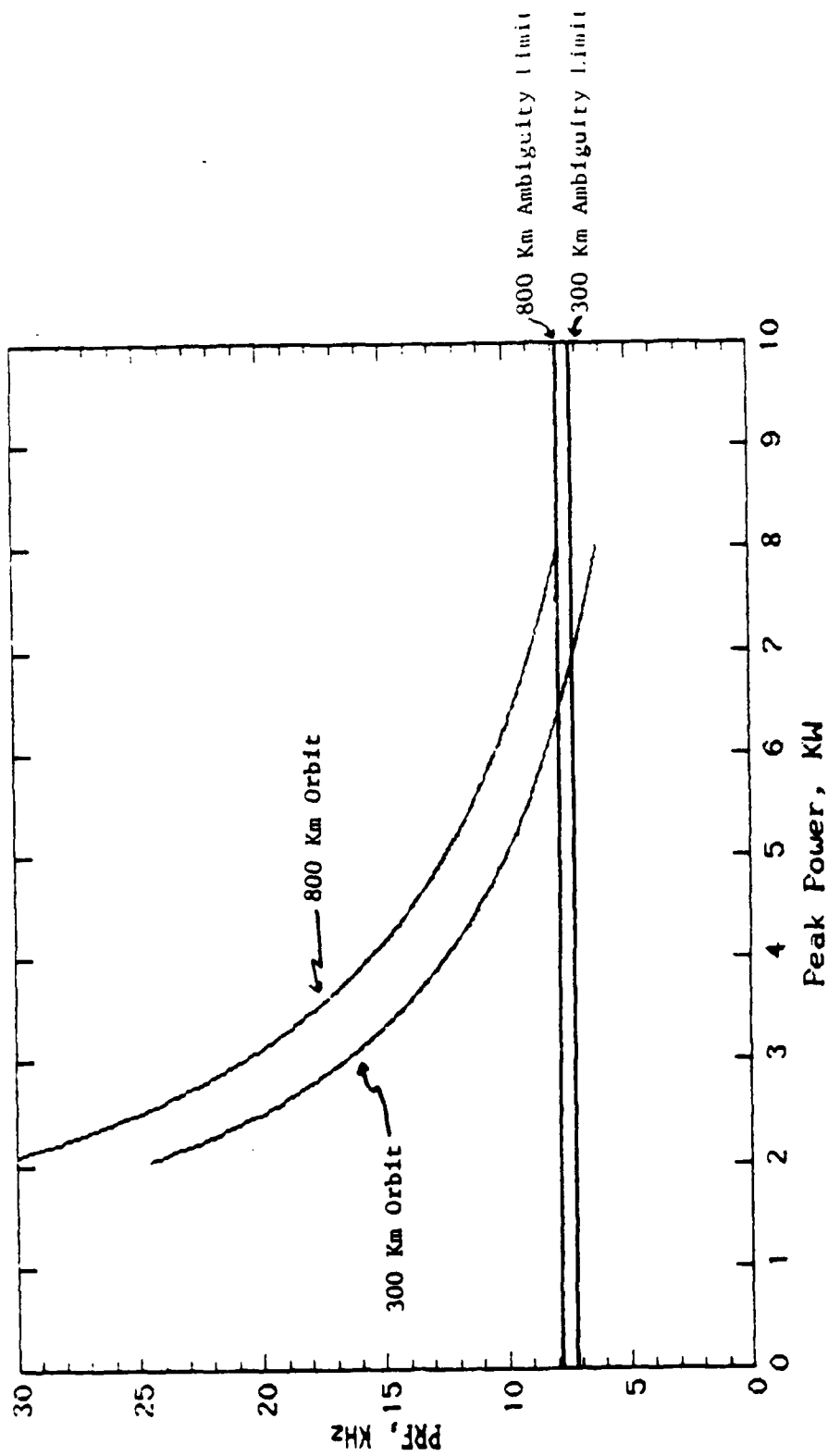


Figure 4.2.1

Average Power = 200 W Altitude = 300, 800 Km
 Pulse Length = 4., 3.2 sec

Table 4.2.1. ALLRAD Waveform Parameters Based on PRF, Ambiguity and Average Power Limits.

Orbit Altitude (Km)	Peak Power (KW) Required?	Ambiguity - Limited PRF (KHz)	Baseline PRF (KHz)	Pulse Length (μ sec)	Average Power (watts)
300	7	7.1	7	4	196
800	8	7.8	7	3.2	179.2

Examination of return signal fluctuation is necessary to determine whether or not frequency agility can significantly contribute to the detection capabilities of the ALLRAD radar. There are three sources of temporal decorrelation for the distributed atmospheric target viewed from space. The first is the doppler spread due to turbulence, wind shear, and locally varying rainfall drop velocities. The power spectral density for these effects is assumed Gaussian, and the standard deviation is modeled by Dr. R. Crane (1 m/s for 1mm/hr rain, .2 m/s for stratus, etc.). Because the unnormalized Gaussian function is its own Fourier transform, the autocorrelation function associated with the atmospheric spectral density is Gaussian and easily computed. Table 4.2.2 summarizes the postulated atmospheric spectral density, its autocorrelation function, and the decorrelation time for various atmospheric conditions.

The second source of decorrelation is the effect due to antenna scanning. Assume a 17 rpm antenna spin rate (see Section) and a 7 KHz PRF. The antenna rotates .014 degrees during one inter-pulse period. In beam coordinates, this number is .006 degrees for the 300 Km orbit, and .004 degrees for the 800 Km orbit, which equals 1/18 and 1/27 of the two-way, 3 dB beamwidth respectively. There is not significant pulse-to-pulse decorrelation due to antenna scanning for the 17 rpm spin rate. For simplicity, a Gaussian beam shape is assumed to determine the autocorrelation function of the beam radiation pattern in terms of azimuth angle variation. Total decorrelation ($\rho \approx 0$) due to antenna scanning occurs in 2.85 milliseconds at 300 Km and 4.5 milliseconds at 800 Km. The beam dwell time is 2 milliseconds at 300 Km and 3 milliseconds at 800 Km. For both satellite orbits the antenna scanning effect does not sufficiently decorrelate the signal over the beam dwell time.

The third and dominant source of decorrelation is the effect of satellite translational motion. This effect yields a doppler spectrum which is a "power weighted distribution of the radial velocities of the scatterers that mostly lie within the resolution volume" Goldhirsh [2]. The power weight is a function of the reflectivity of the scatterers, the antenna radiation pattern, and the pulse width. Doviak and Zrnic' [13] derive an integral over surfaces of constant velocity within the pulse resolution volume which gives the doppler spectrum. A simplified approach is used for this study which is based upon a two dimensional integral over the

Table 4.2.2 Atmospheric Spectral Characteristics

The atmospheric spectral density can be written;

$$G(f) = \exp \left(- \frac{f^2}{2\sigma_f^2} \right)$$

$$\rho_1(\tau) = \exp \left(- 2\pi\sigma_f^2 \tau^2 \right),$$

$$\sigma_f = \frac{2\sigma_v}{\lambda}$$

OBSERVABLE	ASSUMED DOPPLER SPREAD (σ_v , m/sec)	σ_f (Hz)	DECORRELATION TIME $\rho \approx 0$ (seconds)
1 mm/hr Rain	1	235	4.2 E-3
16 mm/hr Rain	2	470	2.1 E-3
Stratus	.2	47	2.1 E-2
Cirrus	.2	47	2.1 E-2

combinations of azimuth and elevation angle which form isodops on the elliptical pulse area formed by the intersection of the atmosphere and the azimuth and elevation beams. Atmospheric reflectivity is assumed constant on this area and integral limits are allowed to go to the 6 dB one-way beam limit. The integral can be expressed as,

$$P_r dv = \int f^4(\theta - \theta_0, \phi - \phi_0) d\theta d\phi dv$$

where,

P_r = expected power

$f(\theta, \phi)$ = antenna radiation pattern.

A numerical integration was performed over 10,000 points to yield the IFOV doppler spectrum as a function of scan angle from the platform velocity vector. Figure 4.2.2 illustrates the doppler spectrum for a 300 Km orbit at scan angles of 0, 30, 60, and 90 degrees from the satellite track. Figure 4.2.3 illustrates the doppler spectrum for a 800 Km orbit for the same assortment of scan angles. The spectrum at each scan angle has been shifted down to a 20 m/s zero point so that the spectral widths can be compared. Note for both cases that the spectrum is most narrow in the along track direction and widest in the cross track direction. Figures 4.3.4 and 4.3.5 give the ALLRAD IFOV first and second spectral moments for the 300 and 800 Km orbits. For a 300 Km orbit, the variance of the power spectrum does not exhibit as much sensitivity to scan angle as for the 800 Km orbit.

The information provided above can be used to determine whether a frequency agile waveform is worth the attendant increase in system complexity. First, it is appropriate to define fluctuation loss as "the increase in signal-to-noise ratio required to achieve the same detection probability, P_d , and false alarm probability, P_{fa} , for a fluctuating target as for a nonfluctuating target" Bucknam [3]. The fluctuation loss increases significantly (10 to 20 dB depending on the P_d) as the pulse-to-pulse correlation coefficient approaches unity. Frequency agility can be used to recover some of this loss. In order to determine the fluctuation loss for the ALLRAD system, it is necessary to form the composite autocorrelation function, $\rho_c(\tau)$, as follows;

$$\rho_c(\tau) = \rho_1(\tau) \rho_2(\tau) \rho_3(\tau)$$

where,

$\rho_1(\tau)$ = autocorrelation function due to postulated atmospheric motion spectrum,

$\rho_2(\tau)$ = autocorrelation function due to antenna scanning

$\rho_3(\tau)$ = autocorrelation function due to satellite motion.

The composite autocorrelation function can be used in the following equation to determine the equivalent number of independent pulses, N_e , for N pulses

Figure 4.2.2.2 ALLRAD IFOV SPECTRAL DENSITY

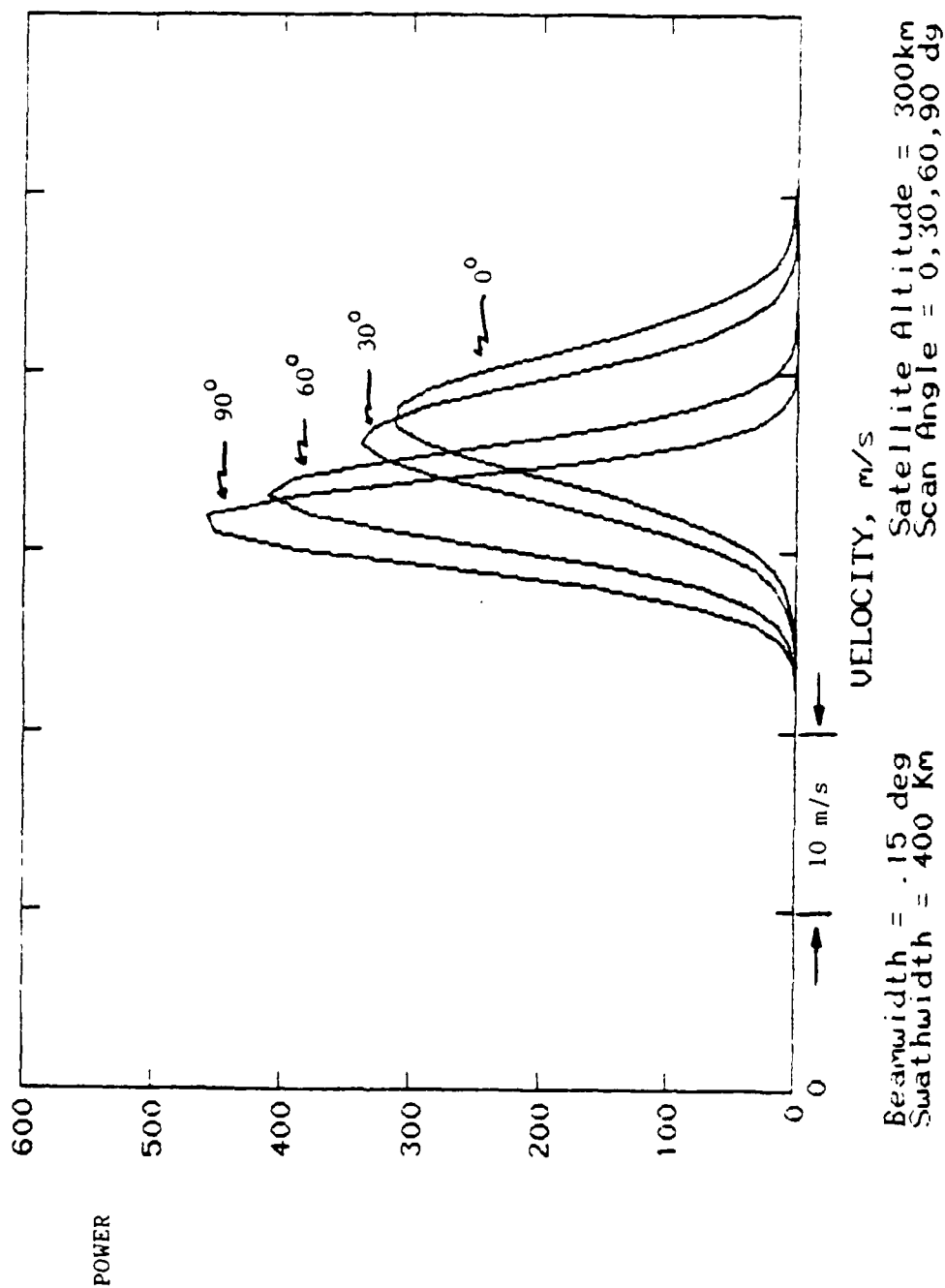


Figure 4.2.3 ALLRAD IFOV SPECTRAL DENSITY

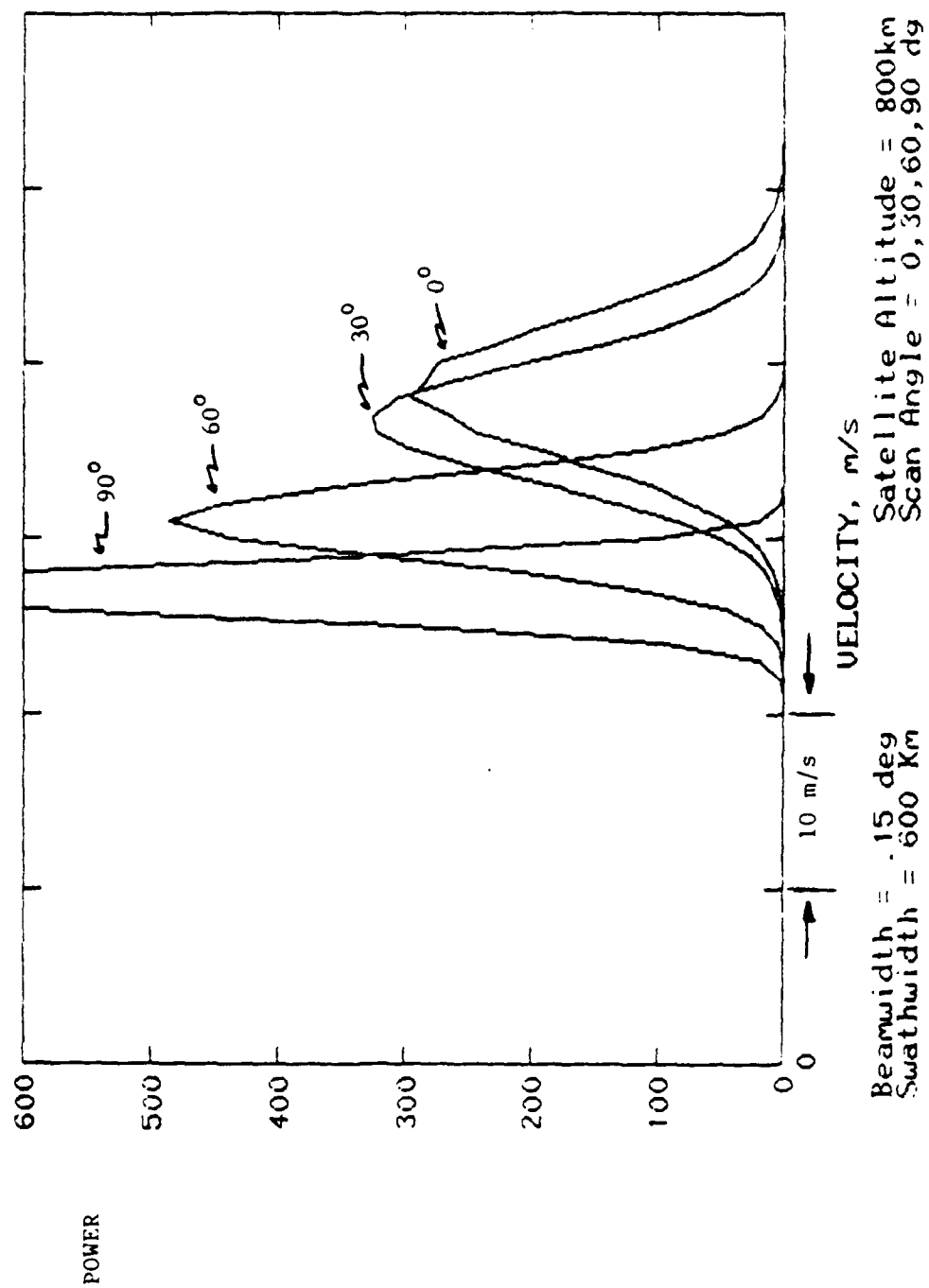


Figure 4.2.4 ALLRAD IFOV SPECTRAL MOMENTS

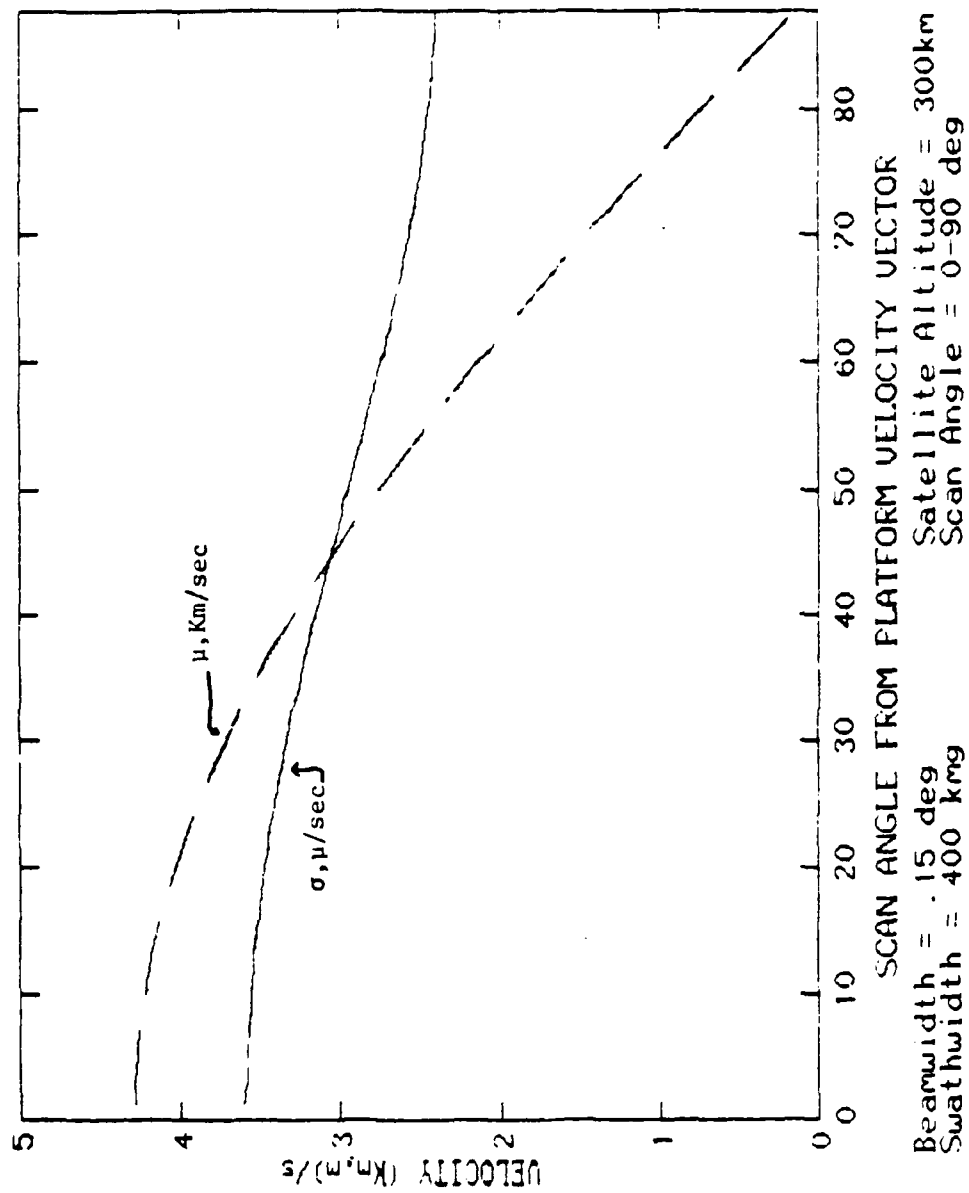
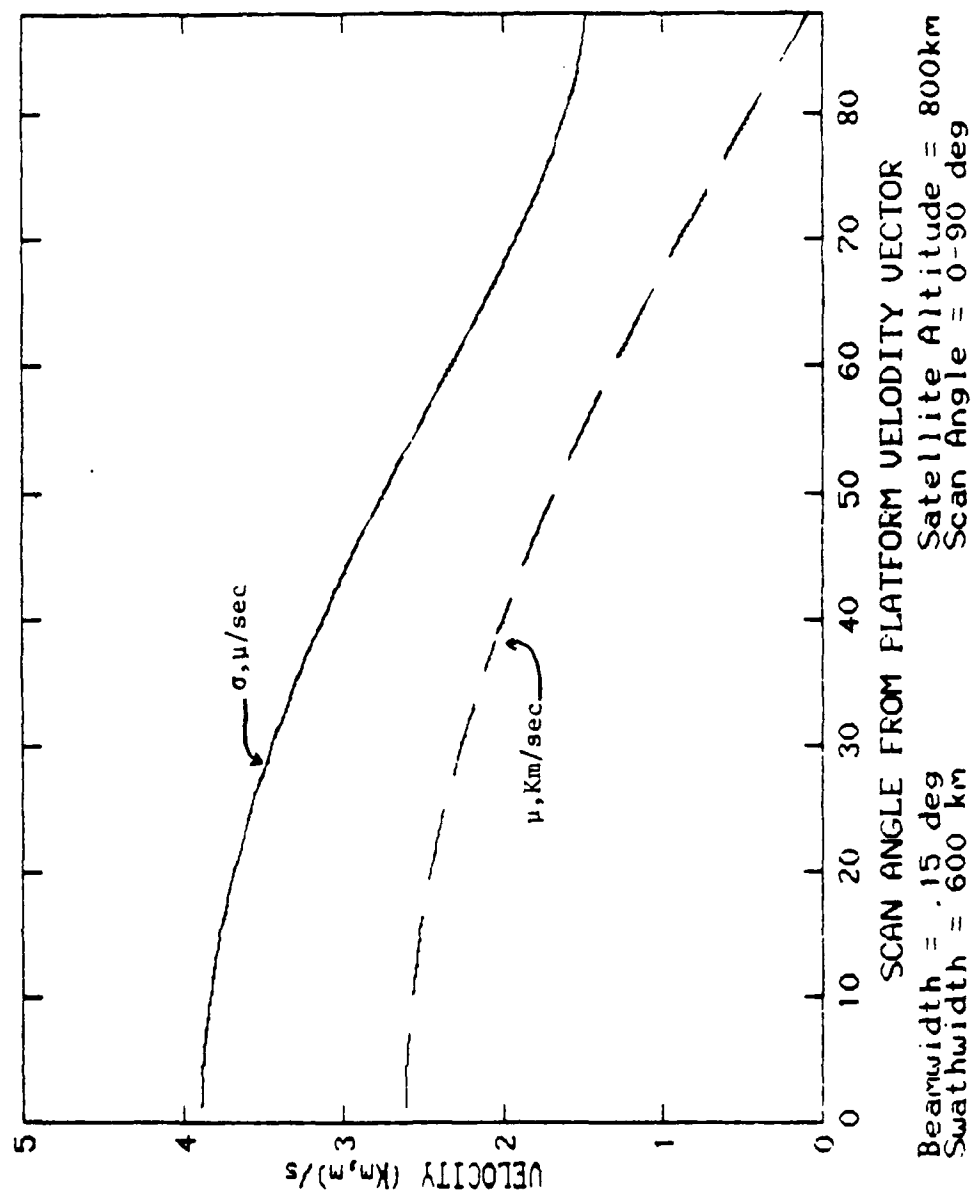


Figure 4.2.5 ALLRAD IFOV SPECTRAL MOMENTS



integrated;

$$N_e = \frac{N^2}{N-1 + 2 \sum_{m=1}^{N-1} (N-m) \rho_c^2(m)}$$

Figure 4.2.6 gives N_e for the 300 and 800 Km orbits as a function of scan angle. The fluctuation loss for a given number of independent pulses and a given P_d can be determined by using the curves developed by Kanter in [35]. Figure 4.2.7 is the chart from [35] for a .9 P_d (which is high for this application). The solid line in Figure 4.2.7 indicates that for 2 "effective" pulses integrated the fluctuation loss is slightly greater than 4 dB. For 3 independent pulses integrated, the fluctuation loss is slightly less than 3 dB. According to Figures 4.2.6 and 4.2.7, the worst case fluctuation losses (corresponding to the off-track scan angles) at the 300 and 800 Km orbits are 3.1 dB and 3.5 dB respectively. Considering that the best case fluctuation loss is about 1 dB ($\rho \approx 0$), the gains to be made by using frequency agility are 2.1 and 2.5 dB. Note, however, that more than 2 frequencies are needed to achieve these gains, and that in the along-track direction the frequency agility gain is less than 1 dB. If the P_d is reduced to .7, then the fluctuation loss is insignificant and use of frequency agility does not enhance radar sensitivity. In summary, if a high P_d (>.90) were needed for the ALLRAD radar, then frequency agility can yield approximately 2 dB gain in sensitivity at the off-track scan angles.

4.2.2 Estimation Considerations

The ALLRAD waveform impacts the geophysical parameter estimation capabilities of the instrument via the number of independent samples available to smooth the statistical uncertainties associated with the phenomena being measured (rain signal fluctuation, attenuation fluctuation). There are several algorithms which can be used for parameter estimation for the ALLRAD instrument. One algorithm may be best suited for heavy rain, another algorithm may be best suited for light rain, and some of the algorithms may incorporate radiometric measurements and scatterometer type of measurements. In short, it is difficult to determine whether the 3 to 6 independent samples per resolution cell provided by the current waveform is sufficient for the estimation problem without considerable investigation into the algorithms which may be used. This subject is discussed in section 4.4. If more than 3 to 6 independent samples are needed for sufficient estimation accuracy, then frequency agility is one possible solution. Another solution to be considered is expansion of the measurement cell resolution to 3 or possibly more radar resolution cells when measurement conditions are difficult. It should be noted that the pulse width computation made to satisfy the 1 km vertical resolution goal does not include the pulse envelope and the antenna pattern responses. The top and bottom edges of the 1 km vertical cell are really at the 6 dB down point when these responses are taken into consideration. Therefore, additional samples will be available in the vertical dimension of the measurement cell.

Figure 4.2.6 ALLRAD EFFECTIVE PULSES INTEGRATED

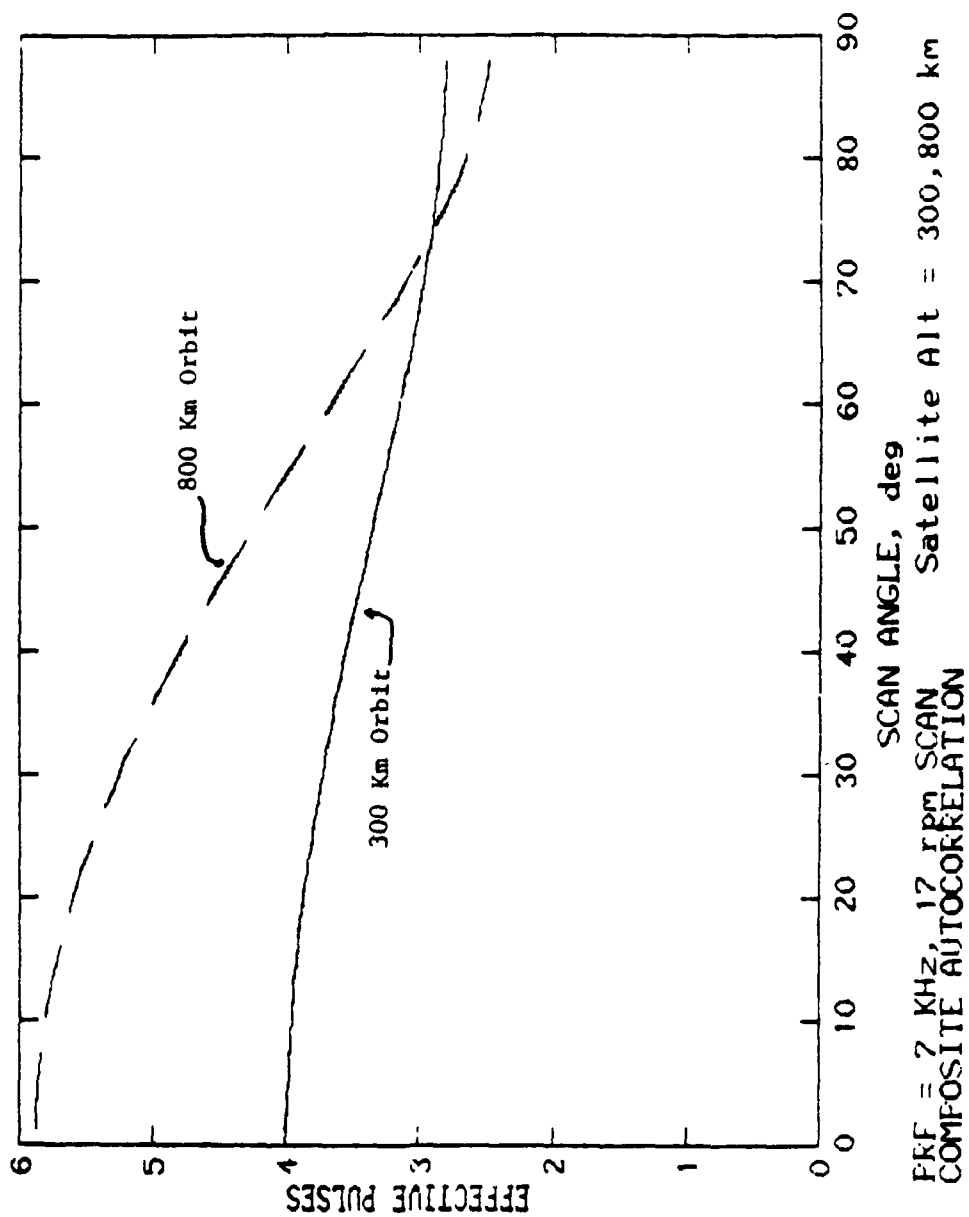
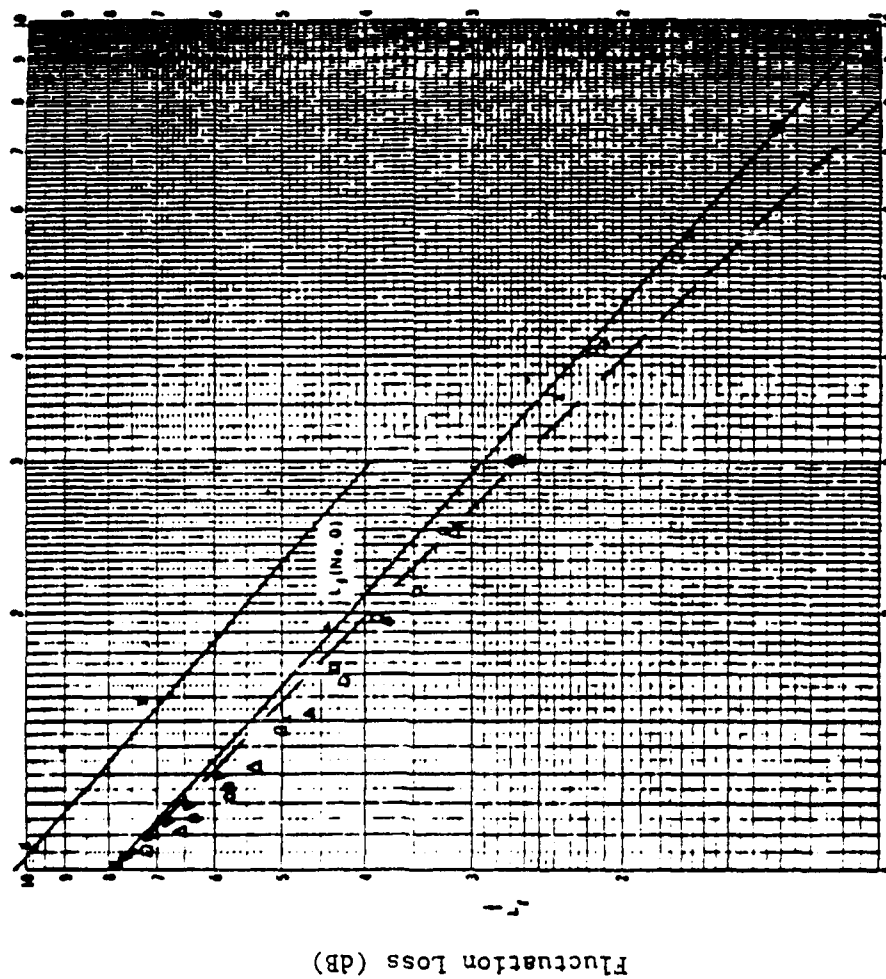


Figure 4.2.7 FLUCTUATION LOSS VERSUS NUMBER OF INDEPENDENT PULSES

$$\rho_D = 0.90$$



Independent Pulses

From Kanter [35]

4.3 Radar Parameter Selection and Detection Capabilities

This section presents the baseline radar parameters and the resultant radar detection capabilities. Table 4.3.1 lists the baseline radar parameters. The system has a short, uncompressed pulse and relies on a relatively large power-aperture product and a maximum unambiguous PRF for sensitivity. There are two transmitters, one for each elevation beam. Both transmitters operate synchronously with the same waveform and duty factor.

ALLRAD radar detection capabilities are presented in terms of signal excess above a somewhat arbitrarily chosen threshold setting. The threshold is set to yield a 50% probability of detection and a 10^{-6} probability of false alarm. It is likely that this false alarm probability can be relaxed for a real system. The 50% detection probability is convenient because signal fluctuation does not affect the ALLRAD radar detection capabilities for detection probabilities less than about 90% and Swerling case 2 Receiver Operator Characteristic (ROC) curves can be used to evaluate threshold settings.

The radar detection capabilities are evaluated for three spatial resolution cases; (1) 2 km or very high resolution, (2) 6 km or high resolution, and (3) 25 km or medium resolution. In each case the number of pulses which can be integrated over the resolution area is determined using the scan pattern and spatial sampling described in Section 4.1. Table 4.3.2 gives the number of pulses integrated and the corresponding threshold ($9 P_d, 10^{-6} P_{fa}$) for the three resolution cases and the 300 and 800 orbit altitudes. Tables 4.3.3 and 4.3.4 give signal excess for the 300 km orbit (400 km swath) and the 800 km orbit (600 km swath) respectively for the three resolution cases given above. Signal excess is evaluated at the bottom of the cloud to account for the full attenuation effect on the signal. At 300 km the radar detects stratus clouds at 2 km resolution with 4 dB signal excess. At 800 km the radar is 1 dB shy of detecting stratus at high resolution, but will detect stratus with 5 dB signal excess at 25 km resolution. Tables 4.3.3 and 4.3.4 indicate that heavy rain is easily detected at both orbital altitudes. It should be noted that the per pulse signal-to-noise ratio reaches zero for rain rates above 30 mm/hr. Non-coherent processing gain will allow detection of cloud bottoms for rates as high as 40 mm/hr.

Table 4.3.1 HIGH ORBIT RADAR/RADIOMETER

Frequency (Radar)	35.6 \pm .30	GHz
Frequency (Radiometer)	36.6 - 37.6	GHz
Altitude of Satellite	800	km polar
Antenna Diameter	4.1	Meters
Beamwidths (one way)	.15 - .16	Degrees
Horizontal Resolution	2	km
First Sidelobes (35dB design)	31	dB
Gain (G_T, G_R) (40° efficiency)	59.7	dB
Number of Transmitters/Recs.	2	
Transmit positions	2	Per Transmitter
Peak Power (per transmitter)	6.2	kw
Average Power (per transmitter)	150	watts
Pulse Repetition Frequency (Nominal)	7	kHz
Pulse Duration	3-4	Microseconds
Vertical Resolution	<1	km
Transmitter Loss (to feeds)	2.50	dB
Pattern Losses	1.0	dB
L_R , Receiver loss (included in T_S)		
T_S , System Noise Temp. ($L_R = 2.0$ dB)	500	°K
Filter and Detector losses	1.0	dB
Distribution and/or CFAR loss	1.0	dB
Swath Diameter	400,600	km
Nadir Angles	13.6, 20	Degrees
Rotation Rate (Approx.)	17	RPM
Pointing Accuracy (-1KM)	.11	Degrees

Table 4.3.2 Threshold Necessary for $.50 P_d$ and $10^{-6} P_{fa}$

	Number of Pulses		Threshold (dB)	
	300 km	800 km	300 km	800 km
2 km Resolution	40.4	30.4	0	.75
6 km Resolution	121.2	91.2	-5.2	-2.3
25 km Resolution	2020	1520	-9.6	-8.9

Table 4.3.3 ALLRAD Signal Excess (dB), 300 km Orbit, 400 km Swath

	Very High Resolution 2 km	High Resolution 6 km	Medium Resolution 25 km
Heavy Rain (4 km thick)	15.7	20.9	25.3
Light Rain	35.3	40.5	44.9
Cirrus	25.0	30.2	34.6
Stratus	4.1	9.3	13.7

Table 4.3.4 ALLRAD Signal Excess (dB), 800 km Orbit, 600 Km Swath

	Very High Resolution 2 km	High Resolution 6 km	Medium Resolution 25 km
Heavy Rain (4 km thick)	12.1	15.2	21.8
Light Rain	27.7	30.8	37.4
Cirrus	16.7	19.8	26.4
Stratus	-4.15	-1.1	5.5

4.4 ALGORITHMS FOR SPATIAL EXTENT, RAIN RATE AND LIQUID WATER CONTENT RETRIEVAL, AND PARTICLE DISTRIBUTION

Algorithms are necessary to convert the radar received power measurements into useful geophysical quantities. The quantities which directly relate via algorithms to the radar received power levels are the following: "equivalent radar reflectivity factor" $Z_e(\text{mm}^6/\text{m}^3)$ for both cloud and rain expressed in dBZ, the "cloud liquid water content" $M(\text{g}/\text{m}^3)$, and the "equivalent rain rate intensity" $R_e(\text{mm}/\text{hr})$. The intermediate and most difficult step in the conversion process is to determine the relative contributions of cloud/rain backscatter (η) and path integrated attenuation (α) to the power level measured at the output of the radar envelope detector. At Ka-band, attenuation becomes a factor at rain rates greater than 1 mm/hr and penetration depths of 1 km and greater. The problem which is difficult to solve with algorithms alone is the estimation of two unknowns given a single measurement.

There are several methods available for obtaining a second independent measurement which makes the estimation problem tractable. For ground based radars, the use of dual polarization differential reflectivity techniques has been investigated with success by Goldhirsh, Bringi and Seliga, Ulbrich, and others. However, for the space-based geometry under consideration for ALLRAD, the use of dual polarization is not likely to yield sufficiently independent measurements. Dual frequency techniques have been investigated for space borne radars by Goldhirsh [1], and exhibit increased estimation accuracy. However, this is a somewhat expensive option and does not contribute to the primary mission of the radar; measurement of cloud tops and bottoms. It is suggested that radiometric measurements (19 and 37 GHz) of path integrated liquid water content be used to obtain "total attenuation" estimates over the ocean. Over land, a surface reference technique is suggested which uses earth surface radar backscatter measurements (like a SCATTEROMETER) to estimate "total attenuation". The "total attenuation" estimate will be an input into an algorithm which, constrained by cloud and rain vertical extent measurements, outputs a vertical attenuation profile which can be used in conjunction with other classical algorithms to estimate rain rate. These algorithms are discussed in greater detail in Section 4.5.

4.4.1 Spatial Extent

Spatial extent is determined using both the detection and estimation functions of the ALLRAD instrument. Radar detection in the atmosphere answers the question; is there cloud mass or rain present within a given radar resolution cell? Maps of areal extent of rain and/or clouds are obtained from the three-dimensional grid of detection decisions which correlate to given radar cell samples. The accuracy of such a map is determined by the detection probability and false alarm probability associated with the threshold used to make detection decisions. The map resolution is determined by the radar resolution, and the lateral and vertical distance between radar cells. The radar resolution for a 300 km orbit is approximately 1.5km x 1.5km x 1km. The anticipated lateral spacing is 6 km. The vertical spacing is overlapped as illustrated in figure 4.4.1. Interpolation techniques can be used to obtain cloud bottom altitude estimates which are accurate to a few hundred meters.

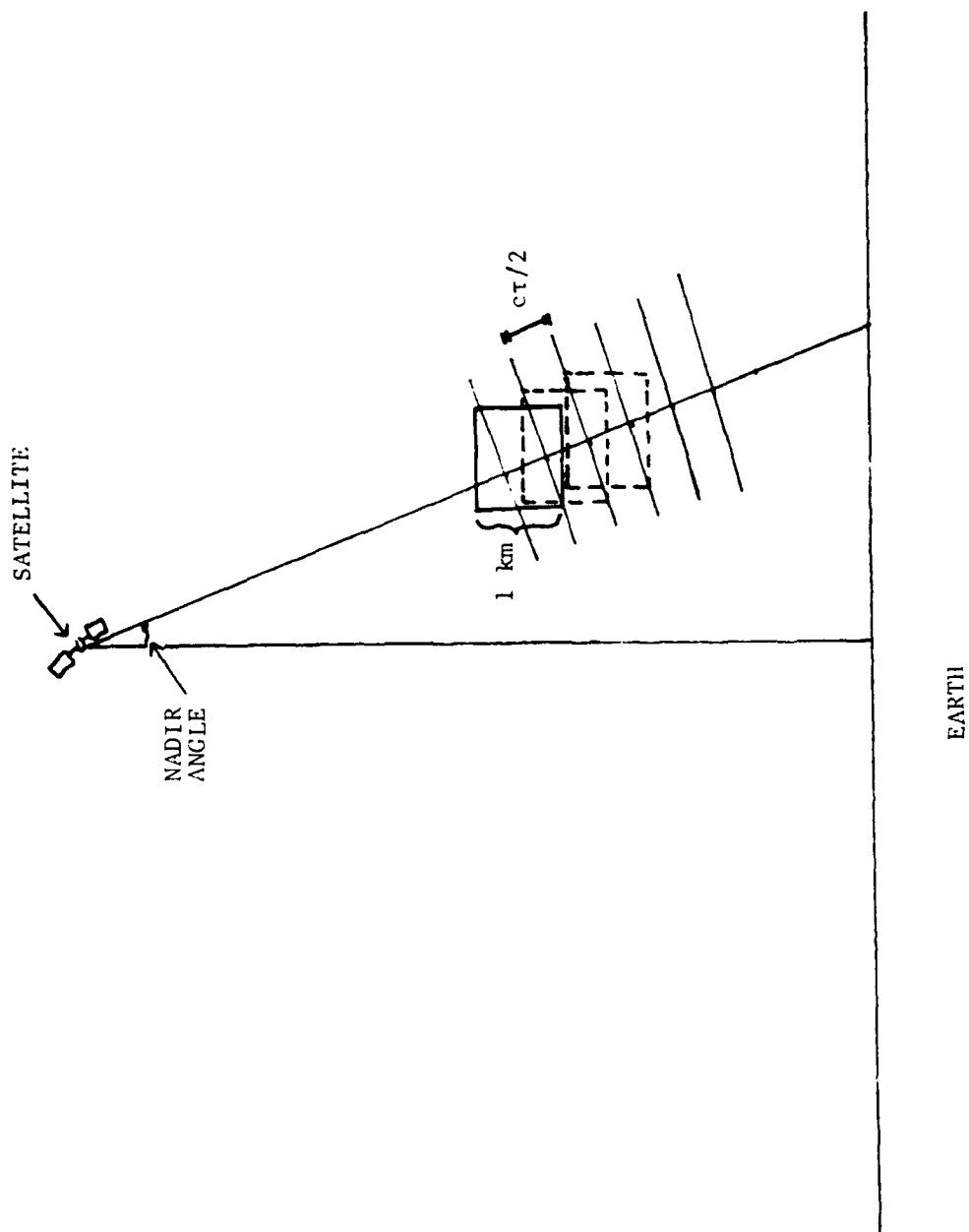


Figure 4.4.1.1. Overlapped Vertical Spacing of ALLRAD Radar Resolution Cells

A four dimensional map, a point on which is identified by position (longitude, latitude, and altitude), and either rain rate or liquid water content, can be generated using the detection map described above and the output of the estimation algorithms. Such a map gives the spatial extent of the various classes of the phenomena being observed (e.g., 10 mm/hr rain, stratus clouds, cirrus clouds, etc.) as a set of intensity contours.

4.4.2 Rain Rate and Atmospheric Liquid Water Content (LWC) Retrieval

This section discusses the "backscatter method" and the "attenuation coefficient method" as they apply to the ALLRAD radar. It also presents the ways in which the scatterometer and radiometer measurements may be used to enhance the rain rate and LWC retrieval accuracy of ALLRAD.

4.4.2.1 Backscatter Method

The backscatter method will be primarily used for the following conditions; (1) non-precipitating clouds to estimate LWC in g/m^3 , (2) rain rates less than 2 mm/hr over entire vertical extent of the atmosphere, (3) rain rates greater than 2 mm/hr for a few hundred meters into the top of the cloud. Figures 4.4.2 and 4.4.3 show the ALLRAD sensitivity (per pulse) in the .1 to 2 mm/hr interval and the 2 to 50 mm/hr interval respectively at various penetration depths into the rain (at the 300 km orbit). Visual inspection of the curves indicates that the attenuation effect (α) dominates over the increase in atmospheric reflectivity (η) as the rain rate increases beyond 5 mm/hr at Ka band. Another way to interpret these curves is that there is adequate signal-to-noise to define the rainfall rate in the top 3 km of the 4 km thickness to above 50 mm/hr.

The backscatter method described herein is developed in greater detail in various sources by Goldhirsh [36], [2], [5]. The method described below is for rain. An equivalent method can be used to estimate LWC. The backscatter method is based on the formulation of the mean radar echo power for rain backscatter which can be treated as the following:

$$P_v = C_o \eta \exp \left[-\gamma \int_0^h k_p dH \right]$$

where, C_o - radar constant
 k_p - attenuation due to precipitation
 H - along beam axis
 γ - .461

The path integrated effects of attenuation are ignored which gives rise to the definition of an effective reflectivity defined as,

$$\eta_e = \eta \exp \left[-\gamma \int_0^h k_p dH - AR_e^B \right]$$

The coefficients A and B are determined empirically for a given frequency and drop size distribution. Empirical relations of the form $\eta = AR^B$ abound

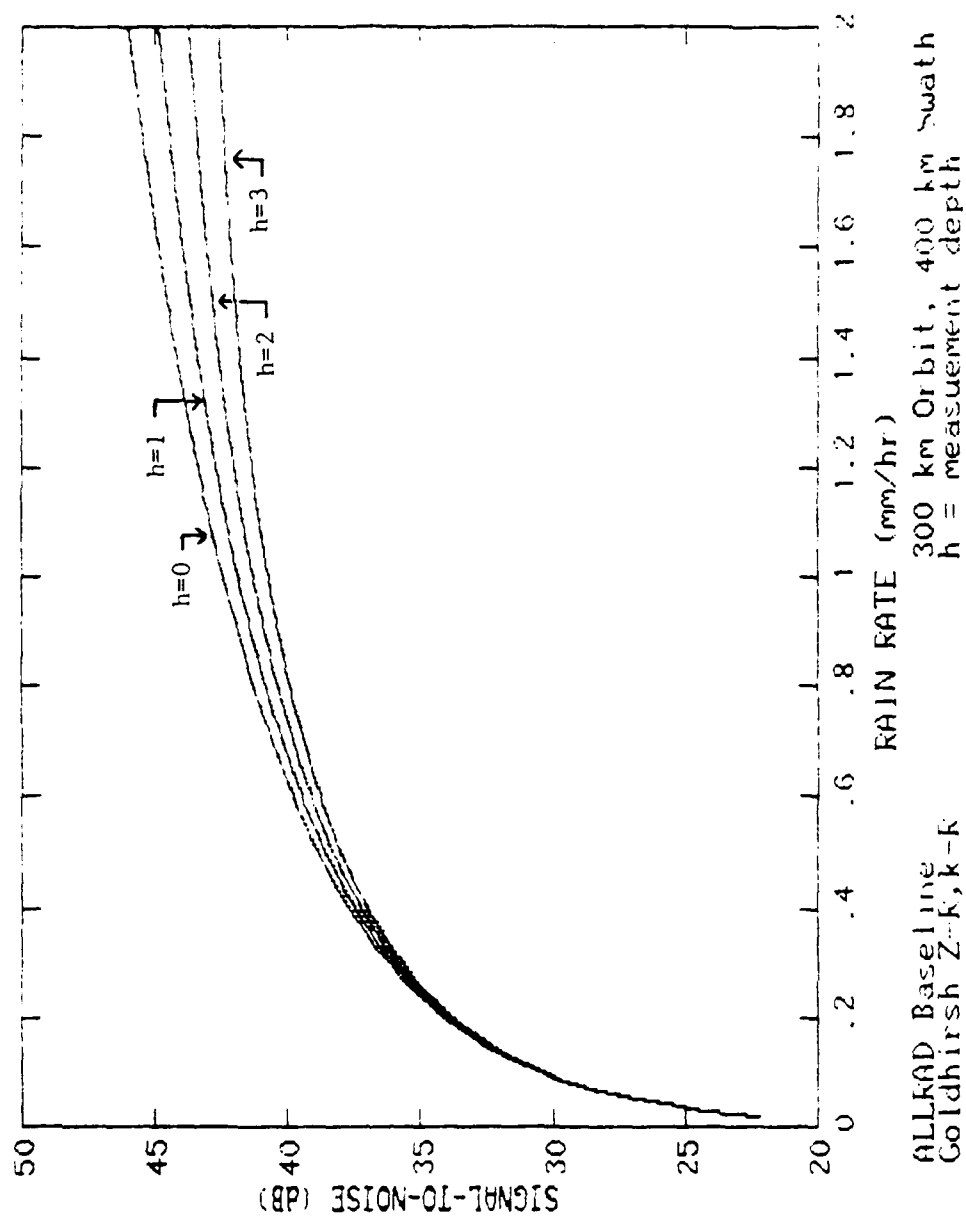


Figure 4.4.2. ALLRAD Per Pulse Sensitivity

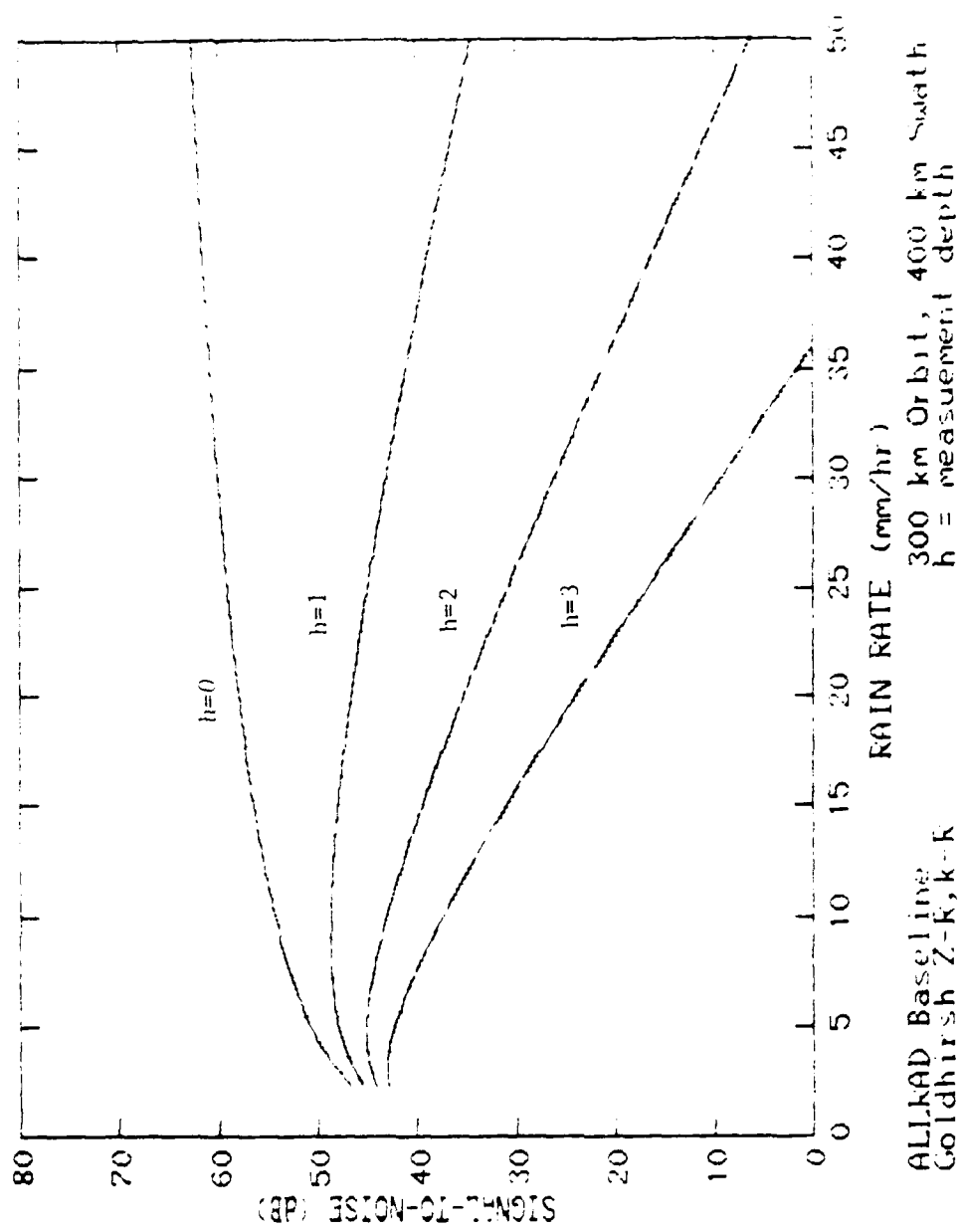


Figure 4.4.3. ALLRAD Per Pulse Sensitivity

in the meteorological literature for various combinations of frequency and drop size distribution. At 35 GHz, and a Marshall-Palmer Drop Size Distribution, Goldhirsh gives $A=2.29E-5$ and $B=1.192$ in [36]. Using substitution, the effective rain rate, R_e , can be determined from the radar echo power using the following equation:

$$R_e = \left[\frac{P_v}{C_o A} \right]^{1/B} \quad (\text{mm/hr}).$$

R_e approximates the true rain rate when attenuation effects are minimal.

Assuming that the rain or clouds fill the radar resolution cell, there are two major sources of error which contribute to distortions in rain rate profiles obtained using the backscatter method.* The first source of error is a bias which occurs because of the assumption that the signal is not attenuated. There is always some attenuation even in very light rains. Figures 4.4.4 and 4.4.5 illustrate effective rain rate (R_e) versus true rain rate at .1 to 2 mm/hr and 2 to 30 mm/hr respectively as measured by the ALLRAD instrument. In each case, a uniform vertical rain profile is assumed. For a 1 mm/hr rain, the effective rain rate is 10% down from the actual rain rate at a 1 km depth. For a 1 mm/hr rain and a 4 km depth, the effective rain rate is 48% down from the actual rain rate. For a 2 mm/hr rain rate and a 1 km depth, the effective rain rate is 19% down from the true rain rate. For a 2 mm/hr rain and a 4 km depth, the effective rain rate is 54% down from the true rain rate. For rain rates greater than 2 or 3 mm/hr and depths greater than a few tens of meters, the effective rain rate is significantly lesser than the actual rain rate. For example, the error is greater than 70% when the rain rate is greater than 10 mm/hr and the measurement depth is greater than 1 km.

The second source of error originates from the process of estimating the effective reflectivity, η_e . The actual return signal fluctuates according to the decorrelation effects outlined in the previous section, and the receiver noise is a stochastic process (a set of independent, identically distributed random variables). The standard

* The effects of uncertainty in the drop size distribution are not explored here.

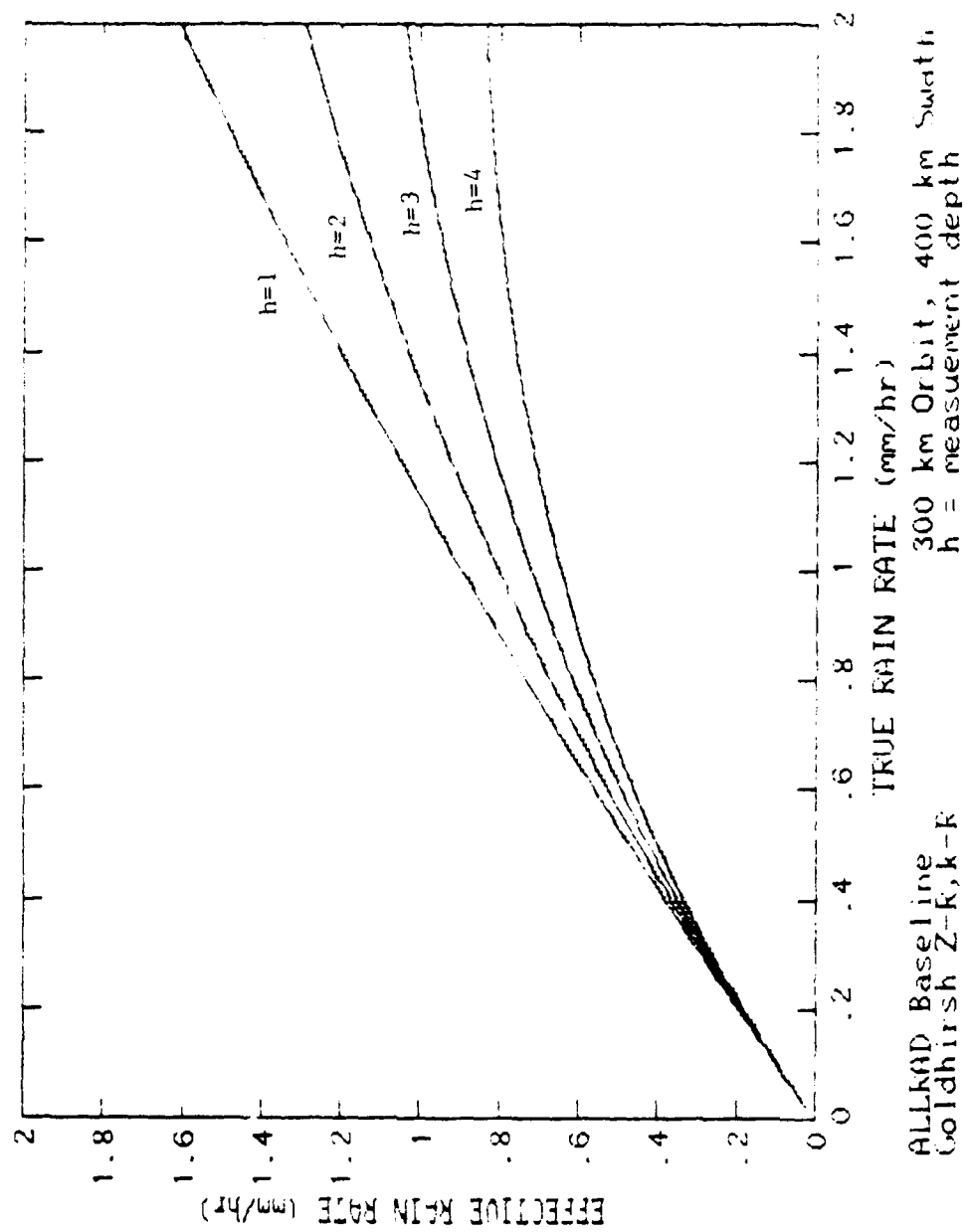


Figure 4.4.4. ALLRAD Effective vs. True Rain Rate

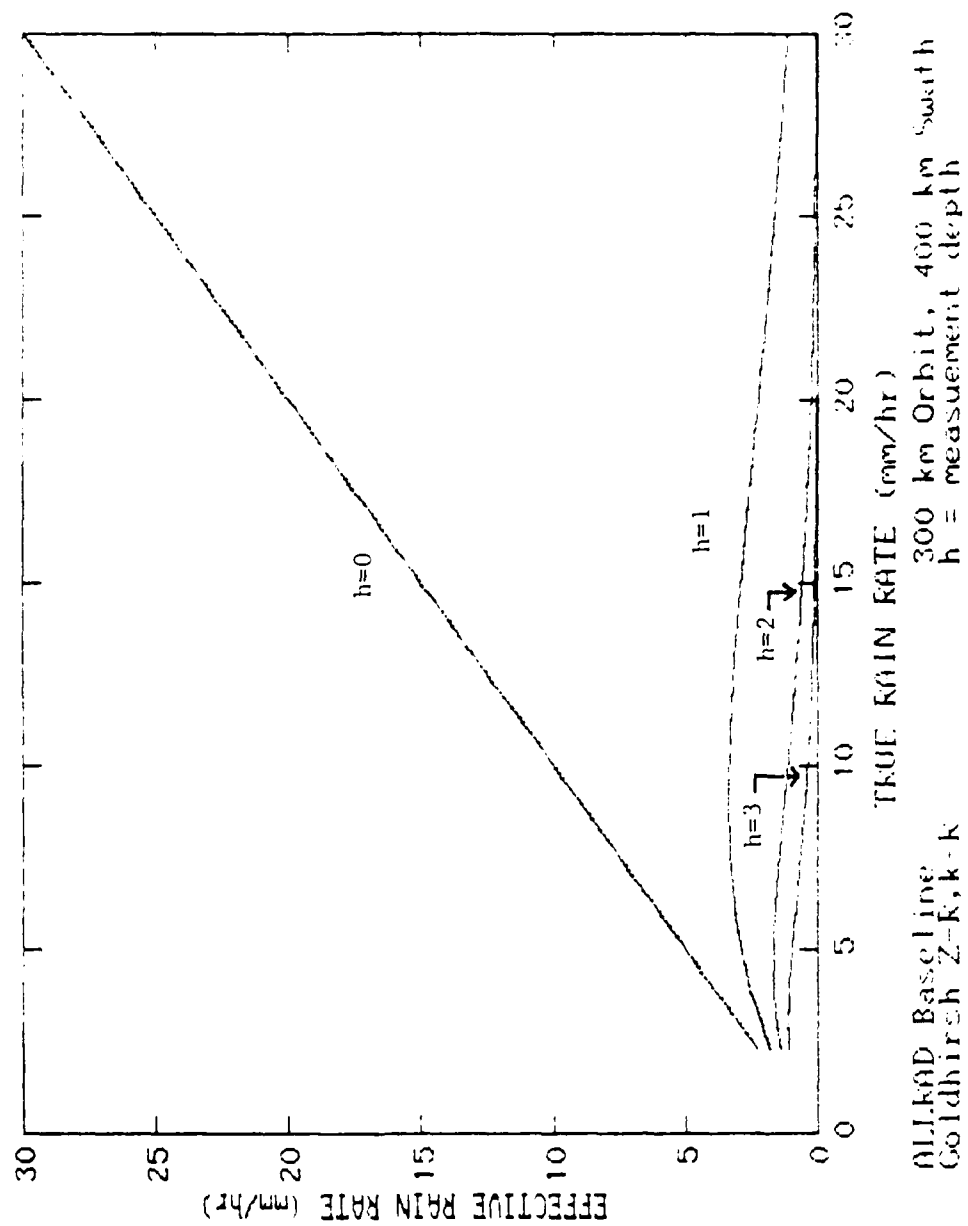


Figure 4.4.5. ALLRAD Effective vs. True Rain Rate

deviation associated with a given mean signal power, P_v , at a given instant is,

$$\sigma_s = P_v \left[\frac{1}{N} \left(1 + \frac{1}{\text{SNR}} \right)^2 + \frac{1}{N_n} \left(\frac{1}{\text{SNR}} \right)^2 \right]^{1/2}$$

where, N = number of signal samples
 SNR = Signal-to-Noise Ratio (per pulse)
 N_n = number of samples averaged to estimate the mean receiver noise.

Because the receiver noise is assumed to be a stationary process, very accurate estimates of receiver noise power are possible using long term averages. This allows the foregoing equation to reduce to the following:

$$\sigma_s = P_v \left(1 + \frac{1}{\text{SNR}} \right) \left(\frac{1}{N} \right)^{1/2}$$

The number of samples, N , averages to obtain the mean rain signal power is equal to the number of independent pulses obtained per 3 dB, 2 way beam pattern, unless spatial averaging is used (radar cell to radar cell). This number depends on orbit altitude and scan angle, and was computed in the previous section (ALLRAD Waveform) of this report to be between 3 and 6.

The error, σ_s , in estimating the equivalent reflectivity due to signal fluctuation, can be converted to a rain rate estimation error in mm/hr using,

$$\sigma_R = \frac{P_v}{C_o A} \left(1 + \frac{1}{\text{SNR}} \right) \left(\frac{1}{N} \right)^{1/2}$$

Figures 4.4.6 through 4.4.9 illustrate this error for rain rates between .1 and 50 mm/hr and 4 independent sample cases (3, 6, 10, and 20). It is possible for the ALLRAD instrument to average over a few radar cells to obtain close to 20 independent samples if the increase in accuracy is warranted. Figure 4.4.6 illustrates the sensitivity of estimation error to the number of independent samples for a 1 km penetration depth for rain rates between .1 and 2 mm/hr. The effective reflectivity estimation error at 1 mm/hr from this chart is 58% for three samples averaged and 25% for 20 samples averaged. Therefore, for a 1 mm/hr rain rate, at a 1 km depth, the estimation accuracy can be improved significantly by increasing the number of samples from 3 to 20. According to Figure 4.4.8, for a 1 mm/hr rain rate, at a 4 km depth, the estimation accuracy can be improved only 22%. For higher rain rates (and greater penetration depths), the estimation error decreases because the signal is attenuated to such an extent that the effective reflectivity is very low. Figure 4.4.7 illustrates this effect for a 1 km measurement depth and rain rates between 2 and 50 mm/hr.

In order to determine total rain rate measurement error for the backscatter method, it is necessary to combine the effective rain rate bias

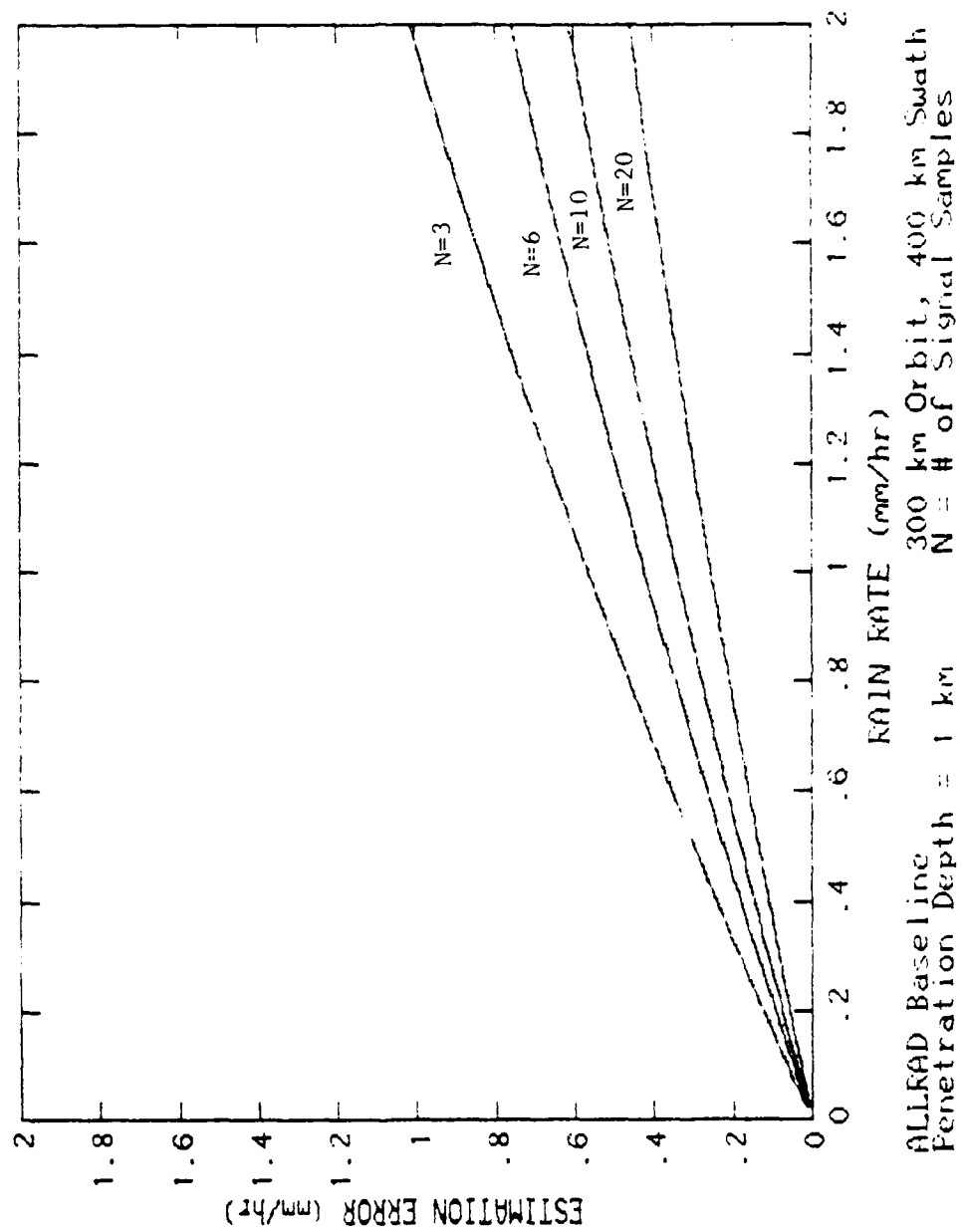


Figure 4.4.6. ALLRAD Backscatter Method Error

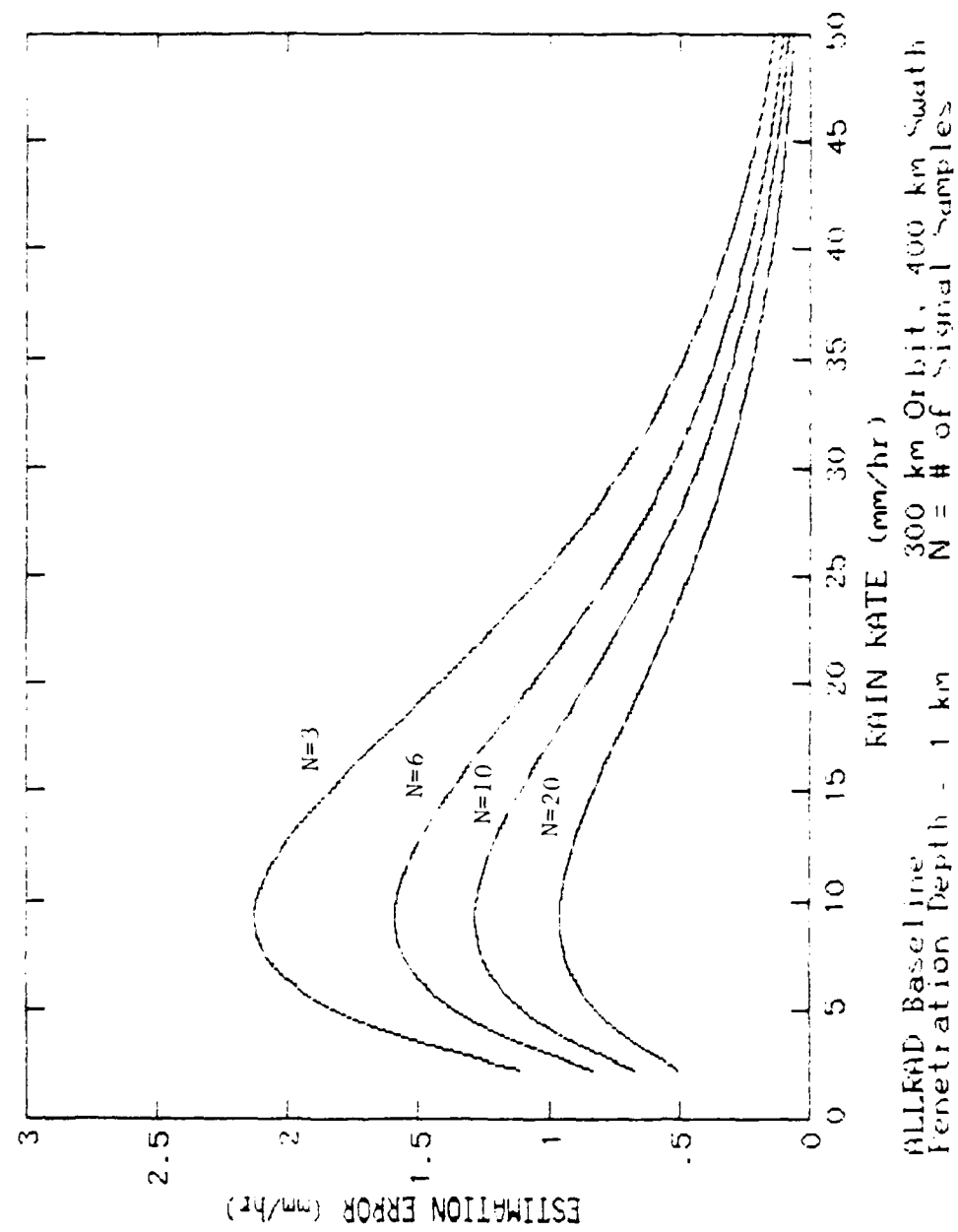


Figure 4.4.7. ALLRAD Backscatter Method Error

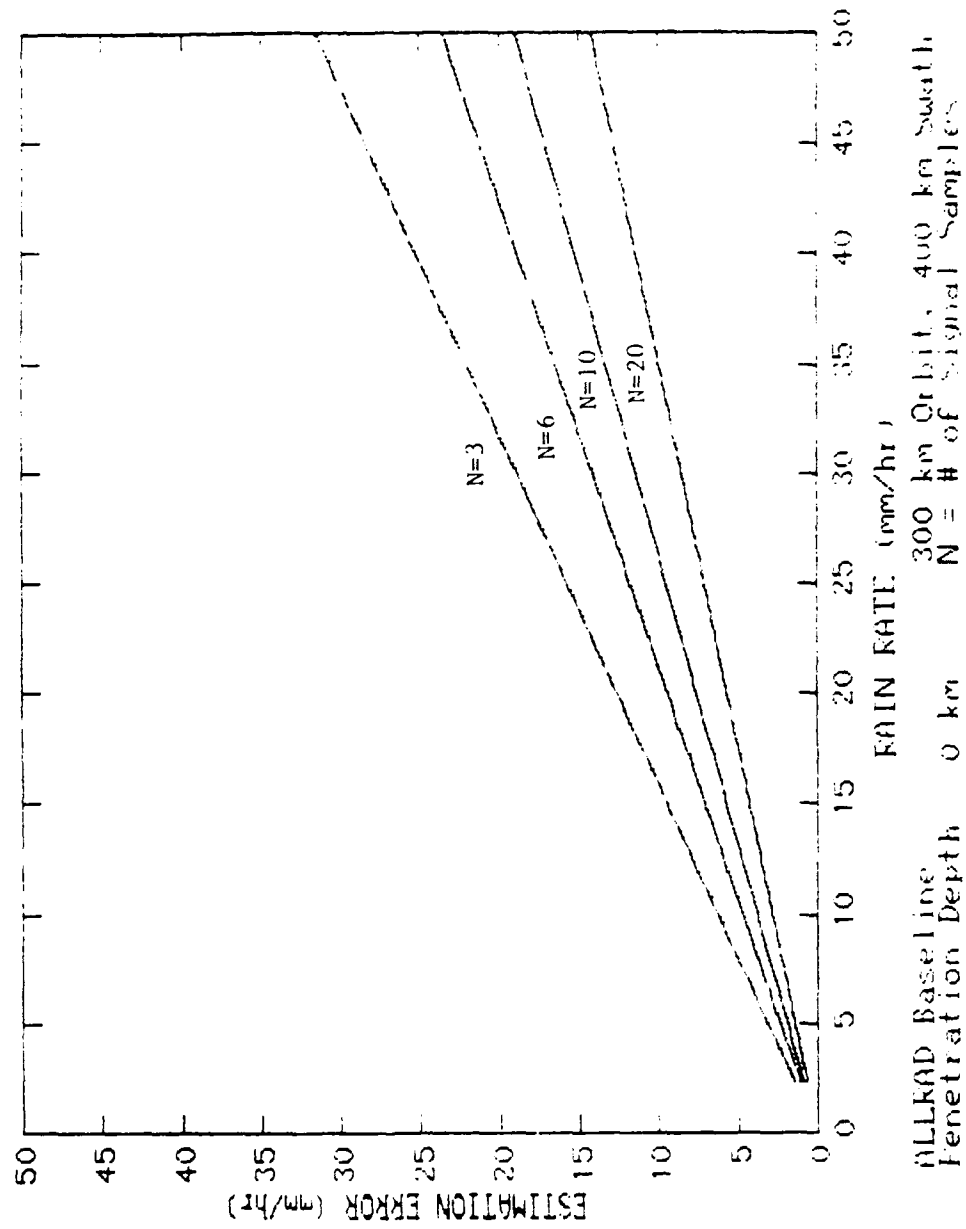


Figure 4.4.8. ALLRAD Backscatter Method Error

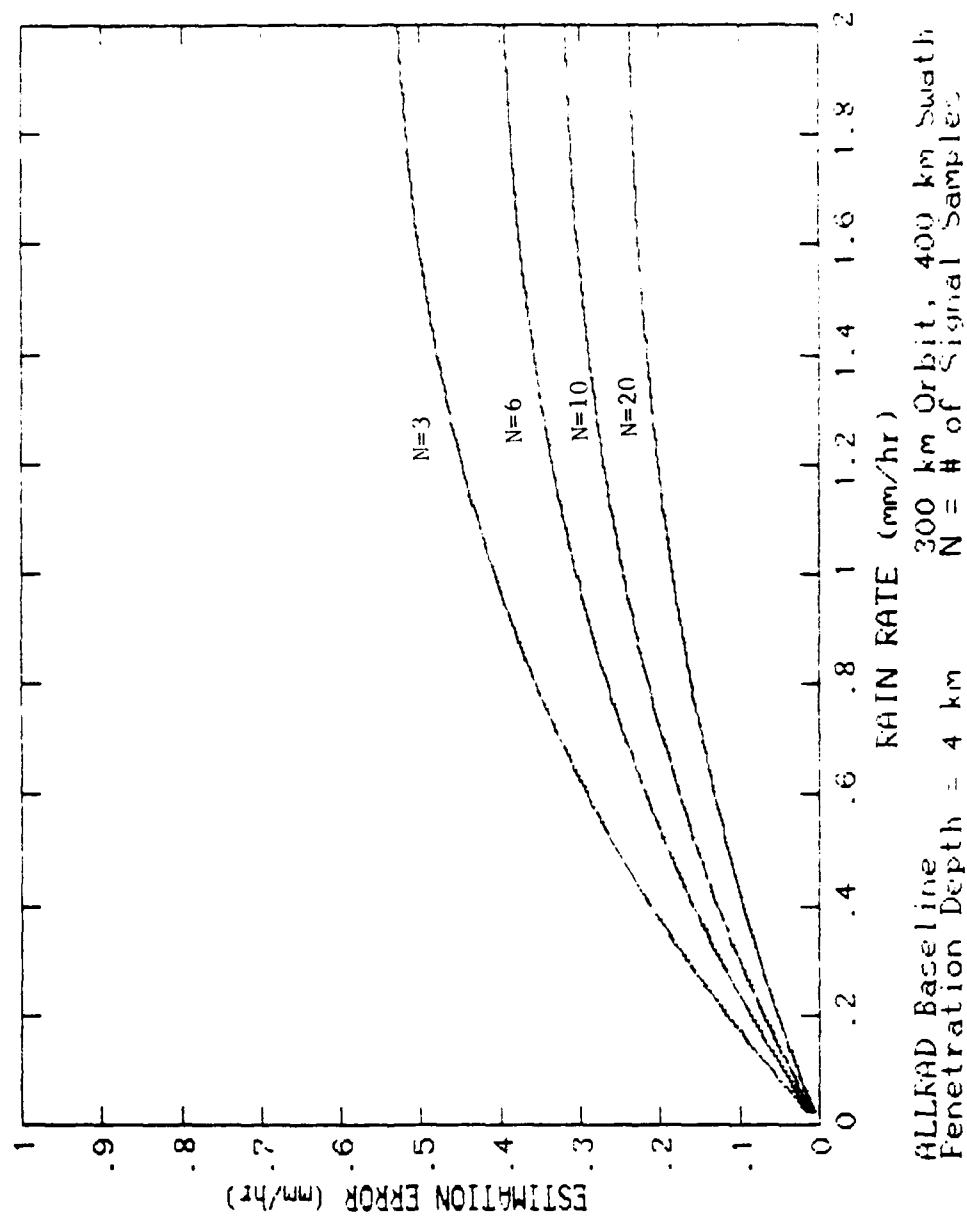


Figure 4.4.9. ALLRAD Backscatter Method Error

with the effective reflectivity estimation error. Table 4.4.1 gives the total measurement error for cases pertinent to ALLRAD. As expected, Table 4.4.1 indicates that the worst case rain rate estimation error increases with rain rate and measurement depth. The difference between 6 sample and 20 sample estimations varies depending on rain rate. Typical of the backscatter technique, a 10 mm/hr rain is measured more accurately at the top of the rain than a 1 mm/hr rain is after attenuation through a 4 km depth.

There are two ways to obtain greater accuracy with the backscatter method. First, at lower rain rates (less than 2 mm/hr) and at shallow measurement depths (less than 1 km), the only way to increase accuracy is to increase the number of samples by spatial averaging (or to use frequency agility). The cost is reduced resolution for the estimated parameters. Detection decisions are still made at full resolution except for very light stratus clouds.

Second, at higher rain rates and greater measurement depths, an independent measurement of attenuation is useful. If the total path integrated attenuation can be measured by scatterometer or radiometer measurements, then an attenuation profile can be inferred using rain rate measurements from the top of the rain mass and an estimate of the melting layer altitude. The attenuation profile is used to obtain a more accurate effective reflectivity which will increase the accuracy of the estimation of rain rate. If the inferred attenuation profile is accurate enough, then the backscatter method can be used for any combination of rain rate and measurement depth where the signal is adequate.

4.4.2.2 Attenuation Coefficient Method

The attenuation coefficient method can be used for rain rates greater than 2 mm/hr over the entire vertical extent of the atmosphere. Similar to the backscatter technique, the attenuation coefficient method is based on an empirical relationship between atmospheric attenuation and rain rate which is given by,

$$\alpha = aR^b$$

According to [36], at 35 GHz the coefficient "a" equals .235 and the exponent "b" equals 1. The linear relation between attenuation and rain rate at Ka-band is independent of drop size distribution. The same is true for the relation between attenuation and cloud LWC.

The attenuation coefficient method is based on a relative power measurement between two different penetration depths in the rain (or cloud). An average path attenuation coefficient is assumed between the two different depths (h_1 and h_2) which is defined as:

$$\bar{\alpha} = \frac{1}{(h_2 - h_1)} \int_{h_1}^{h_2} k(H) dH$$

TABLE 4.4.1 - Backscatter Technique - Total Rain Rate
Estimation Error (%)

300 km Orbit, 400 km Swath, 6 samples/20 samples

TRUE RAIN RATE (mm/hr)	RAIN PENETRATION DEPTH											
	0 km				1 km				4 km			
	EFFECTIVE RATE ERROR (%)	ESTIMATED ERROR (%)	WORST CASE ERROR (%)	EFFECTIVE RATE ERROR (%)	ESTIMATION ERROR (%)	WORST CASE ERROR (%)	EFFECTIVE RATE ERROR (%)	ESTIMATED ERROR (%)	ESTIMATED ERROR (%)	EFFECTIVE RATE ERROR (%)	ESTIMATED ERROR (%)	WORST CASE ERROR (%)
.5	0	±43/30	±43/30	- 4	±44/34	-48/38	-20	±40/22	±40/22	-20	±40/22	-60/42
1.0	0	±43/29	±43/29	-10	±41/25	-51/35	-37	±32/20	±32/20	-37	±32/20	-69/57
1.5	0	±46/28	±46/28	-14	±40/25	-54/39	-48	±26/15	±26/15	-48	±26/15	-74/63
2.0	0	±48/29	±48/29	-19	±39/21	-58/40	-58	±21/13	±21/13	-58	±21/13	-79/71
5.0	0	±50/30	±50/30	-45	±32/17	-72/57	-	-	-	-	-	-
10.0	0	±50/30	±50/30	-65	±19/10	-79/70	-	-	-	-	-	-

The average path attenuation coefficient can also be defined in terms of return signal power, $P_v(h)$, and reflectivity, $\eta(h)$, as follows:

$$\bar{\alpha} = \frac{5}{(h_2 - h_1)} \log_{10} \left[\frac{P_v(h_1)}{P_v(h_2)} \right] + \frac{5}{(h_2 - h_1)} \log_{10} \left[\frac{\eta(h_1)}{\eta(h_2)} \right]$$

The assumption is made that the rain rate is uniform throughout the vertical extent of the atmosphere which makes the second term in the equation above disappear. Based upon the uniform rain rate assumption, an error value of the average path attenuation coefficient is defined,

$$\bar{\alpha}_e = \frac{5}{(h_2 - h_1)} \log_{10} \left[\frac{P_v(h_1)}{P_v(h_2)} \right]$$

which is related to the estimated rain rate as,

$$\bar{\alpha}_e = a R_e^b$$

There are two problems with using the attenuation coefficient method with the ALLRAD radar. First, it is very rare that the rain rate is uniform throughout the vertical extent of a system. If the rain rate increases substantially with decreasing altitude (which occurs at the bright band), then the attenuation estimate is negative. Usually a rain rate estimate is not made when the attenuation coefficient is negative resulting in data dropout in the upper part of the brightband. Also, smaller perturbations in the rain rate with decreasing altitude will bias the attenuation coefficient and cause errors in the rain rate estimate. Second, a large number of samples is necessary to smooth the statistical uncertainties associated with the attenuation coefficient. Figure 4.4.10 is a chart of the estimation errors which arise from the statistical

uncertainties associated with $\bar{\alpha}_e$ for a penetration depth of 1 km and four different sample sizes. Note that it takes a 10 mm/hr rain to bring the estimation error down to 100% when using 6 samples. At 20 mm/hr, the estimation error is still 55% when 6 samples are averaged. When 100 samples are averaged, the attenuation coefficient method works well for 5 mm/hr rains and greater. For the ALLRAD baseline, between 16 and 33 radar cells are necessary to obtain 100 independent samples which degrades the meteorological resolution considerably. It is possible that the attenuation coefficient method would be used for heavy rain situations with a maximum of 20 pulses averaged.

4.4.2.3 Recommendations

The proposed system would use a combination of the backscatter method, the total attenuation derived from the radiometer and scatterometer, and some of the radiometer algorithms developed for SSM/I. The combination should result in better accuracy than can be achieved with each of the individual sensors.

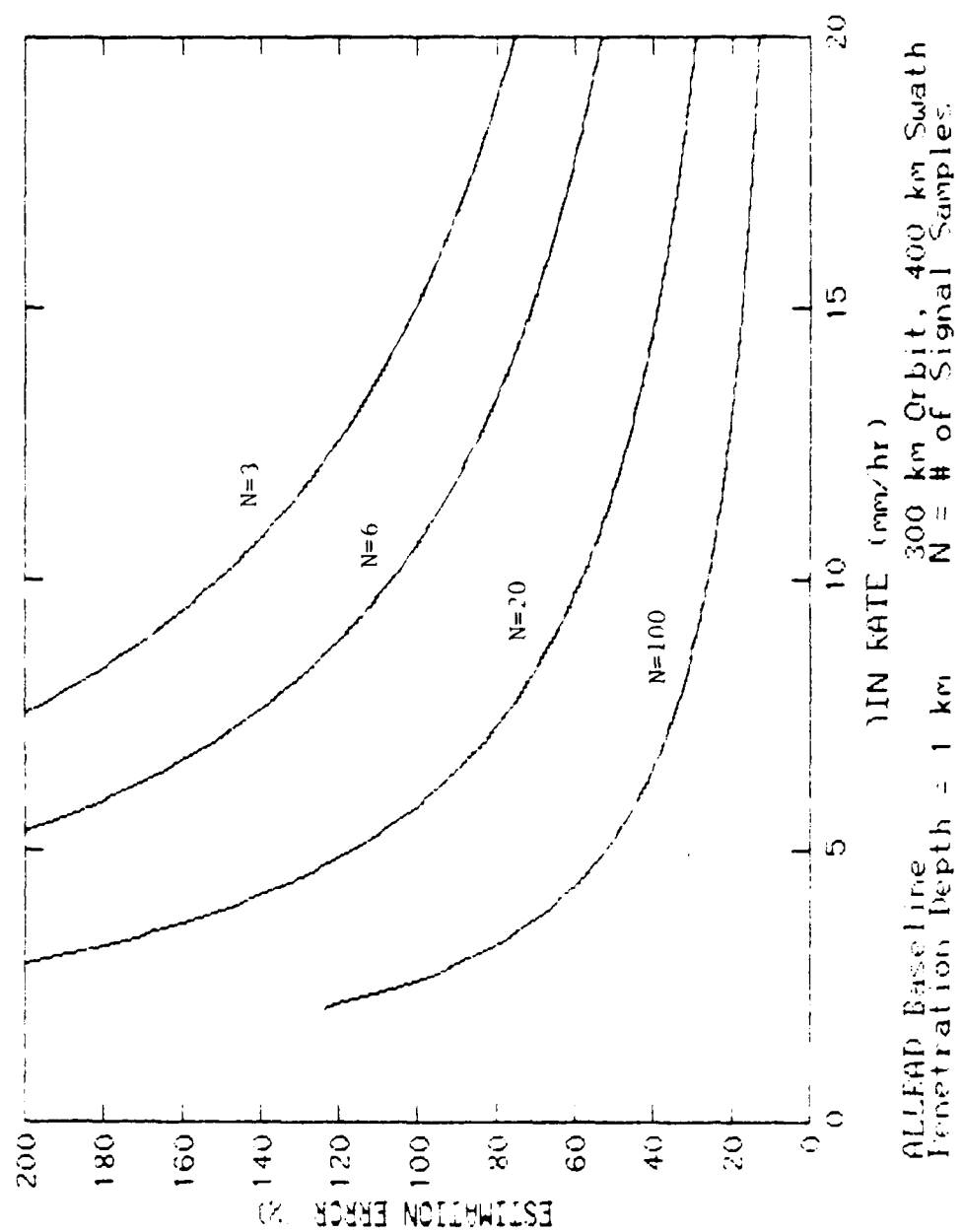


Figure 4.4.10. ALLRAD, Attenuation Coefficient Method

While earlier studies (Goldhirsh [2], TRMM Studies [11]) indicated that a second system at a different carrier frequency (probably at Ku band) was desired to remove the unknown attenuation and "calibrate" the radar system, its utility in the primary goal of cloud measurement is not evident since sensitivity at other lower frequency bands is not adequate. Thus other methods were explored to calibrate the radar that need only yield data in moderate to heavy rains where attenuation is substantial.

Consider that the baseline Radar Sounder consists of a large dish scanning a circular swath on the earth surface as was shown on Fig. 1.1. In the baseline system the nadir angle is 23° . It is noted that there are range cells where the radar is impinging on the surface, and if the reflectivity (σ_0) is estimated, the system is a "SCATTEROMETER", and when over the oceans the output can be used to estimate wind speed and direction similar to the SEASAT SCATTEROMETER or the Scatterometer proposed for NROSS. However, there is an uncertainty in the measurement of σ_0 due to the absorption in the precipitation, and a change in reflectivity due to droplets falling on the surface.

Over land the reflectivity is surprisingly constant in many areas of the earth (Jones et. al. in Elachi [33] Chapter 8) at about 23° incidence, with the spread being only about 2.3 dB between the 20% and 80% points on the distribution. Thus if the radar is calibrated in the absence of clouds or rain, it should be able to estimate the total path attenuation in the presence of clouds or rain. In addition one of the major uncertainties in σ_0 is due to soil moisture. This can be estimated with radiometers at 19 GHz or lower.

Referring back to the calibration of the radar over water, there is a third independent measurement of estimating rainfall rate. If the Radar Sounder is not transmitting, its highly sensitive receiver yields the major portion of an excellent microwave radiometer. Studies have indicated that this is another way of estimating rainfall rates over the ocean. Wilheit et al. (1977, 1982) and the SSM/I Users Guide provided a partial validation of this measurement as is shown on Fig. 4.5.1 and 4.5.2 which are models from the SSM/I Users Guide [36]. The result indicates potential measurement of brightness temperature can be related to rainfall rate in rain up to greater than 16 mm/hour. Absorption/emission and scattering contribute to the measured temperature. One of the uncertainties in that estimate is due to lack of knowledge of the freezing level. However freezing level should be easily estimated by the Radar Sounder. This radiometer should be unique in that the horizontal resolution will be about 2 km which is far better than in other proposed experiments in that this resolution is small compared to the correlation distance of storms and beam filling is more likely.

It should also be practical to operate the Radar Sounder and the Radiometer simultaneously if the radiometer band (about 1 GHz wide) is separated from the radar band by about 1 GHz. For example the radar could operate at 35.6 GHz and the radiometer from 36.6 to 37.6 GHz. A separate receive feed on the same aperture will be proposed for an additional linear

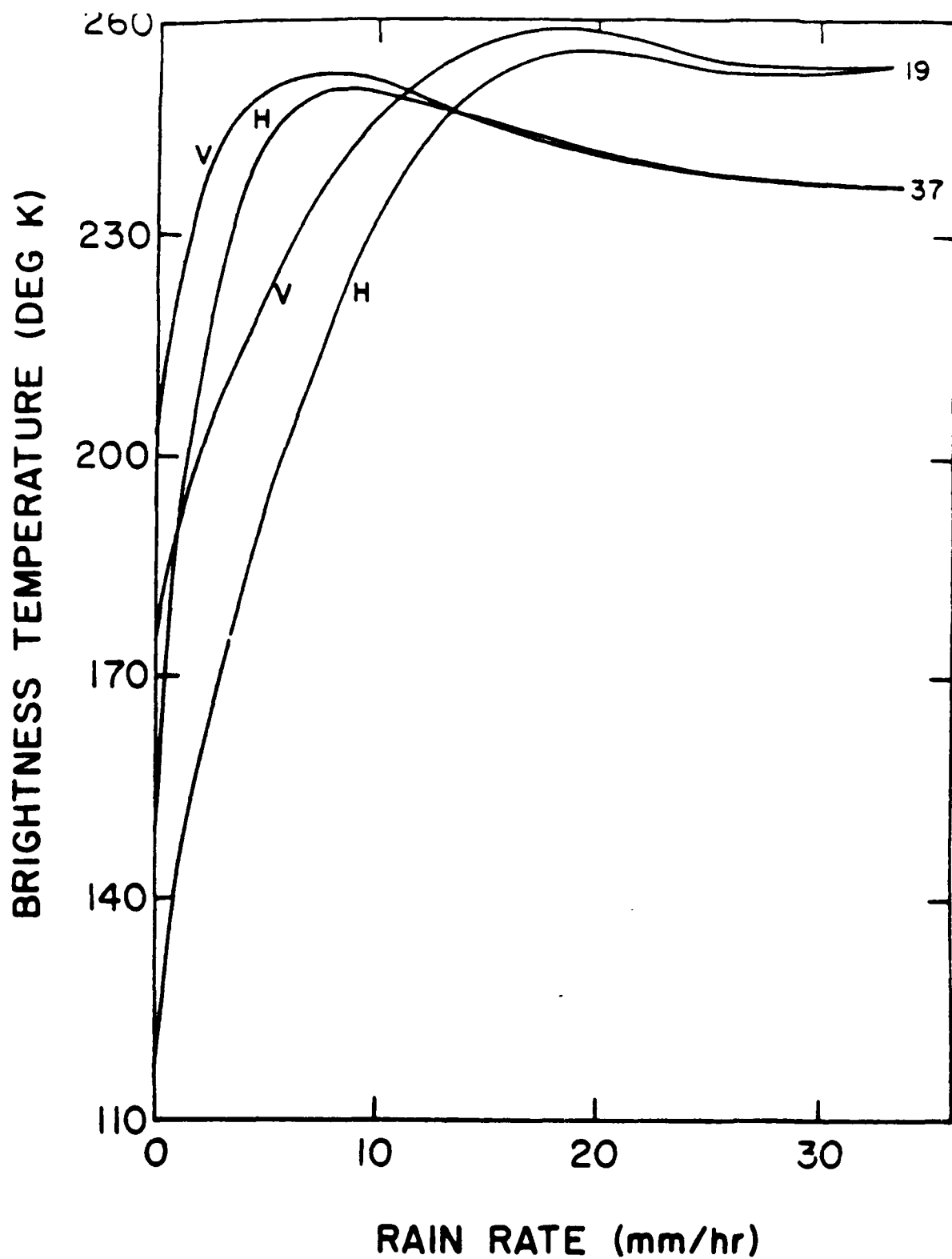


Figure 4.5.1 Brightness temperature vs. rain rate over mid-latitude ocean at 19 and 37 GHz. Ref. [35]

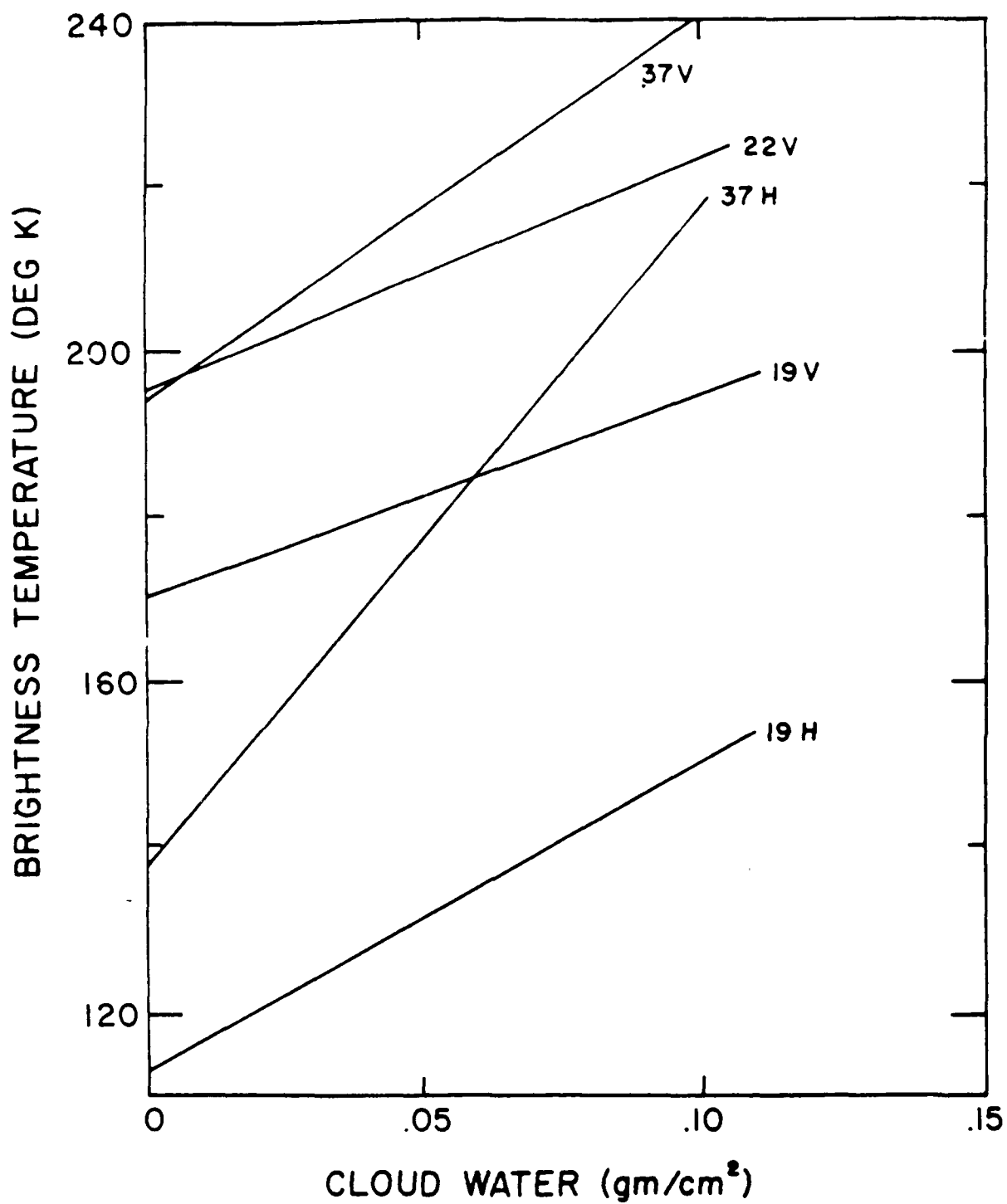


Figure 4.5.2 Brightness temperature vs. cloud water over mid-latitude ocean at 19, 22 and 37 GHz

dual-polarized radiometer channel at perhaps 19.3 GHz. At frequencies below the 22 GHz watervapor absorption line, absorption/emission is the dominant factor while at 37 GHz both absorption/emission and scattering affect the measured brightness temperature.

It is these three (or four) sensors, sharing a common large antenna that form the key elements of a system that should provide a unique opportunity to study all the different phases of precipitation over land and sea areas. It will simultaneously provide high resolution data on the sea surface and its interaction with the atmosphere. The resolution should be adequate to estimate the state and motion of sea ice. The proposed system would have better than 1.0 km resolution in all three dimensions if placed in a low altitude orbit. In a high orbit (>800 km) the radar resolution would be about 2 km. The meteorological resolution would be larger where the greatest sensitivity is required. For example stratus clouds are often reasonably uniform over 12 km in the plane of the earth. The radar cell outputs would be averaged (post-detection integrated) into the larger cells. Signal-to-noise ratio would increase somewhat faster than the square root of the number of radar cells averaged, and the uncertainty in the reflectivity estimate would decrease by a similar ratio.

The relationship between radar and radiometer measurements and meteorological and oceanographic phenomena is of course quite complex and will be addressed in later sections. Table 4.5.1 summarizes some of the relationships that will be utilized. Note that on the Table, LWC_h refers to the liquid water content in the radar resolution cell at a given altitude above the earth. α_h refers to the attenuation through that cell. When there is no subscript, the term represents the summation through the entire atmosphere.

The emphasis to this point has been on the nature of the sensor and its evolution. The system itself evolved from the inability to accurately solve the reflectivity - rain (or cloud) liquid water content equation in the presence of significant attenuation (α). Thus the RADIOMETER and SCATTEROMETER were brought into the system in that they will independently solve other algorithms that have been developed to determine total path attenuation and estimate rainfall rate (R) assuming that the altitude distribution of the precipitation is known. Since the Radar Sounder will know the altitude distribution, the total path attenuation will thus provide an invaluable aid to "calibrate" the Sounder.

TABLE 4.5.1 Multi Sensor Meteorological Instrument

INSTRUMENT	WEATHER	SEA SURFACE	LAND
RADAR SOUNDER	$\eta_h - LWC_h$ $\alpha_h - LWC_h$	$\sigma_o - H_{1/3}^*$ $\alpha - LWC$	
SCATTEROMETER	_____	$\sigma - H_{1/3} \cdot V_W$ $\alpha - LWC$	$\sigma = \text{CONSTANT}$ $\alpha = LWC$
RADIOMETER	$T_w - LWC, \text{ICE}$ $\alpha - LWC$	$T_s = H_{1/3}$	

 η - REFLECTIVITY

LWC - LIQUID WATER CONTENT

 α - ATTENUATION

* NEAR CONTANT SLIGHTLY OFF NADIR

 σ_o - SURFACE REFLECTIVITY V - WIND VELOCITY VECTOR $H_{1/3}$ - SIGNIFICANT WAVE HEIGHT

4.6 SYSTEM BLOCK DIAGRAMS

This section presents preliminary, functional system block diagrams of the ALLRAD instrument design. Figure 4.6.1 is a top level system diagram. It shows the top level functional areas and the interfaces between them.

Figure 4.6.2 is a more detailed radar system block diagram. As indicated, the low noise RF amplifier feeds the received radar signal to a Local Oscillator (LO) where the signal is mixed down to produce the IF signal. Next, the IF signal is mixed with a Voltage Controlled Oscillator (VCO) signal which contains the expected Doppler shift. The resultant velocity compensated signal is matched filtered and converted to bi-polar video via two LO's which are 90° apart in phase. These in-phase (I) and quadrature-phase (Q) signals are A/D converted and sent to the signal processor. The root-mean-square noise estimator is used to estimate the receiver noise power over large sample sizes which is used for instrument calibration and geophysical parameter retrieval algorithms.

It should be determined at a later time if both polarization channels of a 37 GHz radiometer be implemented. If circular polarization is used and only one sense is necessary, one of the polarizations out of the array feed should be used for radar and the other for the radiometer. If linear polarization is implemented, the radar and radiometer can share the wideband low-noise amplifier and then split by a frequency duplexer.

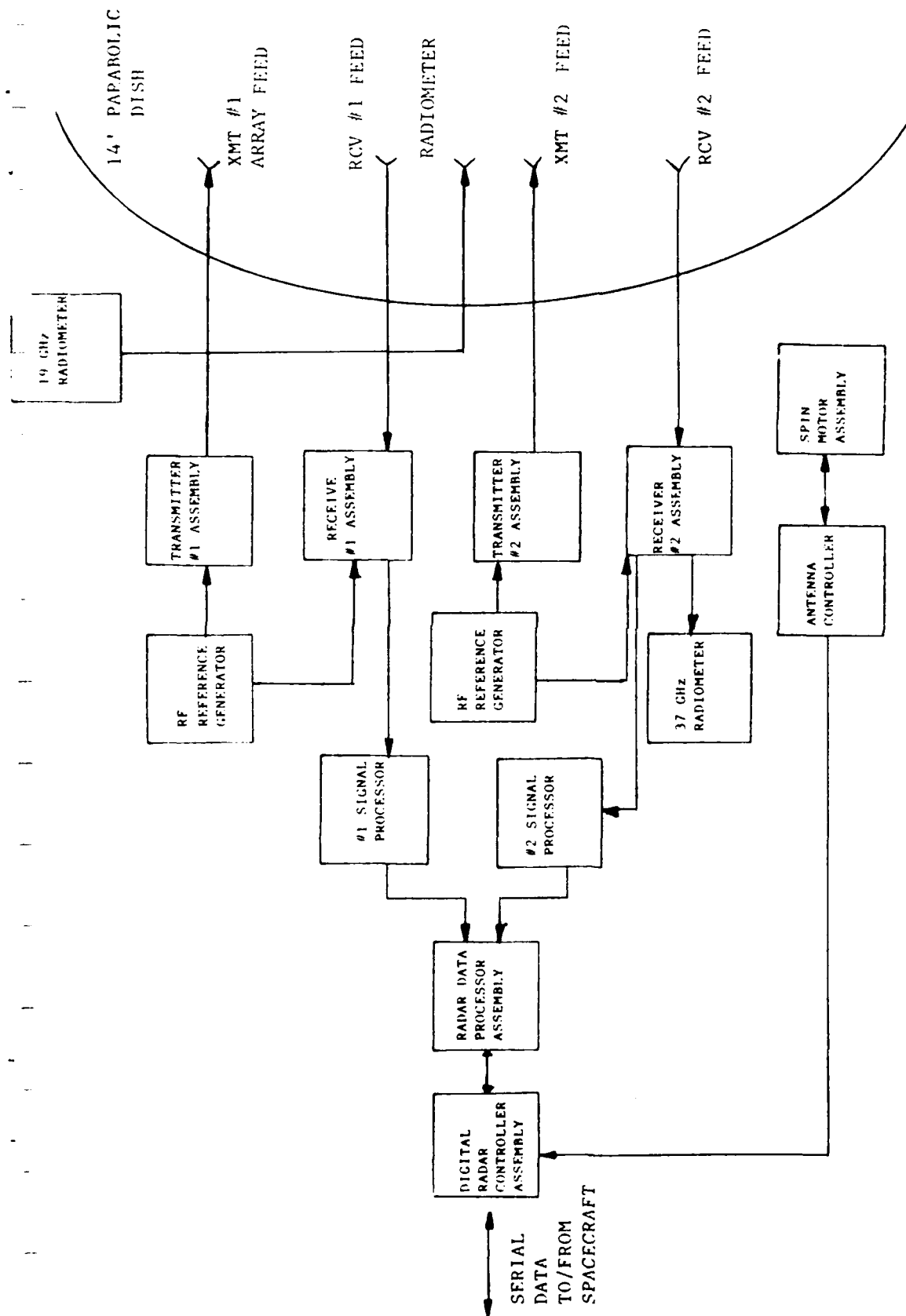


FIGURE 4.6.1 ALLRAD INSTRUMENT TOP LEVEL SYSTEM DIAGRAM

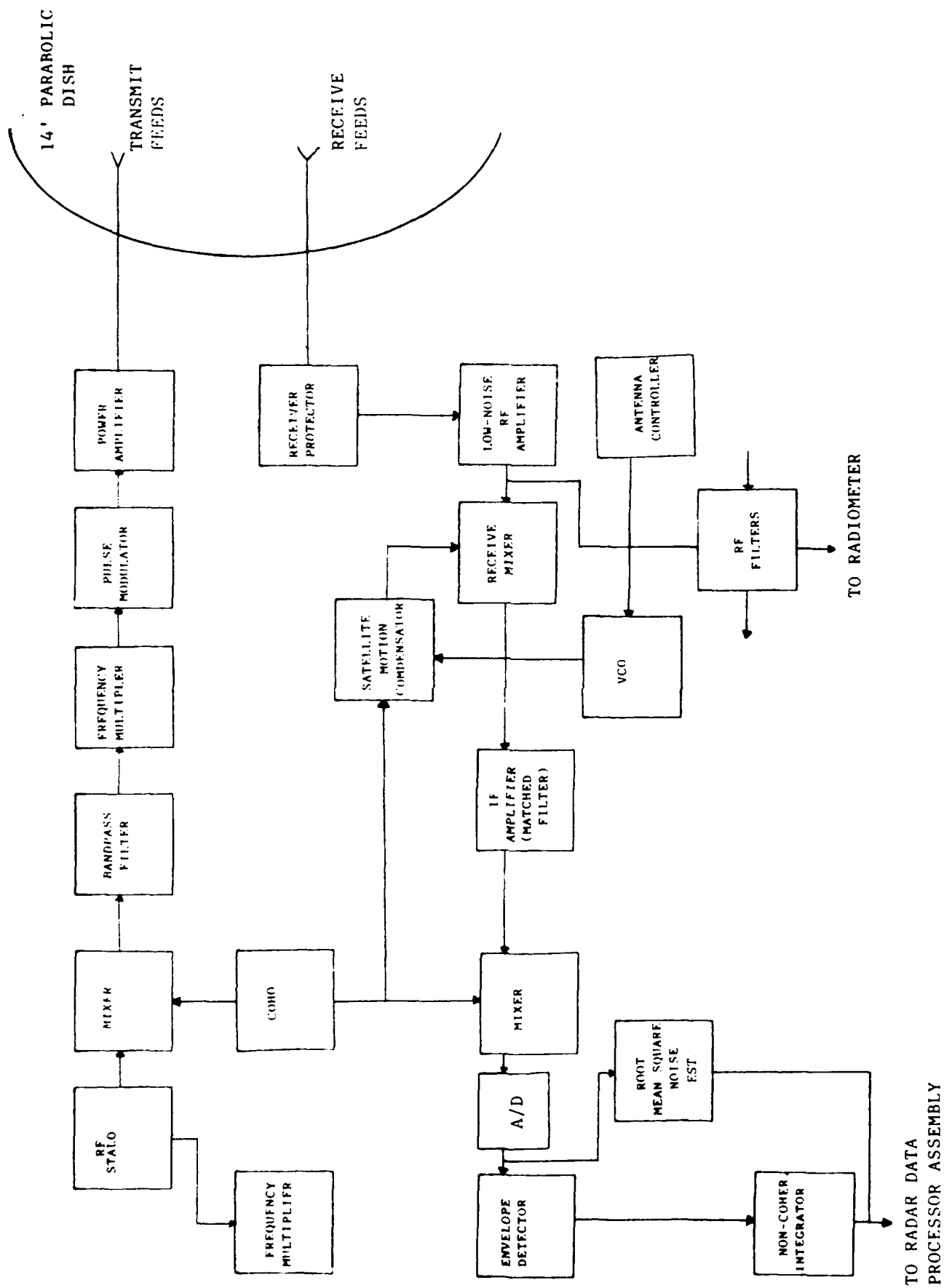


FIGURE 4.6.2 ALLRAD RADAR SYSTEM BLOCK DIAGRAM

5.0 SYSTEM IMPLEMENTATION BASED ON HARDWARE STATE OF THE ART

5.1 TRANSMITTER AND POWER SUPPLY SELECTION

A survey was made on possible radar transmitter tubes, and it is believed that at least one type meets the requirements. A brief summary table of available tubes is shown on Table 5.1.1. There are several possibilities at 35 GHz including Traveling Wave Tubes, klystrons and Electronic Interaction Amplifiers (EIA). Magnetrons were not considered as they are noisier and out of favor with those assigning spectrum allocations. The Traveling Wave Tubes are less desirable due to the generally higher anode-cathode voltages (e.g., 37 kv) that are undesirable in space. While the EIA has the lowest voltages, the peak power is limited to considerably less than desired. The klystron and especially variations of the Varian (California) VKA 1852 seem to be most suited to the radar application.

The basic tube has been in the Varian catalog for at least seven years and about 20 have been delivered. The variant of most interest is the five cavity version that produces 6520 watts peak power shown on Table 5.1.2. Two tubes have been built for a missile seeker application where shock and vibration would far exceed satellite launch conditions.

A higher peak power version which would produce 10 kw of power is shown on Table 5.1.3. Both of these tubes can produce high average power with liquid cooling, but it is recommended that the average power be limited to 150 watts and use the simpler conduction cooling. They use permanent magnets and only weigh 12-15 pounds. Beam voltage is about 18 kv.

A tube for this application would only need 4 cavities which would allow a smaller and simpler tube, with lower drive power but would reduce the bandwidth to about 40 MHz. This bandwidth is far more than needed for the proposed application. The lower drive power will allow the use of simple solid state drivers.

The tube would need to be space qualified with the key item being the lifetime. The current cathodes yield 6000-10,000 hours. Varian is working on a program to achieve 100,000 hour lifetimes on other tubes. A recommended program would be a complete paper design (~\$25K, 3 months) followed by building samples with current cathodes and parallel efforts on a longer life cathode. Final tubes with space qualification testing would complete the program in about 3 years. The time scale fits well. The non recurring cost estimate for space qualification is \$1.0-1.2 million with subsequent tubes costing about \$75K.

The high voltage power supply is also a critical item for spacecraft, but the voltages are not uncommon for military spacecraft. In this system, the very moderate and fixed PRF and pulse duration will simplify the power supply design.

The radar transmitter includes the transmitter tube (a Varian Klystron), the high voltage power supply, the modulator plus monitoring and other peripheral equipment. The tube and the high voltage power supply are the more critical items.

TABLE 5.1.1

Transmit Tubes for 35 GHz

Manufacturer	Varian	Hughes	Hughes	Varian	Varian	Varian
Type	EIO	TWT	TWT	Kyl.	TWT	Mag.
Freq. Range (GHz)		33-36	33.5-36.5	33-36	34.5-35.5	34.86
Bandwidth (1 dB)	70 MHz	3000	3000	130	1000	
Peak Power (kw)	2	4	3.5	2.5/6.6*	30	150
Avg. Power (W)	200	120/220	175	250/300*	3000	75
Duty Factor	.10	.03	.05	.10/104*	.10	.0005
Weight (Kg)	13	7.7	72.7**			
Anode-Cathode (KV)	8	37		14/20	47	23
Anode-Body (KV)	14				73	
Pulse Width (μ s)	10				100	
Cathode Current (A)	1.0	1.1		1.0	4/5	22
Length (inches)	13	18	21	6	25	
Efficiency				18%		
Gain (dB)		46	45	46	50	
Cooling	liquid	air/liquid		liquid	liquid	

* Projected in 1982

** Full Amplifier Package with 921H Tube

TABLE 5.1.2

Five Cavity Klystron Amplifier

	<u>MIN</u>	<u>NOM</u>	<u>MAX</u>
Peak Power Output (across band)	5000	6250 W	-----
Average Power Output (across band)	-----	-----	800 W
Efficiency (band edge)	16%	17%	-----
Efficiency (band center)	-----	21%	-----
Bandwidth	100	120 MHz*	-----
Ripple	-----	-----	± 0.5 dB
RF Drive	-----	0.63 W*	0.8 W
Beam Voltage	-----	18.3 kV	18.8 kV
Beam Current (Peak)	-----	1.61 A	1.68 A
Body Current (Peak)	-----	13 mA	60 mA
Grid Bias On	+350	+371 V	+403 V
Grid Bias Off	-----	-371 V	-403 V
Grid Current (Peak)	-----	5 mA	15 mA
Heater Voltage	5.6	6.0 V	6.3 V
Heater Current	-----	2.7 A	3.5 A
Diameter	-----	4.4"	-----
Magnet Length	-----	3.3"	-----
Package Length	-----	6.3"	-----
Package Weight	-----	12.3#	15.1#

* About 90 mW drive with a 65 MHz bandwidth.

From Varian, California

TABLE 5.1.3

Five Cavity Klystron Amplifier (10 kw)

	MIN	NOM	MAX
Peak Power Output (across band)	8000 W	10000 W	---
Average Power Output (max within band, liquid cooled)	---	---	1000 W
Average Power Output (max within band, conduction cooled)	---	---	200 W
Efficiency (band edge)	16%	17%	---
Efficiency (band center)	---	21%	---
Bandwidth	50 MHz	65 MHz	---
Ripple	---	---	+/- 0.5 dB
RF Drive	---	90 mW	120 mW
Beam Voltage	---	22.0 KV	23.0 KV
Beam Current (peak)	---	2.12 A	2.5 A
Body Current (peak)	---	13 mA	60 mA
Grid Swing (on/off)	---	+/- 460 V	+/- 500 V
Grid Current (peak)	---	5 mA	15 mA
Heater Voltage	5.6 V	6.0 V	6.3 V
Heater Current	---	2.7 A	3.5 A
Diameter	---	4.8 in.	---
Magnet Length	---	4.3 in.	---
Package Length	---	7.3 in.	---
Package Weight	---	15.3 lbs.	17.5 lbs.

The power supply is difficult in the sense that it must be physically large to handle the high voltages without arcing and to restart if there is an arc in the tube or power supply. The tube is the longer lead time item as the power supply can be built for space in about 2 years. However, there are very few contractors that have built these supplies for space programs. The information on the power supply is mostly from Westinghouse who has built these supplies. The tube information is modified from Varian estimates. A power supply using a gas filled dielectric is currently favored over a "potted" version even though it would be heavier (~140 pounds). Expected power supply efficiency is 75-85%.

5.2 Thermal Control

Thermal Control is provided for 2 Klystron Tubes. Each Klystron Tube has a maximum power dissipation of 1 KW (150 W radiated, ~600 W dissipated), a footprint of about 27 in², and an assumed operational temperature range of 50°C to 120°C. Tubes of this specific power density (5W/in³) and size are capable of removing internal heat dissipation by conduction, whereas units with significantly higher power densities may require liquid cooling. The tube itself will not be damaged with a much broader temperature range.

For a tube operating over a 70°C range, thermal control may be provided by a cold plate mount rejecting part of the heat directly to the spacecraft structure. For loads of up to 1.5 KW (both tubes) it is likely that some cooling augmentation would be required for the cold plate mount. This may be achieved by a heat pipe thermal link from the cold plate mount to an external panel radiator. By this approach the thermal capacitance of the bay structure would be available to limit the instantaneous heat load, the spacecraft exterior would provide part of the basic bay heat rejection and the more efficient panel radiators would provide the required operating range. Assuming that the spacecraft bay accepts only a small portion of the thermal load, the panel radiator might be 3 feet square per tube. Additionally, the panels might appear at opposite or removed locations on the spacecraft structure to achieve an improved instantaneous average view for heat rejection. In any case, it does not appear to be a difficult problem.

5.3 Antenna Considerations

The large antenna aperture is key to the sensitivity to detect clouds and to obtain the desired resolutions. In addition to the high gain requirement, there is the requirement to have extremely low sidelobes to eliminate the ground echoes while observing low altitude clouds. Both of these requirements lead to tight antenna tolerances (<10mils).

The proposed antennas are derived from antennas proposed by Harris Corporation, Melbourne, Florida, for the NROSS Low Frequency Microwave Radiometer. One of the proposed antennas for that program was a 23 foot deployable mesh. For the baseline Allrad antenna, there were two designs considered; a 6 meter deployable mesh, and a 4.1 meter solid reflector. With a Titan launch vehicle, the 4.1 meter reflector can easily be stowed in the vehicle envelope. The 6 meter deployable mesh was not rejected because of tolerance problems, but because of the larger weight and the larger spin subsystem to compensate for that weight.

For a low altitude orbit (~300 km) and Delta size launch vehicle, the antenna diameter might be reduced to 3.3m.

Since the feed structure is somewhat complex (see Sec. 5.4), an offset paraboloid was chosen to keep the sidelobes low. The close-in sidelobe requirement has a worst-worst case need for -(31-33) dB when the clouds are above a background of refrozen snow. Over other areas -30 dB sidelobes are adequate. The proposed design is for a -35 dB Taylor taper. A drawing of the proposed configuration is shown as Fig. 5.3.1. The feedhorn is folded toward the reflector for stowage. Overall efficiency including taper and losses is at least 40%.

Tight tolerances will be sought to keep all sidelobes at a low level and a surface error of less than 0.25mm is expected. The gain will be about 60 dB. In a large aperture there is an advantage in that if the tolerances are met, the gain of the far out sidelobes are less or equal to 0 dB or 60 dB down from the main beam on both transmit and receive. This will prevent large specular echoes such as the nadir reflections from entering the receiver at levels comparable to cloud echoes.

The low noise receivers will be placed at the array feed output to minimize losses. The transmitters (2) will not be at the feed but will be connected by very low loss circular waveguide. This is practical since the transmit bandwidth is quite low.

The antenna subsystem as proposed should weigh under 100 kg including the array feed, the reflector (68 kg) and the boom.

An alternate configuration assumes that the long axis of the spacecraft is vertical (relative to nadir). The transmitter is placed near the top of the spacecraft and the array feeds are on the top itself. The dish is attached to a rotating boom above the top and its boresight is about 20° off nadir. While the design is more complex, the losses are lower and the rotating weight is less.

14 FOOT NON-FOLDING MESH REFLECTOR

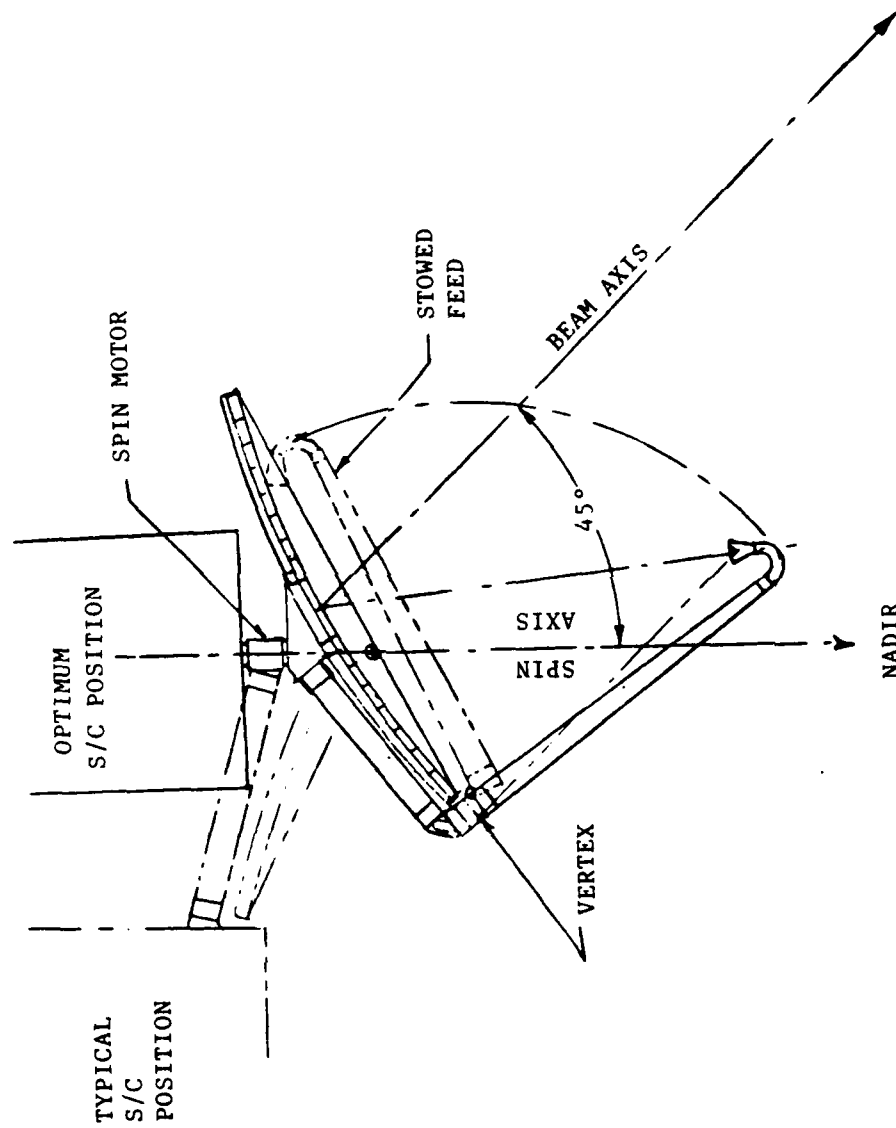


Figure 5.3.1

5.4 Antenna Feed Design

With a rotating radar on a spacecraft there are unique antenna problems with the slant ranges observed due to both high altitudes and large swath diameters. In the round trip time to the precipitation, the satellite antenna moves along its track and rotates away from the point at which the transmit antenna was pointed.

The along track calculation is relatively simple for a velocity of 7700 m/sec and a slant range of 900 km the approximate distance the footprint moves in the round trip time is; $900 \text{ km} \times 6.8 \mu\text{sec/km} \times 7.7 \text{ km/sec} = 47 \text{ meters}$. Since this is small compared to the footprint size of about 1500 m, it can be neglected for sensitivity considerations.

The antenna rotation is more complex and more of a problem. Depending primarily on the swath diameter the receive antenna is rotated an excessive amount. The separation of transmit and receive beams is shown on Figure 5.4.1 to be comparable to a beamwidth. For a relatively narrow swath of 200 km, the displacement is about 0.5 beamwidth and the signal loss would be excessive. For swaths of 400 km or greater, the angular displacement would be greater than one beamwidth and would of course be unacceptable. The above are for the proposed 17 RPM rotation rate. Note how little the sensitivity is to orbit altitude.

A separate feed horn for transmit and receive is thus necessary. However, each feed horn must be physically large to get the proper taper for the illumination function. It is likely that they cannot be physically placed at the proper locations. The solution to this is called an "array feed" as illustrated on Figure 5.4.2. The numbers represent array elements for the "A" transmitter and receiver. Depending on the swath width, the transmit beam might be formed by radiating through 1, 2, 5, 6, 7, 10, 11 and receiving through 3, 4, 7, 8, 9, 12, 13. Array feeds provide controlled illumination at the price of some losses. An example X-band array feed is shown on Figure 5.4.3.

ALLRAD XMIT AND RX BEAM SEPARATION

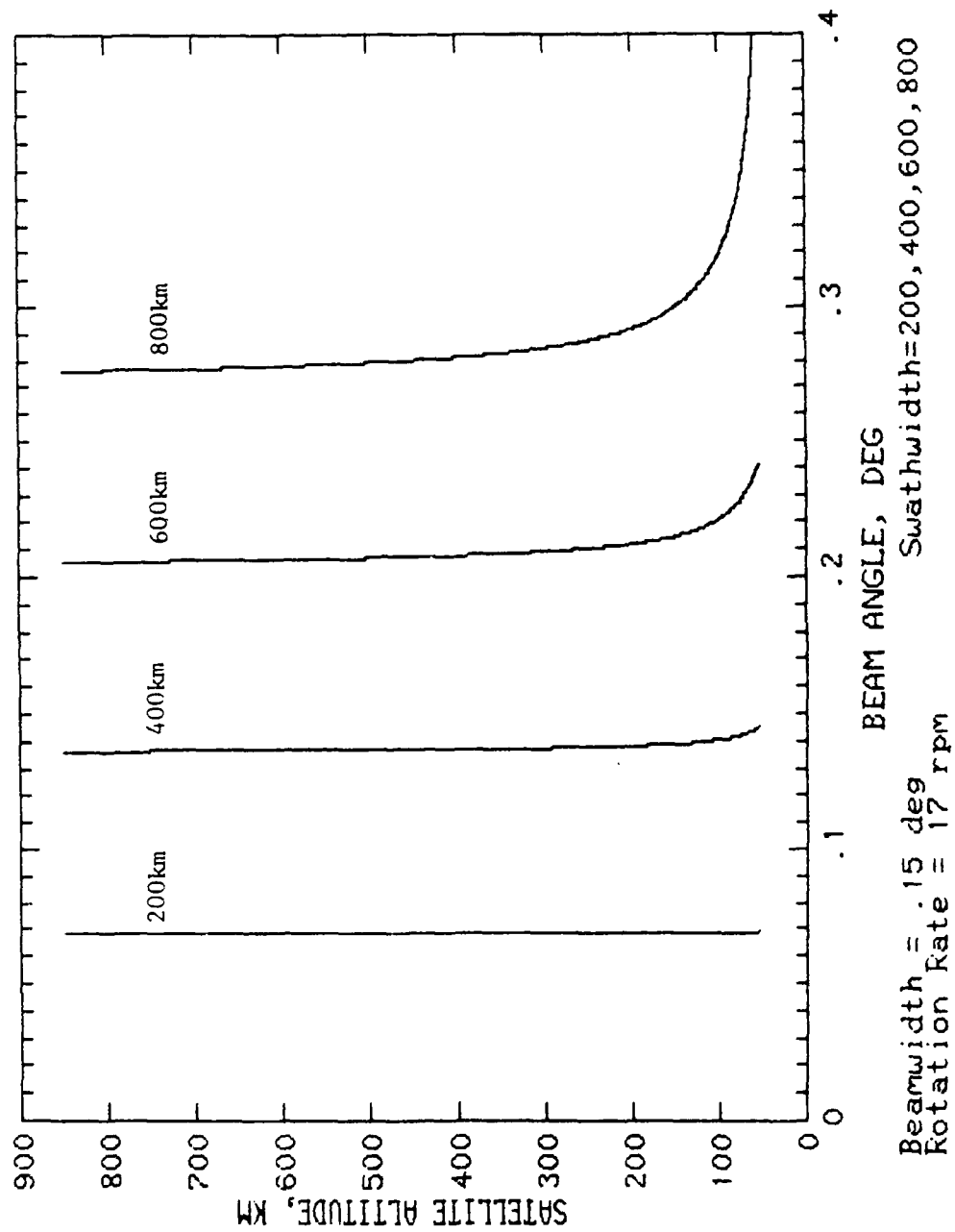


Figure 5.4.1

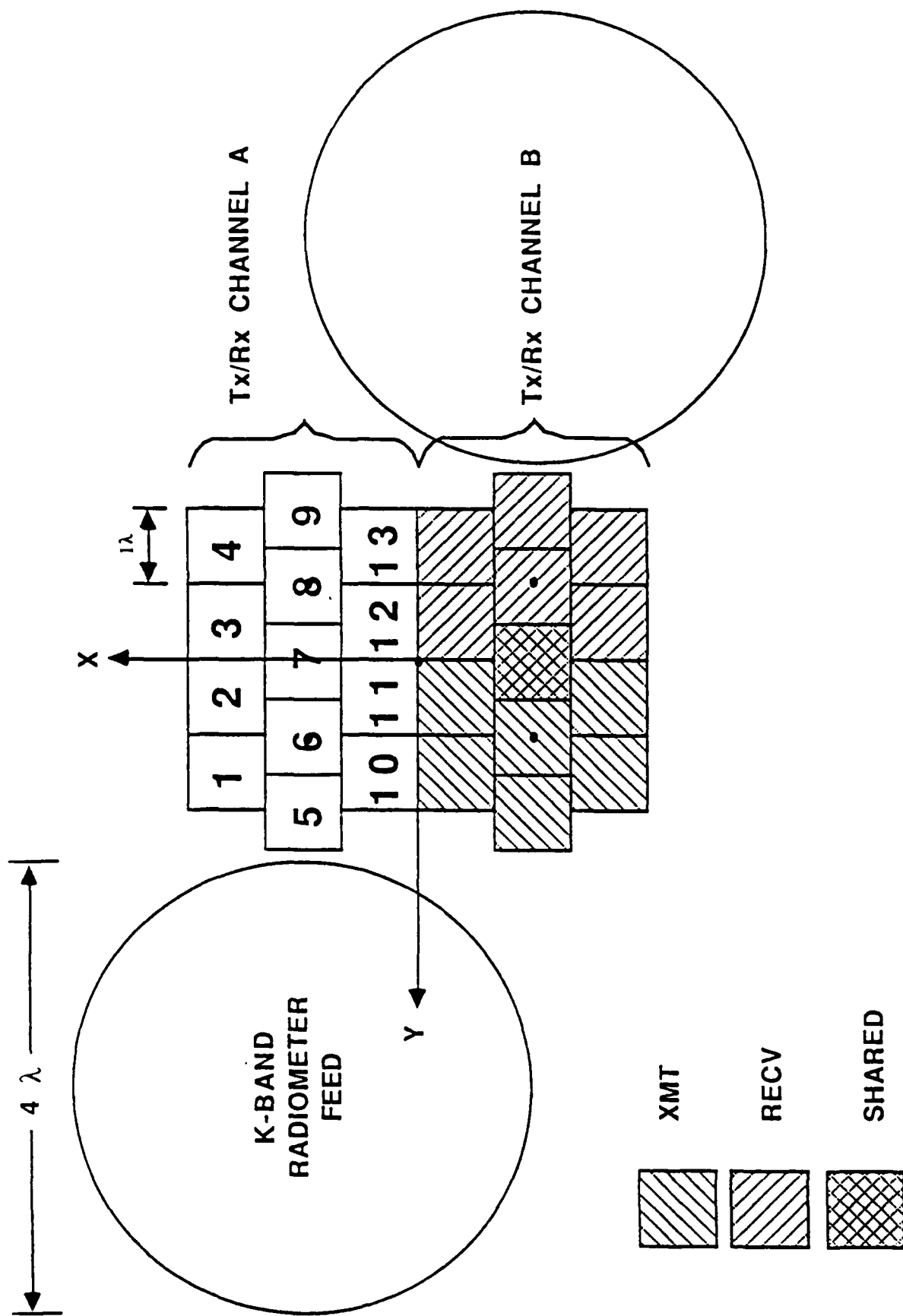


Figure 5.4.2 Ka-Band Feed Cluster

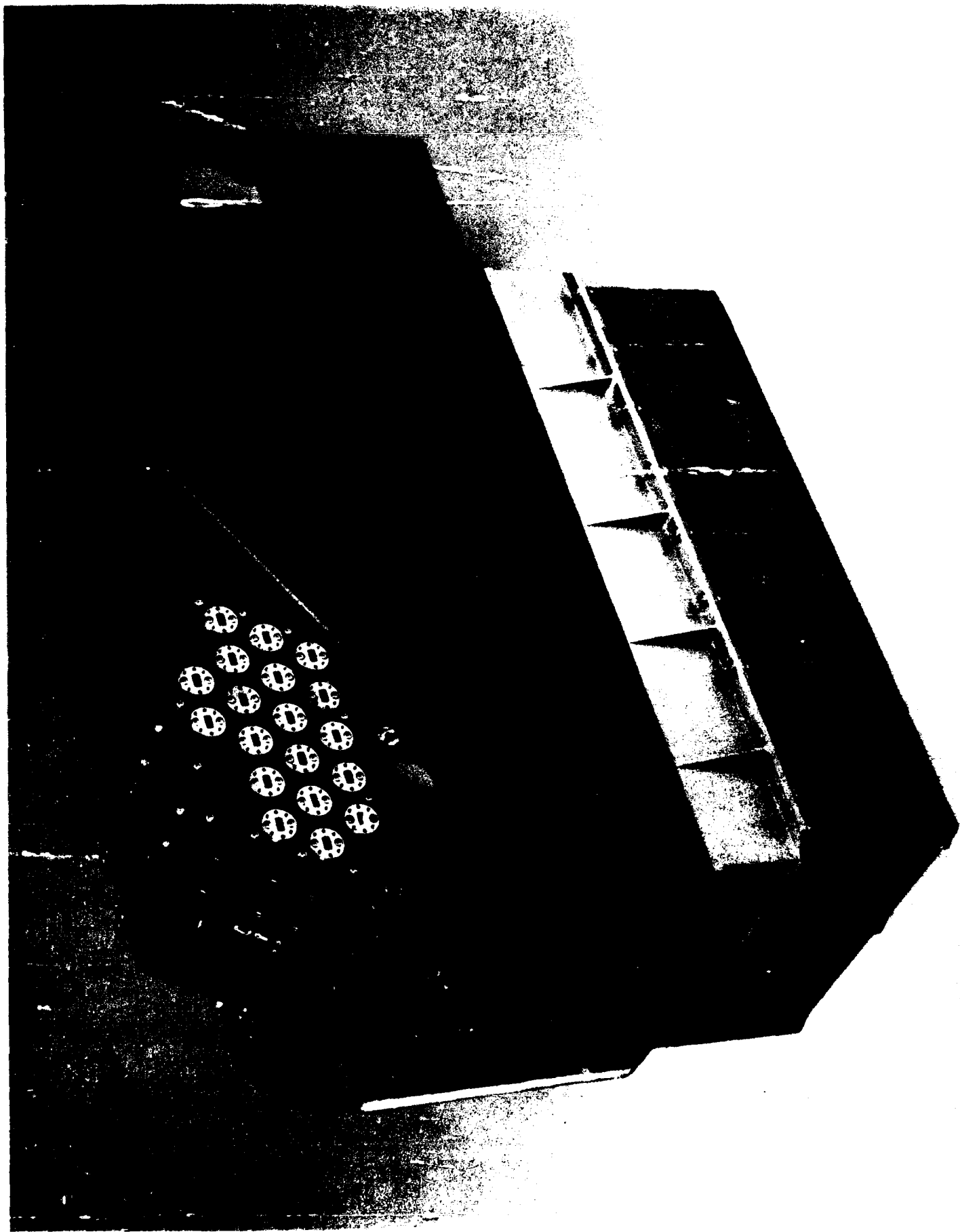


Figure 5.4.3

5.5 Receiver Noise Temperature

The receiver would be a solid state low noise amplifier with a bandwidth that covers the radar and radiometer. The basic relationship for receiver noise temperature, T_S is;

$$T_S = \frac{T_a}{L_{RF}} + \frac{L_{RF}^{-1}}{L_{RF}} (T_{RF}) + (NF-1) 290^\circ$$

where T_a = antenna temperature which varies depending on where the antenna is pointed. It will be higher for land and cooler for snow, ice and oceans. Assume 200° as an average.

L_{RF} = Losses receive antenna to low noise amplifier (LNA)

T_{RF} = Physical temperature where losses exist

NF = Noise Figure of LNA. Values of 2.0-2.5 dB for the multistage amplifier should be available from Millitech, Hughes, and G.E. (see Figure 5.7.1)

It is expected that the receive losses will be 1.5 to 2.0 dB. Since T_a is significant for spacecraft looking at the surface, the value of L_R does not have a major effect on T_S as the first term decreases as L_R increases and the reverse is true for the second term.

T_S will vary since the receiver is also a radiometer, but 500° should be a reasonable bound for T_S in the early 1990's.

The dynamic range of the receiver must be sufficient to detect the weakest cloud, and also not to saturate on highly intense storms or the reflections from the earth's surface. The intense storm is somewhat difficult to model in that the strongest signals are generally near the earth's surface, and the radar signal has been heavily attenuated before it reaches these strong reflections. In the models used in this study, the storms are about 58 dB above the stratus cloud model reflectivity. Expected attenuation is about 32 dB total. Recognizing that there will be some strong cells at higher altitudes, we should not count on anywhere near that level of attenuation.

The maximum surface reflectivity at these angles is only from 2 or 3 radar resolution cells at the surface. Refrozen snow has the highest reflectivity and will yield a mean signal that is about 62 dB above the weaker stratus model. Wet or snow and land echoes are 6-8 dB lower.

The return from the stratus model is several dB below that of the receiver noise on each pulse. (The final signal-to-noise ratio is established by integrating at least 20 pulses.) Thus, if the least significant bit in the A/D conversion process is 3 dB below the rms noise, the input dynamic range is about 58 dB for intense rain (with no attenuation) and 62 dB for surface snow.

An electronic gain control switch could be turned on for the surface echo, but it may introduce a transient at a critical range between the atmosphere and the surface. If it is implemented, the timing must be carefully controlled.

One other factor must be taken into account is that all the echoes have a Rayleigh distribution, and to get accurate readings we need to allow about 2 bits extra for the inherent fluctuation. Thus while a 10 bit plus sign A/D converter would handle the basic dynamic range, it is recommended that 12 bits plus sign be specified. Since the bandwidth is low, these are currently available from the radar manufacturers at modest cost. They are used in many ground based surveillance radars.

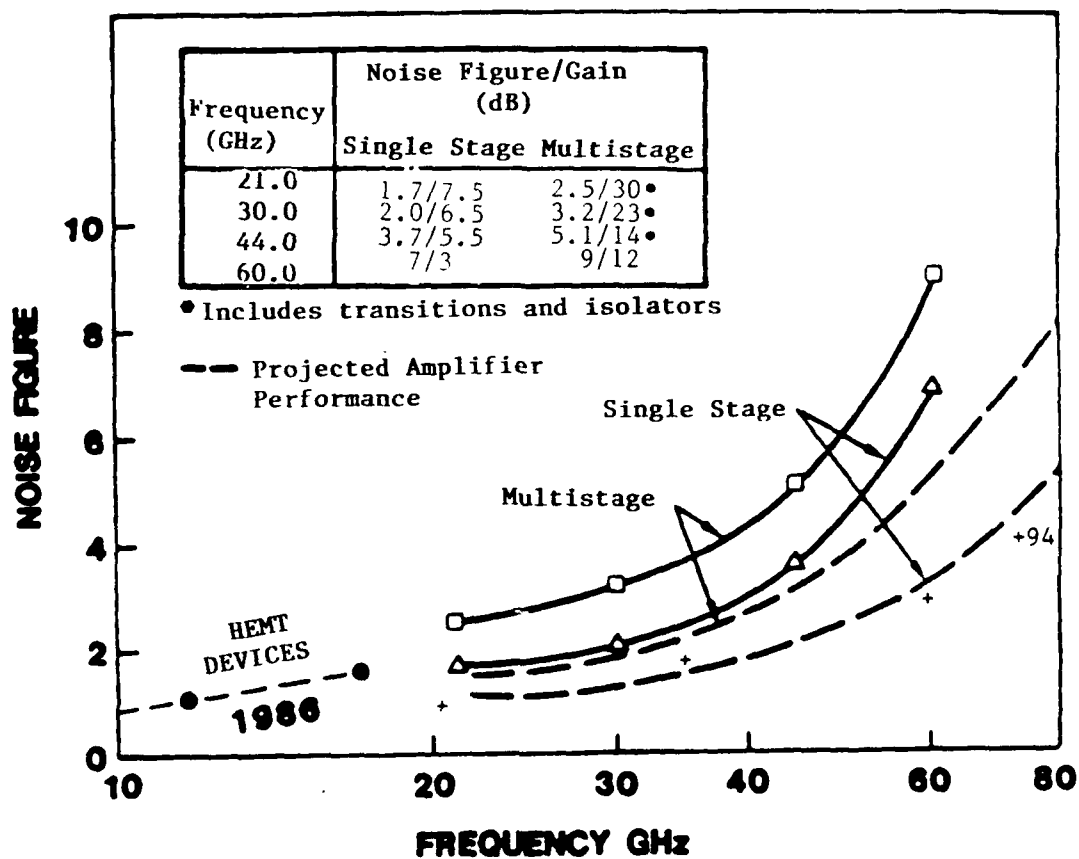


FIGURE 5.6.1 LNA STATE OF THE ART

Hughes FET LNA performance is plotted at 21, 30, 44, and 60 GHz. The solid curves represent the best actual achieved performance, and the broken curves represent expected improvements within the next few years. (Hughes Aircraft 1986)

+ Predictions from General Electric Co. (1988)

5.6 DATA RATE ASSUMPTIONS AND ANALYSIS

The attached data rate table assumes on-board processing of ALLRAD data sets consisting of event thresholding and data compacting as follows:

1. Precipitation occurrence 3%, collected at 36 levels at full 2 km resolution
2. Cirrus cloud occurrence 10%, collected at 36 levels at 6 km (averaged on board) resolution
3. Stratus cloud occurrence 40%, collected at 36 levels at 25 km resolution

Channels include:

- | | | |
|----|--|----------------------|
| 1. | 2 Meteorological Radar Channels at 36 Levels - | 72.0 |
| 2. | 2 Scatterometer Channels (2 cells) - | 4.0 |
| 3. | 3 Radiometer Channels at 37 GHz - | 3.0 |
| 4. | 2 Radiometer Channels at 19 GHz | |
| | With 2 Polarizations - | 4.0 |
| | | <u>83.0 Channels</u> |

Twelve bit words will be used for each radar and radiometer cell. A constant scan rate of 16.5 rpm results in modest peak and average data rates. The 7 KHz pulse repetition frequency used for the scanning altimeter solution (Section 3.2) and the scan rate of nearly 17 rpm results in approximately 20 pulses averaged per radar cell. The 2 meteorological radar channels result in a data rate of 8.4 Kbps for each radar cell or a peak data rate, assuming the occurrence of precipitation, of 303 Kbps. The continuous scatterometer and radiometer channels add 16 Kbps each for a combined total of 335 Kbps. This represents the highest data rate that the system would experience over the duration of precipitating clouds. If the frequency of occurrence estimates given at the beginning of this section are used with an on-board processing system that detects the reflectance levels and then samples the data in accordance with cloud type, the orbital average data rate for the meteorological channels becomes 27 Kbps. Adding the surface scatterometer and radiometer channels produces a combined average rate of 59 Kbps. This rate would produce a daily data volume of 5.1×10^9 bits.

The on-board storage technologies being considered for DMSP BLOCK VI are more than adequate to cover this rate and volume as shown in Table 5.8.1. The DMSP preference for a 1993 time period mission is the static RAM option which represents a weight and power advantage over the magnetic tape and bubble memory options.

TABLE 5.6.1

DMSP BLK VI
MASS MEMORY SURVEY (1988)

BASELINE	DIGITAL TAPE	STATIC RAM	BUBBLE MEM
INPUT - 1.04 MBPS	2502 IN. ³	820 IN. ³	2016 IN. ³
OUTPUT - 12.2 MBPS	77.6 LB	49 LB	80 LB
STORE - 6.2×10^9	65 W	17.5 W	50/475 W

BASELINE RADIOMETER

The radiometer subsystem will be comprised of 2 systems at 37 GHz with footprints overlapping the 2 radar footprints. It is not obvious that both polarizations are required and at this time it is assumed that it will utilize the same feed structure as the radar. It will be of the Dicke type, and the radiometer LNA will be switched to a dummy load preferably when the radar is transmitting or receiving the strong surface echoes. Absolute calibration will be achieved by occasionally switching to a feed looking at cold space. Additional isolation between the radar and the radiometer will be realized by frequency selective filters.

An additional pair of dual polarized radiometers will be at 19.4 GHz illuminating approximately the same volumes as the radars with the exception that the beam diameters will be somewhat larger (as will the integration times).

Suggested parameters are listed below. Other feeds at 22.2 and 85.6 GHz to yield SSM/I performance could be implemented, but were not considered in this study.

Frequencies	Ku (19.4) and Ka (37) GHz
Bandwidths	Greater than 1 GHz
Type	Unbalanced Dicke
Noise Figure (DSB)	1.5 dB at 19.4, 2.0 dB at 37 GHz
Delta T*	$\approx 0.6^\circ \text{ K}$ at 19.4 GHz $\approx 0.9^\circ \text{ K}$ at 37 GHz
Integration Time	3.4 msec at 19.4 rain
(800 km Orbit)	2.0 msec at 37 GHz
Accuracy	$\pm 1.5^\circ \text{ K}$

*Delta T will be somewhat dependent on whether there is rain and whether the background is land or oceans.

5.8 POWER AND WEIGHT ESTIMATES

The weight and power estimates of the baseline Allrad are listed below. Two transmitters are utilized for reliability and increased data rate.

<u>Component</u>	<u>Avg. Power (Watts)</u>	<u>Mass (Kg)</u>
Antenna Subsystem		
- Array Feed, Reflector, Boom	40	95
RF Subsystem		
- Radar Transmitters (2)	1800	120
- Radar Receivers (2)	40	15
- Radiometer Receivers	50	15
Spin Subsystem	50	85
- Spin Control Electronics Assy.		
- Spin Motor Assembly		
- Momentum Wheel Assy.		
- Boom Hinge Motor Assy.		
- Release Mechanism		
- Balance Assembly		
Electrical Subsystem	140	40
- Power Converter Assy.		
- Power Distribution Assy.		
- Spacecraft Interface Assy.		
- Data Processor Assembly		
Harness Assembly		16
Mechanical Subsystem		50
- Structure		
- Payload Assembly Plate		
Thermal Protection		14
TOTAL SENSOR	2120	450
For the total spacecraft, the following are estimates excluding fuel for orbit maintenance:		
Power (28 m^2)		280
Thermal		62
TT & C		5
Structure		<u>83</u>
TOTAL	<u>673</u>	<u>430</u>
OVERALL TOTAL	2793	880

6.0 SYSTEM TRADEOFFS AND PLAN OF ACTION

6.1 ORBIT SELECTION

Selection of an orbit for ALLRAD depends on a complex set of trade-offs between radar performance and mission data collection which can be expressed as coverage as a function of time and geographic location. For example, lower altitude orbits can reduce the cost of the radar and mission requiring less expensive launch vehicles, etc. At the same time, the lower altitude orbits may result in decreased coverage rates due to narrower swathwidths and require more orbital maintenance expendables (propulsion) to compensate for increased drag.

A microwave sensor derives no benefit from the 98.7° inclined sun-synchronous orbits currently used for meteorological weather satellites such as DMSP. As the SEASAT satellite demonstrated, a more inclined orbit has the virtue of better repeat characteristics as a function of latitude and also collects synoptic cloud maps over varying diurnal cycles. This improves the understanding of global climatological patterns. The figures that follow illustrate a range of orbital altitudes, swathwidths and the coverage update rates associated with various global coverage and revisit strategies.

In Figure 6.1.1, the revisit interval vs latitude is shown for 400 km and 800 km swaths associated with a 800 km altitude, 98.7 degree sun synchronous orbit. This orbit is similar to the current 833 km DMSP orbit. Figure 6.1.2 plots revisit interval vs latitude for 300 km and 600 km swaths associated with a 550 km altitude, sun synchronous orbit. Figure 6.1.3 illustrates the revisit interval vs latitude for 200 km and 400 km swaths associated with a 300 km altitude, sun synchronous orbit.

In all cases, significant time (days) elapse before any of these orbits provide complete coverage in mid-latitude regions of interest. A possible solution is to change orbital inclination to match a region of particular interest. The final two figures demonstrate this possibility.

Figure 6.1.4 shows the revisit interval vs orbit inclination and demonstrates the improvement in revisit timing associated with inclining a 800 km altitude, 800 km swath orbit nearer a latitude of interest, in this case 45 degrees. For example a 50 degree inclined orbit improves revisit by nearly a factor of 3, achieving a respectable twice a day revisit. Figure 6.1.5 plots revisit interval vs inclination for a 300 km altitude, 400 km swath orbit.

An experimental "proof-of-concept" ALLRAD mission designed for a 400 km swathwidth using a 300 km altitude circular orbit inclined near 66° would provide improved coverage rates over much of the globe. Such a system would cover to 70° north and south latitude. The major benefit of the lower orbit is one of total system or mission cost. Soviet experimental satellites, such as the recent Cosmos 1870 space-based radar system, take advantage of the lower altitude orbit (approximately 300 km) on radar performance, design and cost while accepting some compromise in mission duration (probably 1 year or less) due to drag effects. An orbit near 800 km could be used, following the proof-of-concept mission, to provide improved revisit times/coverage rates and extended mission lifetimes (3 to 5

years with the limitation due more to radar longevity than orbital maintenance).

An estimate of the fuel required to maintain an orbit was derived using a computer model and assuming a spacecraft and payload mass of 1000kg, a drag coefficient of 2.5, an area of 24 m^2 and a specific impulse of 220 sec. The results show that it would take about 39kg of fuel per month for a 300km orbit, but only 0.6kg for a 550km orbit and 0.3kg for an 800km orbit. For a long life mission, a 300km orbit would not be practical. It is believed that any orbit above 420km would be practical.

FIGURE 6.1 REVISIT TIME VS LAT.

ALT. = 800 km, INCLINATION = 98.7 deg.

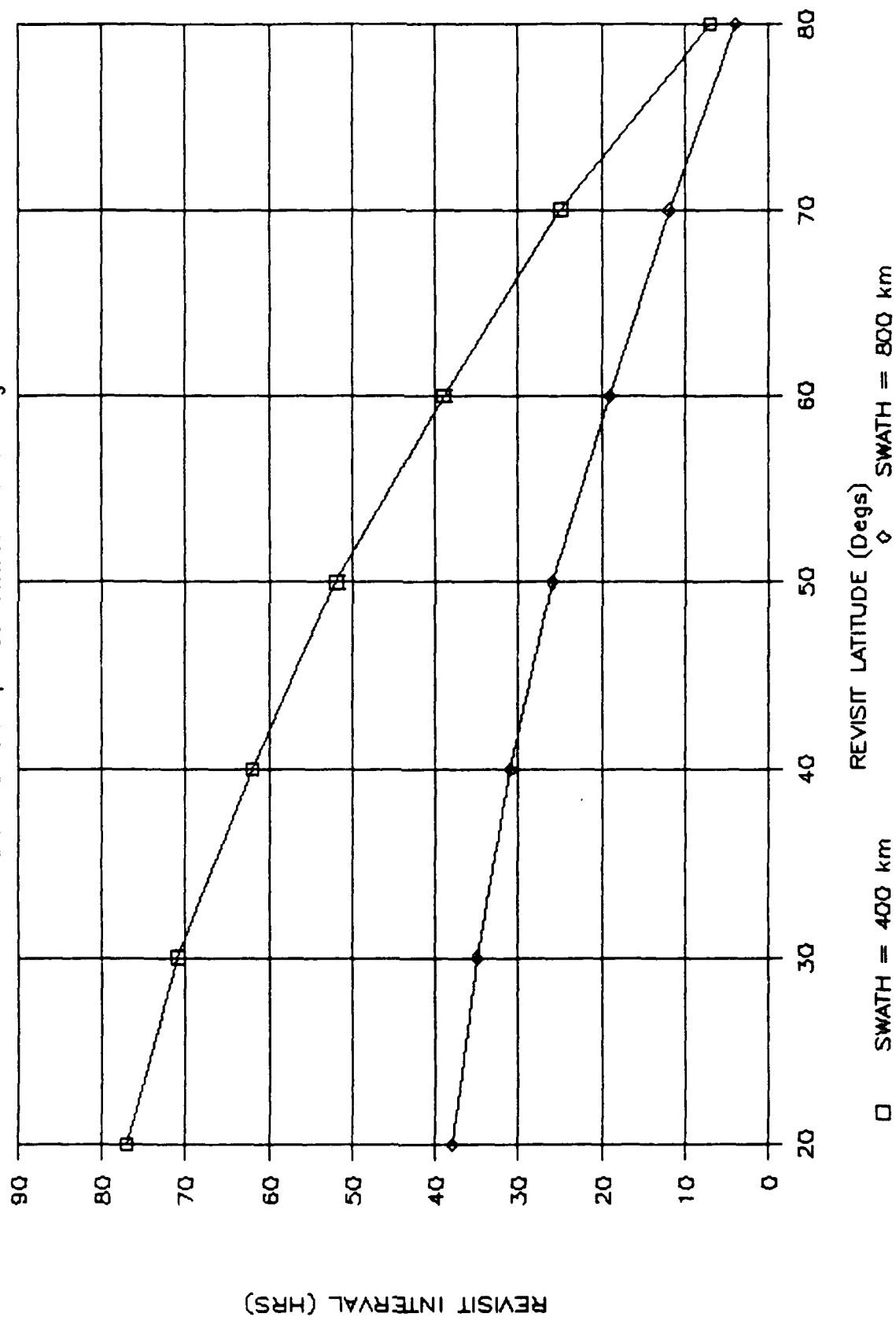


FIGURE 6.2 REVISIT TIME VS LAT.

ALT. = 550 km, INCLINATION = 98.7 deg.

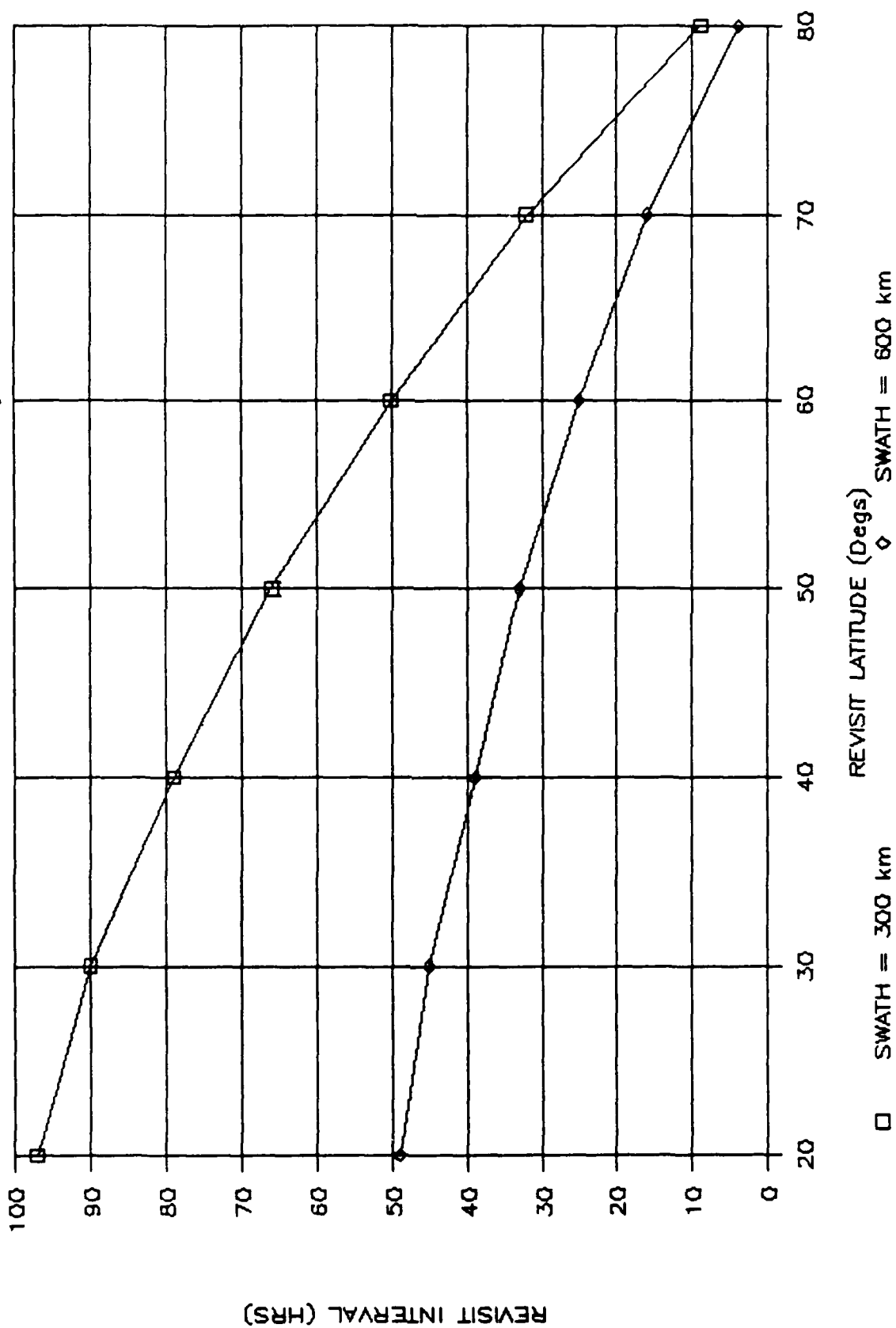


FIGURE 6.3 REVISIT TIME VS LAT.

ALT. = 300 km, INCLINATION = 98.7 deg.

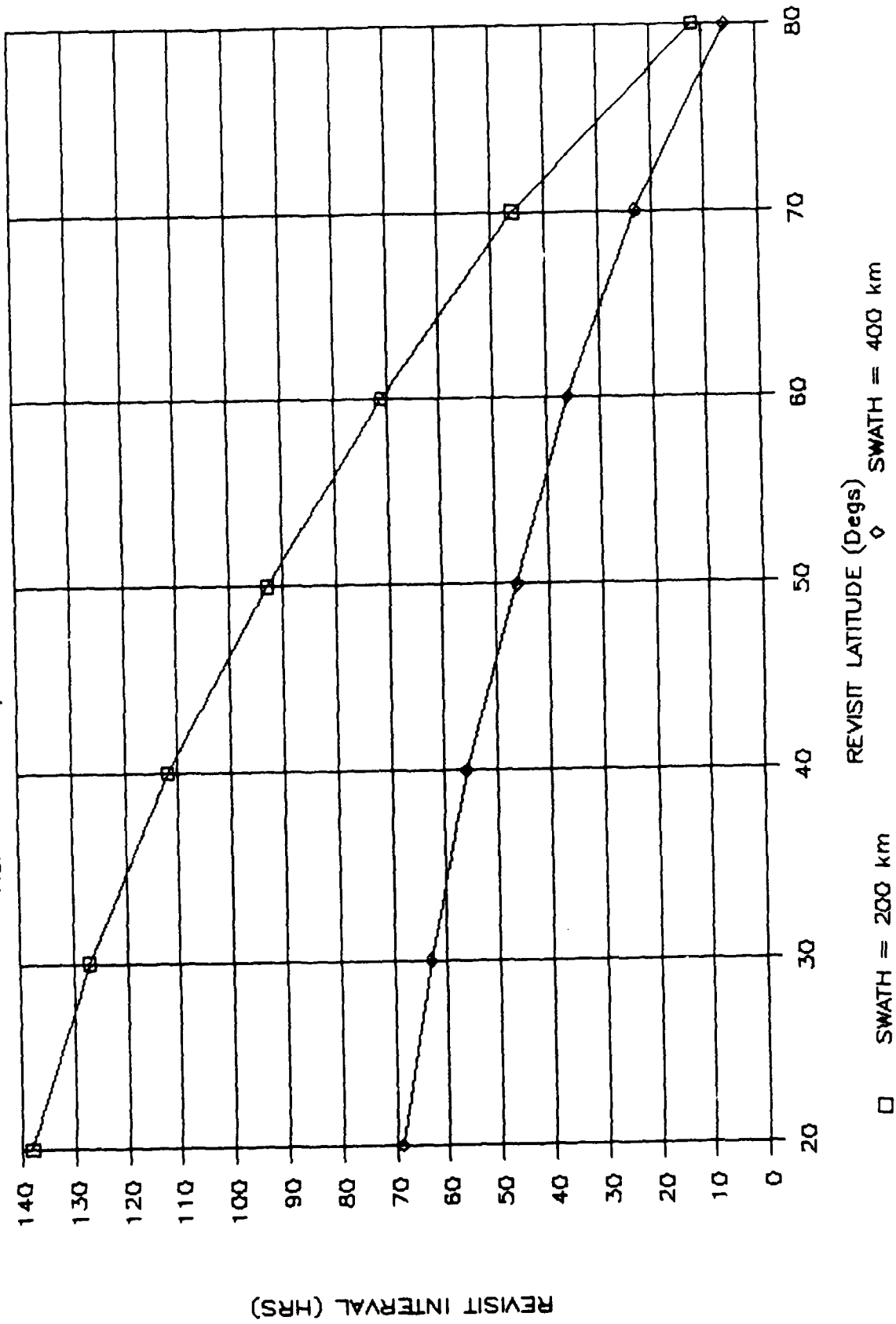


FIGURE 6.4 REVISIT TIME VS INCL.

ALT. = 800 km, LAT = 45, SWATH = 800km.

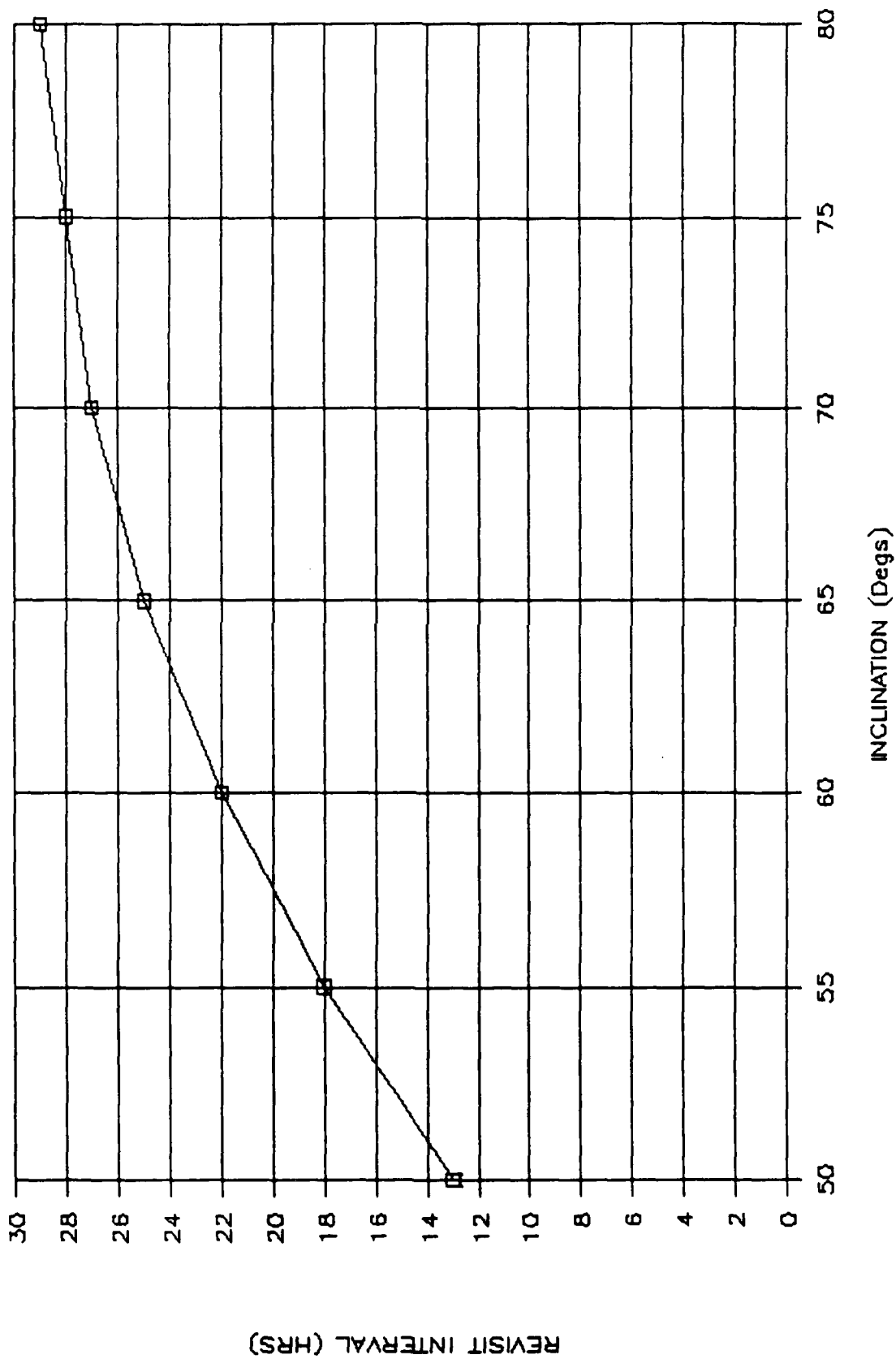
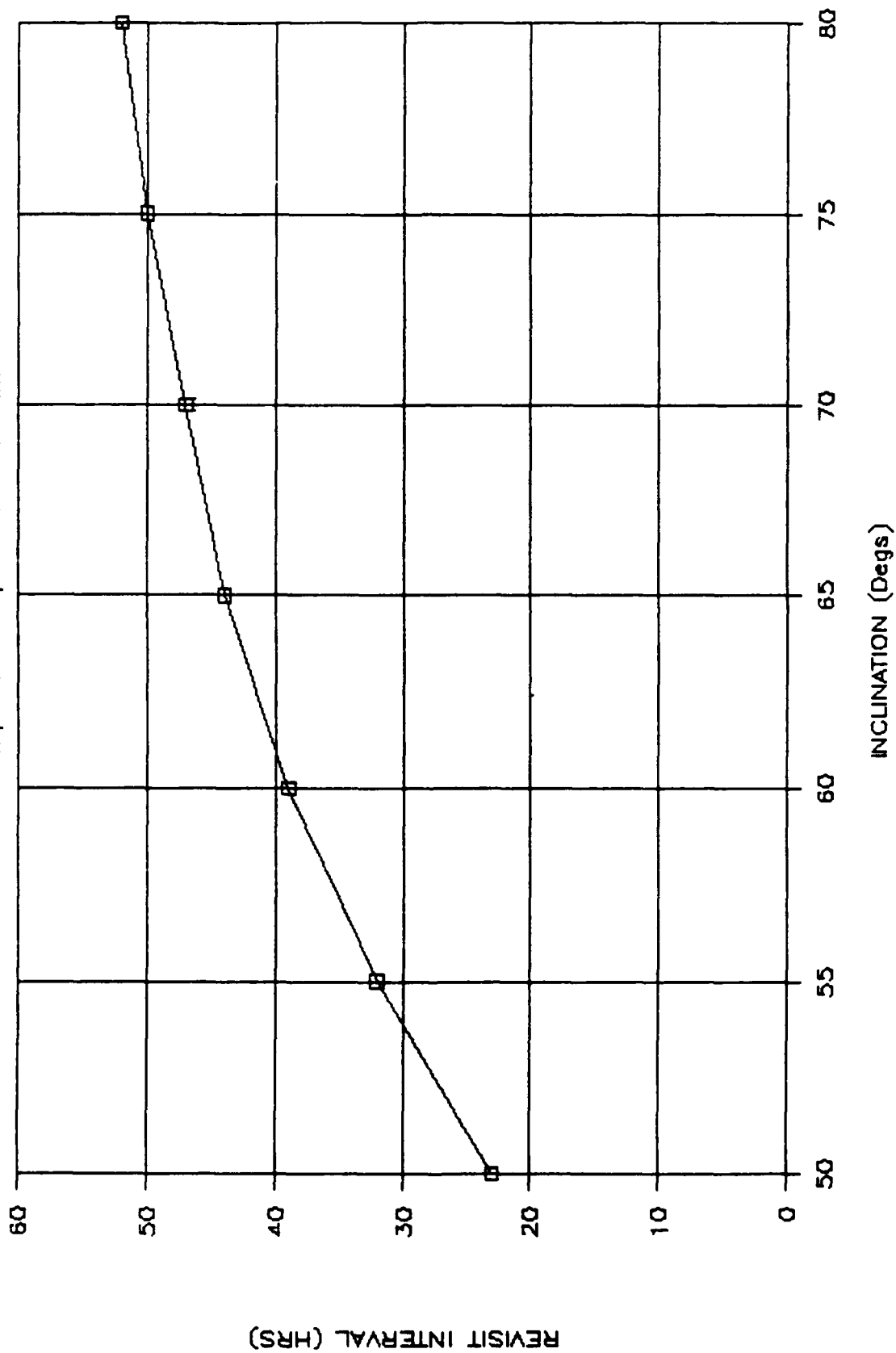


FIGURE 6.5 REVISIT TIME VS INCL.

ALT. = 300 km, LAT = 45, SWATH = 400km.



6.2 Long Lead Items

If a launch is desired in 4-5 years, some efforts should be initiated early in the process. The main item is the transmitter and then the transmitter power supply. While the proposed klystron should be rugged enough, it will need to be space qualified. For an "operational" system, a lifetime of 3-5 years is desired as compared to current cathode lifetime of 1 year. While Varian has a 100,000 hour cathode life program, it would need to be subsidized for timely tube delivery. The current tube would be adequate for breadboard tests. Development of a long life tube is about a 2 1/2 year process followed by the space qualification process.

The transmitter power supply and modulator has a shorter development cycle with a space version potentially available in 1 1/2 to 2 years from manufacturers who build space radars. Since the tube will fit into the transmitter module and the total module should be space qualified together, it seems imperative to develop them together. The lowest risk approach is to contract for the total transmitter and let that contractor subcontract for the tube and space qualification.

The next long lead item is the antenna and especially the array feed. The remainder of the components are quite straightforward.

RECOMMENDATIONS

It is believed that the Radar Sounder System will provide a significant advance in Global Meteorological Capability to detect and locate cloud tops and bottoms and the freezing level along with being able to determine cloud cover, cloud type and an estimate of rainfall rate. In addition, there will be a capability to determine surface winds over the ocean, mapping of ice and other geophysical phenomena.

The configuration and orbit will be somewhat dependent on the primary mission. Sensitivity to detect weak stratus clouds will be best achieved with a low orbit (300 km) and a 200-400 km swath. Updating of Global Meteorological Models calls for larger swaths with some sacrifice in sensitivity. Sensitivity can be traded off with horizontal resolution. For tactical applications, orbit inclination and number of satellites must be considered.

While the lower orbit is compatible with a shuttle launch, An 800 km orbit is compatible with the NASA EOS Program or DMSP Block 6. For deployment on small satellites the antenna diameter must be reduced to 3.5 meters. For shorter revisit times an inclined orbit is recommended.

For primarily oceanographic applications a greater NADIR angle will best replicate the SCATTEROMETER function.

The recommended waveform will allow measurement of wind velocity when there are clouds or precipitation. With nadir angles of 15° - 30° , the fall rate of the drops in rain must be estimated. Since there is a forward and backward look at each area, this should not be difficult. Accuracy will depend upon the nadir angle and the complexity of the array feed. The signal processing would not be complicated. A short (6 month) study is recommended as this capability would greatly enhance the systems utility for updating global meteorological models.

Assuming that there is interest in initiating development, the next step is to define and implement a brassboard system that can be placed on an aircraft or mountaintop. It would use current technology including a 1.5-2.0 foot dish and a current transmitter. The definition and implementation could be completed in about 2 years and would include at least one pair of radiometer channels.

AIRCRAFT EXPERIMENT

A high altitude aircraft experiment with a brassboard model of the radar/radiometer would be useful to validate the algorithms linking the radar, radiometer and scatterometer, and to obtain data for input to meteorological models. It should fly above the clouds if possible, have resolution comparable to the satellite version and be flown near meteorological facilities.

There appears to be a reasonable way of accomplishing this with a Lockheed TR-1 (U-2). Lockheed has run millimeter wave radiometer experiments with these aircraft and can cut-out a portion of the bottom of the A/c to allow downward viewing without a radome that might disturb the antenna sidelobes. A previous installation is shown on Fig 7.1. Flight would be at about 68,000 ft altitude. The ALLRAD would be mounted on a removable section. Flying costs would be about \$2000/hr. About a 700 pound package is allowed. The planes are usually flown out of Ames AFB, California. An alternate aircraft would be the Westinghouse BAC III flown out of BWI near Baltimore. However, it does not have the altitude capability of the U2.

A sample set of scaled parameters is shown on Table 7.1. It is expected that a version for the National Aerospace Plane would have similar parameters.

TABLE 7.1 AIRCRAFT BRASSBOARD MODEL

Altitude	- 20 km (66 kft) TR-1
Velocity	- 200 m/sec (388 knots)
D_s	- 50 km swath
R_s	- 43 km
Nadir Angle	$\approx 51^\circ$
D antenna	- 61 cm (72 λ)
θ	- .018 rad (1.0 $^\circ$)
Res	$\approx .8$ km (azimuth)
T	- 350 μ sec
PRF	- 4 KHz
Circumference	- 157 km (200 cells)
T_{cell}	- 5000/200 = 25 msec
N	- 4 x 25 = 100
τ	- 3.75 μ sec
T_s	- 600 μ
B_N	- 300 KHz
P_t	- .1 to 2 kw peak
DF	- 1.5%
P_{avg}	- 15 to 30 w
L	- 4.5 db



Figure 8.1

1. Simpson, J., R. F. Adler and G. R. North, "A Proposed Tropical Rainfall Measuring Mission (TRMM) Satellite," Bulletin American Meteorological Society, Volume 69, No. 3, March 1988, pp. 278-295.
2. Goldhirsh, J., "Analysis of Algorithms for the Retrieval of Rain Rate Profiles from a Spaceborne Dual Wavelength Radar," JHU/APL, S1R87U-001, January 1987.
3. Bucknam, J. N., "Performance Comparison of Simultaneous Beam vs. Scanning Beam Configurations for the NASA/Goddard METSAT Radar," Technology Service Corporation, TSC-W7-16, 24 October 1974.
4. Cole, A. E., R. J. Donaldson, R. Dyer, A. J. Kantor and R. A. Skrivanek, "Precipitation and Clouds: A Revision of Chapter 5, Handbook of Geophysics and Space Environments," Air Force Cambridge Research Laboratories, AFCRL-69-0487, November 1969. AD703288
5. Goldhirsh, J. and E. J. Walsh, "Precipitation Measurements from Space Using a Modified Seasat Type Radar Altimeter," JHU/APL, S1R81U-022, May 1981.
6. Meneghini, R., J. A. Jones and L. H. Gesell, "Analysis of a Dual-Wavelength Surface Reference Radar Technique," IEEE Transactions on Geoscience and Remote Sensing, Volume GE-25, No. 4, July 1987, pp. 456-471.
7. Wilheit, T. T., et. al., "Microwave Radiometric Observations Near 19.35, 92 and 183 GHz of Precipitation in Tropical Storm Cora," Journal of Applied Meteorology, Volume 21, No. 8, August 1982, pp. 1137-1145.
8. Lhermitte, R. M., "Small Cumuli Observed with a 3mm Wavelength Doppler Radar," Rosenstiel School of Marine and Atmospheric Science, University of Miami, Geophysical Research Letters, Volume 14, No. 7, July 1987, pp. 707-710.
9. Taylor, H. P., "The Radiometer Equation," The Microwave Journal, May 1967, pp. 39-41.
10. Wilheit, T. T., A. T. C. Chang, M. S. V. Rao, E. B. Rodgers and J. S. Theon, "A Satellite Technique for Quantitatively Mapping Rainfall Rates Over the Oceans," Journal of Applied Meteorology, Volume 16, 1977, pp. 551-560.
11. Okamoto, K., T. Kozu, K. Nakamura and T. Ihara, "Conceptual Design of TRMM Rain Radar," Radio Research Laboratory, Japan, 3rd TRMM Expert Panel Meeting, August 1987.

12. Eaves, J. L. and E. K. Reedy, "Principles of Modern Radar," Van Nostrand Reinhold Company, Inc., 1987, pp.
13. Doviak, R. J. and D. S. Zrnic, "Doppler Radar and Weather Observations," Academic Press, Inc., 1984, pp.
14. Atlas, D. and R. Meneghin, "Rain Retrieval Algorithms for Spaceborne Radar," NASA/Goddard Space Flight Center, September 1987, pp.
15. Atlas, D. and O. Thiele, "Precipitation Measurements from Space," NASA/Goddard Space Flight Center, Workshop Report, October 1981, pp.
16. Lhermitte, R. M., "94 GHz Doppler Radar Project," Army Research Office Contract, DAAG29-84-K-0145, 1986, pp.
17. Atlas, D. and C. W. Ulbrich, "Path and Area Integrated Rainfall Measurement by Microwave Attenuation in the 1-3 CM Band," Proceedings of 7th Conference Radar Meteorology, October 26-29, 1976, pp. 406-412.
18. Battan, L. J., Radar Observations of the Atmosphere, University of Chicago Press, 1973.
19. Eckerman, J., R. Meneghini and D. Atlas, "Average Rainfall Detection from a Scanning Beam Spaceborne Meteorological Radar," NASA Tech Memo. 79664, November, 1978.
20. Fujita, M., K. Okamoto, S. Yoshida and K. Nakamura, "Interference of Rain Rate Profile and Path-Integrated Rain Rate by an Airborne Microwave Rain Scatterometer," Radio Science, Vol. 20, 1985, pp. 631-642.
21. Goldhirsh, J. and E. J. Walsh, "Measurement of Precipitation with a TOPEX-Class Dual Frequency Satellite Altimeter," Proceeding of URSI Commission F, Multiple-Parameter Radar Measurements of Precipitation, (Bournemouth, UK), August, 1982.
22. Goldhirsh, J. and F. Monaldo, "Achieving Improved Frequency Response of the Rain Structure from Spaceborne Radar Altimeters by Employing Deconvolution Methods," Journal Geophys. Research, Vol. 91, No. C2, February 15, 1986, pp. 2338-2344.
23. Goldhirsh, J. and B. Musiani, "Rain Cell Size Statistics Derived from Radar Observations at Wallops Island, Virginia," IEEE Trans. Geoscience and Remote Sensing, Vol. GE-24, No. 6, November, 1986, pp. 947-954.

24. Meneghini, R., J. Eckerman and D. Atlas, "Determination of Rain Rate from a Spaceborne Radar Using Measurements of Total Attenuation," IEEE Trans. Geoscience and Remote Sensing, Vol. GE-21, 1983, pp. 34-43.
25. Meneghini, R., J. A. Jones and L. H. Gesell, "Analysis of a Dual-Wavelength Surface Reference Radar Technique," IEEE Trans. on Geoscience and Remote Sensing, Vol. GE-25, No. 4, July, 1987, pp. 456-471.
26. Stout, G. E. and E. A. Mueller, "Survey of Relationships Between Rainfall Rate and Radar Reflectivity in the Measurement of Precipitation," Journal of Applied Meteorology, Vol. 7, 1968, pp. 465-474.
27. Goldhirsh, J., "Rain Cell Size Statistics as a Function of Rain Rate for Attenuation Modeling," IEEE Trans. on Antennas and Propagation, Vol. AP-31, No. 5, September, 1983, pp. 799-803.
28. Hitschfeld, W. and J. Bordan, "Errors Inherent in the Radar Measurement of Rainfall at Attenuating Wavelengths," Journal of Meteorology, Volume 11, pp. 58-67.
29. Atlas, D. and R. K. Moore, "The Measurement of Precipitation with Synthetic Aperture Radar," Journal of Atmospheric and Oceanic Technology, Volume 4, pp. 368-376.
30. Goldhirsh, J., "Yearly Variations of Rain-Rate Statistics at Wallops Island and Their Impact on Modeled Slant Path Attenuation Distributions," IEEE Trans. on Antennas and Propagation, Volume AP-31, No. 6, November, 1983, pp. 918-930.
31. Atlas, D. and T. J. Matejka, "Airborne Doppler Radar Velocity Measurements of Precipitation Seen in Ocean Surface Reflection," Journal of Geophysical Research, Volume 90, No. D3, June, 1985, pp. 5820-5828.
32. Simpson, J., R. F. Adler and G. R. North, "A Proposed Tropical Rainfall Measuring Mission (TRMM) Satellite," Bulletin American Meteorological Society, Volume 69, No. 3, March, 1988, pp. 278-295.
33. Elachi, C., Spaceborne Radar Remote Sensing: Applications and Techniques, IEEE Geoscience and Remote Sensing Society, IEEE Press, New York, 1987.
34. Doviak, R. J. and D. S. Zrnic, "Doppler Radar and Weather Observations," Academic Press, Inc., 1984.
35. Kanter, I., "Exact Detection Probability for Partially Correlated Rayleigh Targets," AES, Volume AES-22, No. 2, pp. 184-196.

36. Hollinger, J., R. Lo, G. Poe, R. Savage and J. Peirce, "Special Sensor Microwave/Imager Users Guide," Naval Research Laboratory, Washington, DC, 14 September 1987.
37. Bunting, J. T., R. S. Hawkins and R. P. d'Entremont, "R & D Nephanalysis at the Air Force Geophysics Laboratory," Preprints 5th Conf. Atmospheric Radiation, AMS, pp. 272-275, 1983.
38. Carrier, L. W., G. A. Cato and K. J. von Essen, "The Backscattering and Extinction of Visible and Infrared Radiation by Selected Major Cloud Models," Appl. Optics, 6(7), pp. 1207-1216, 1967.
39. Crane, R. K., "Automatic Cell Detection and Tracking," IEEE Trans. Geosci. Electron., GE-17, pp. 250-262, 1979.
40. Crane, R. K. and K. R. Hardy, "The HIPLEX Program in Colby-Goodland Kansas: 1976-1980," Rept. P-1552-F, Environmental Research & Technology, Concord, MA, 1981.
41. Crane, R. K., "Studies on Growth/Decay in Storm Tracking," Thayer School of Engineering, Dartmouth College, Hanover, NH, 1987.
42. Crane, R. K., "Space - Time Structure of Precipitation," 10th Conf. Meteorol. Statistics, AMS.
43. Westwater, E., Private Communications, 1987.
44. Falcone, V. J. and L. W. Abreu, "Atmospheric Attenuation of Millimeter and Submillimeter Waves," EASCON '79 Record, IEEE Pub., 79CH 1476-1 AES, pp. 36-41, 1979.
45. Greaves, J. R., "Development of Global Cloud Model for Simulating Earth-Viewing Space Missions," J. Appl. Meteorol., 12, pp. 12-22, 1973.
46. Joss, J., R. Cavalli and R. K. Crane, "Good Agreement Between Theory and Experiment for Attenuation Data," J. Recher. Atmosph., VIII(1-2), pp. 299-318, 1974.
47. Sheer, P. E., A. H. Glaser, J. C. Barnes and J. H. Willand, "Worldwide Cloud Cover Distributions for use in Computer Simulations," Applied Res. Assoc., Concord, MA, 1969.
48. Slobin, S. D., "Microwave Noise Temperature and Attenuation of Clouds: Statistics of These Effects at Various Sites in the United States, Alaska, and Hawaii," Radio Sci., 17(6), pp. 1443-1454, 1982.
49. Crane, R. K., "Space-time Structure of Precipitation," Pre-prints 10th Conference Probability and Statistics in Atmospheric Sciences, pp. 265-268, AMS, Boston, MA, 1987.